



HAL
open science

Correlations and symmetries in one-dimensional ultracold atomicgases

Gianni Aupetit-Diallo

► **To cite this version:**

Gianni Aupetit-Diallo. Correlations and symmetries in one-dimensional ultracold atomicgases. Condensed Matter [cond-mat]. Université Côte d'Azur, 2023. English. NNT: 2023COAZ4110. tel-04508765

HAL Id: tel-04508765

<https://theses.hal.science/tel-04508765>

Submitted on 18 Mar 2024

HAL is a multi-disciplinary open access archive for the deposit and dissemination of scientific research documents, whether they are published or not. The documents may come from teaching and research institutions in France or abroad, or from public or private research centers.

L'archive ouverte pluridisciplinaire **HAL**, est destinée au dépôt et à la diffusion de documents scientifiques de niveau recherche, publiés ou non, émanant des établissements d'enseignement et de recherche français ou étrangers, des laboratoires publics ou privés.



$$\rho \left(\frac{\partial v}{\partial t} + v \cdot \nabla v \right) = -\nabla p + \nabla \cdot T + f$$

$$e^{i\pi} + 1 = 0$$

THÈSE DE DOCTORAT

CORRELATIONS ET SYMETRIES DANS LES GAZ D'ATOMES ULTRAFROIDS À UNE DIMENSION

Gianni AUPETIT-DIALLO

Institut de Physique de Nice

Présentée en vue de l'obtention
du grade de docteur en Physique
de l'Université Côte d'Azur

Dirigée par : Patrizia Vignolo

Co-dirigée par : Mathias Albert

Soutenue le : 08/12/2023

Devant le jury, composé de:

Maxim Olshanii, Professor,
University of Massachusetts (Boston,
United States)

Sylvain Capponi, Professeur,
Laboratoire de Physique Théorique,
FeRMI, Université Paul Sabatier
(Toulouse, France)

Isabelle Bouchoule, Directrice de
recherche, Institut d'Optique
(Palaiseau, France)

Mathilde Hugbart, Directrice de
recherche, INPHYNI (Nice, France)

Ovidiu Pâtu, Research supervisor,
Institute for Space Sciences
(Bucharest-Magurele, Romania)

CORRÉLATIONS ET SYMETRIES DANS LES GAZ D'ATOMES ULTRAFROIDS À UNE DIMENSION

*Correlations and Symmetries in One-dimensional
Ultracold Atomic Gases*

Jury:

Président

Mathilde Hugbart, Directrice de recherche, INPHYNI (Nice, France)

Rapporteurs

Maxim Olshanii, Professor, University of Massachusetts (Boston, United States)

Sylvain Capponi, Professeur, Laboratoire de Physique Théorique, FeRMI, Université Paul Sabatier (Toulouse, France)

Examineurs

Isabelle Bouchoule, Directrice de recherche, Institut d'Optique (Palaiseau, France)

Ovidiu Pâțu, Research supervisor, Institute for Space Sciences (Bucharest-Magurele, Romania)

Directeur de Thèse

Patrizia Vignolo, Professeure, Université Côte d'Azur

Co-directeur de Thèse

Mathias Albert, Maître de conférence HDR, Université Côte d'Azur

Résumé

Corrélations et symétries dans les gaz d'atomes ultrafroids à une dimension

Nous avons mené une étude analytique et numérique d'observables pour les mélanges unidimensionnels de spins atomiques ultrafroids avec interaction de contact entre les atomes. Ces particules peuvent être des bosons, des fermions ou une combinaison des deux. L'accent a été mis sur l'étude des régimes de forte répulsion pour leurs caractéristiques de fortes corrélations. En outre, nous avons exploré en profondeur les propriétés de symétrie des systèmes correspondants. Nous avons d'abord analysé les propriétés de corrélation de gaz atomiques ultra froids piégés dans un potentiel en forme de boîte. Nous avons examiné à la fois le cas de particules identiques et celui, plus complexes, de mélanges de spins. Nos résultats démontrent que les parois rigides du piège ont un impact significatif sur la queue de la distribution des impulsions. Plus précisément, nous avons observé que la discontinuité du piège entraîne une brisure de la relation de Tan. En conséquence, la queue de la distribution de impulsions présente des oscillations que nous avons utilisées pour proposer une méthode expérimentale permettant de déterminer l'état d'un mélange de spins bosoniques. En parallèle, nous avons considéré un modèle de mélange de spins qui brise la symétrie du système. Grâce à l'analyse conjointes des corrélations et de la symétrie, nous avons montré que même une légère brisure de symétrie a un effet considérable sur la cohérence à longue distance du système. De plus, nous avons fourni un protocole expérimental pour la réalisation d'un tel système. Nous suggérons ainsi que de nouveaux états physiques peuvent être conçus pour encoder de l'informations dans le système. Enfin, nous avons abordé un système plus complexe de mélanges bosoniques piégés en forme d'anneau avec un champ de jauge artificiel généré par l'application d'un flux. Nous avons pu obtenir la solution exacte pour des mélanges équilibrés ainsi que le spectre correspondant. Grâce à l'analyse de symétrie, nous avons attribué une symétrie bien définie à chaque partie du spectre, permettant une compréhension plus profonde du système. Cette étude constitue un pas en avant vers des montages expérimentaux permettant de sélectionner un état de symétrie du mélange de spin choisi.

Mots-clés: Physique a N -corps, Atomes froids, Systèmes fortement corrélés

Abstract

Correlations and symmetries in one-dimensional ultracold atomic gases

We have conducted an analytical and numerical investigation of observables for one-dimensional ultracold atomic spin mixtures with contact interaction between atoms. These particles can be either bosons, fermions, or a combination of both. The focus was on studying the strong repulsion regimes for their high correlation features. Furthermore, we have extensively explored the symmetry properties of the corresponding systems. We first analyzed the correlation properties of ultracold atomic gases trapped in a box-shaped potential. We examined both the case of identical particles and the more complex spin mixtures. Our findings demonstrate that the hardwalls of the trap have a significant impact on the tail of the momentum distribution. Specifically, we observed that the trap's discontinuity causes a breakdown of Tan's relation. As a result, the momentum distribution showcases an oscillatory tail, which we utilized to propose an experimental method for determining the state of a bosonic spin mixture. Then, we considered a spin mixtures model, which breaks the system's symmetry. Through joint correlations and symmetry analysis, we have exposed that even a slight symmetry breaking has a tremendous effect on the long-distance coherence of the system. Alongside this, we have provided an experimental protocol for realizing such a system. By this means, we suggest that new physical states can be engineered to encode information on the system. Finally, we moved to a more involving system of ring-shaped trapped bosonic mixtures with an artificial gauge field generated via the application of flux. We were able to obtain the exact solution for balanced mixtures as well as the corresponding spectrum. Thanks to the symmetry analysis, we have assigned a well-defined symmetry to each part of the spectrum, enabling a deeper understanding of the system. This investigation constitutes an engaging step toward experimental setups for selecting a chosen spin mixture symmetry state.

Keywords: Many-body physics, Cold atoms, Highly correlated systems

Glossary

Acronyms	Signification
UCAG	Ultra-Cold Atomic Gases
#D	#-Dimensional
BEC	Bose-Einstein Condensate
MOT	Magneto-Optical Trap
PBC	Periodic Boundary Conditions
DBC	Dirichlet Boundary Conditions
SF	Spinless non-interacting Fermions
TB	Tonks-Girardeau Bosons
RMT	Random Matrix Theory
PDF	Profile Density Function
PP	Point Process
DPP	Determinantal Point Process
CSCO	Complete Set of Commuting Observables

Contents

1	Introduction to 1D ultracold atomic gases	5
1.1	Why one-dimensional ultracold atomic gases?	5
1.2	Preparing the Lineland journey	6
1.2.1	Reaching ultracold temperatures with neutral atoms	6
1.2.2	What is a 1D quantum system?	7
1.2.3	Contact interactions tuning: The Feshbach resonance	9
1.3	Models and preliminary solutions	11
1.3.1	Non-interacting identical particles	12
1.3.2	Strong interaction limit	13
1.4	Correlations investigation	14
1.4.1	Correlations in real space: The correlation functions	14
1.4.2	Correlations in Fourier space: The momentum distribution	17
2	Ultracold atomic gases of identical particles	19
2.1	A first exact solution	19
2.1.1	The two-body problem	19
2.1.2	The many-body problem	22
2.2	The correlation functions	25
2.2.1	General definition in quantum mechanics	25
2.2.2	Spinless fermions and random matrix theory	26
2.2.3	Tonks-Girardeau regime	29
2.3	The momentum distribution	31
2.3.1	Long-distance coherence	32
2.3.2	Short-distance correlations	34
3	Spin mixtures in highly repulsive regime	37
3.1	The Bethe wave function	37
3.1.1	Arbitrary interaction strength	37
3.1.2	Highly repulsive regime	39
3.2	Spin mixtures in the high repulsion regime	40
3.2.1	The Volosniev formalism	41
3.2.2	Equivalence to the XXZ spin chain	46
3.3	The $SU(n)$ symmetry	48
3.3.1	Define and characterize permutational symmetry: the Young's diagrams	49
3.3.2	Complete set of commuting operators of S_n	53

4	Breakdown of Tan's relations induced by trapping discontinuity	59
4.1	Large- k tail of the momentum distribution in the box for identical particles	60
4.1.1	Spinless non-interacting fermions	60
4.1.2	Tonks-Girardeau bosons	64
4.2	Large- k tail of the momentum distribution in the box for spin mixtures	65
4.2.1	Generalities about spin mixtures	66
4.2.2	Derivation of \mathcal{K}_N	66
4.2.3	Investigation on \mathcal{K}_N for a mixture	71
4.2.4	Φ_N^{mix} as a ground state probe	74
4.2.5	Concluding remarks	76
5	Symmetry analysis	77
5.1	Exact solution for $SU(2)$ symmetry breaking of bosonic mixtures at strong interactions	77
5.1.1	The model	78
5.1.2	Analysis of the symmetry breaking	82
5.1.3	Proof of the $SU(2)$ symmetry breaking	84
5.1.4	Commutation between $\hat{\Gamma}^{[2]}$ and $\hat{H}_P^{SU} = V^{SU}/g$	84
5.1.5	Commutation between class sum operators and $H_P^{SB} = V^{SB}/g$	87
5.1.6	Correlations analysis	87
5.1.7	Long-distance coherence	89
5.1.8	Short-distance correlations: the Tan's contact	91
5.1.9	Concluding remarks	91
5.2	Spin mixtures with artificial gauge field on a ring	93
5.2.1	Model and definitions	93
5.2.2	Case of two particles	95
5.2.3	Results for $N = 4, N_{\downarrow} = 2$	97
5.2.4	Concluding remarks	100
	Conclusion	103
A	Derivation of the Volosniev matrix	105
A.1	The nearest-neighbor exchange constant	105
A.1.1	α_N in the ring	105
A.1.2	α_N in the box	107
A.2	Construction of the Volosniev matrix	108
B	$SU(2)$ symmetry analysis of a $2 + 2$ mixture in the box	113
B.1	Derivation of the $\gamma_{[\nu]}^{[r]}$ and dimension of the CSCO	113
B.2	Element and representations of the conjugacy classes cc_r	114
B.3	r -cycle class-sum operators and symmetry analysis	116
C	Large-k tail of the momentum distribution of TB in the box	119
	Bibliography	121

Introduction

Ultra-Cold Atomic Gases (UCAG) represent a fascinating and effervescent area of physics. By cooling atoms to significantly cold temperatures, the matter is pushed into extreme conditions and exhibits new features. The study of UCAG began with the discovery and comprehension of atoms [Curie, 1894, Einstein, 1905b], which was made possible by the joint efforts of spectroscopy and quantum mechanics in the 19th and 20th centuries. Initially, atomic gases were roughly studied at room temperature, but it was evident that cooler and more still atoms were required. This led to the pursuit of ultracold temperatures, resulting in significant fundamental and experimental breakthroughs.

When the matter is pushed to ultracold temperatures, the particles exhibit entirely new behaviors due to their quantum nature. For instance, an ultracold atomic gas can undergo a phase transition to a Bose-Einstein condensate (BEC) [Anderson et al., 1995] or become degenerate [Holland et al., 2001], depending on their constituents' statistics. BEC is a typical example of a phenomenon which have no classical counterpart. Indeed, below a specific temperature, a large number of atoms will start to occupy the lowest energy state, resulting in a macroscopic manifestation of the wave function. As a consequence, these gases behave as coherent waves rather than a bunch of individual particles. This transition is expected for very low temperatures. In terms of thermal energy, typically, of the order of the difference between energy levels. However, it generally occurs at energy far above, enabling observation of quantum effects on a macroscopic scale. We could also evoke other phenomena, such as superfluidity [Kapitza, 1938, Allen & Misener, 1938], where the gas flows without any resistance or Mott insulator phases transition [de Boer & Verwey, 1937, Mott & Peierls, 1937]. The various exotic states of matter that UCAG showcases are fascinating enough to pique anyone's interest, but UCAG has been instrumental in some groundbreaking applications. For instance, one can think about the development of the quantum computer and the atomic clocks we use daily. However, resuming its contributions to these two achievements would be reductive, so we will provide a brief overview of UCAG's key strengths.

Starting off, UCAG are by nature especially sensitive to fields, like gravitational [Peters et al., 1999, Doughty & Lawler, 1984, Kasevich & Chu, 1991] or magnetic [Wildermuth et al., 2005, Faley et al., 2004, Kominis et al., 2003]. In parallel, confinement setups have benefited from current drastic size reductions. This combination of factor have made UCAG an ideal option for constructing portative sensors. See Figure 1 for a recent example of an application. Next, UCAG turned out to be an excellent option to simulate other quantum systems. This concept is not new, and credit must be given to Y. I. Manin [Manin, 1980]. R. Feynman has afterward encaps-

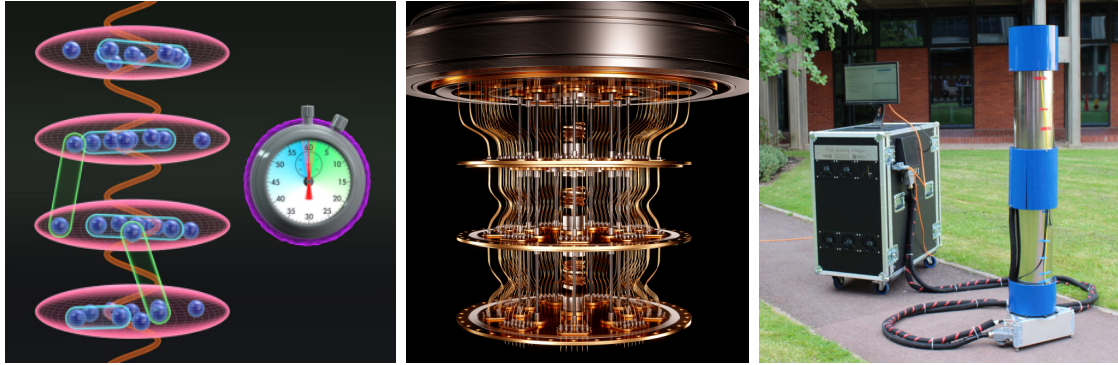


Figure 1: (Left) Schematic view of the interaction intra and inter-atomic lattices leading to improved atomic clock precision. Image Credit: S. Burrows/A. M. Rey and J. Ye groups at JILA, Boulder, Colorado [[Web Site](#)] (Center) Artistic representation of a quantum computer. Image from [[Castelvecchi, 2023](#)] (Right) Quantum sensors using matter interference to detect gravitational field local fluctuations [[Stray et al., 2022](#)].

sulated this idea with his famous words: "Nature isn't classical, dammit, and if you want to make a simulation of nature, you'd better make it quantum mechanical, and by golly it's a wonderful problem, because it doesn't look so easy" [[Feynman, 1982](#)]. On top of that, UCAG displays analogies with a broad range of physics domains, including condensed matter [[Bloch et al., 2008](#), [Satija & Zhao, 2013](#), [Lewenstein et al., 2007](#)], fluid mechanics [[Fetter & Svidzinsky, 2001](#), [Langen et al., 2015](#)], and general relativity [[Barceló et al., 2001](#), [Gerritsma et al., 2010](#)], expanding the potential applications of quantum simulators.

As we begin to glimpse, UCAG encloses a wide variety of topics. Among all the engaging possibilities, we will dedicate the present document to analyzing One-Dimensional (1D) UCAG with contact interaction between particles. These atoms will be bosons, fermions, or both and of different spin species with a particular focus on correlations and symmetry effects.

The document will follow this plan:

In the introductory Chapter 1, we will discuss the unique characteristics and benefits of UCAG in 1D. We will also briefly overview the typical experimental setup and explore the standard quantities accessible theoretically and experimentally. Additionally, we will provide examples of experimental setups used to probe these quantities successfully.

In Chapter 2, we will derive the explicit solution of the Lieb-Liniger Hamiltonian for two particular trapping configurations. We will complete this with a focus on the limit of high repulsion. Subsequently, we will examine the correlations in both real and Fourier spaces to determine how they are affected by this highly interactive environment.

Chapter 3 will be dedicated to the more involving scenario of spin mixtures. We will introduce the corresponding Hamiltonian and provide solutions for fermionic,

bosonic, and Bose-Fermi mixtures in the repulsive regime. Our emphasis will be on the high interaction regime. We will explain the various powerful tools at our disposal for solving and investigating the system. In particular, symmetry analysis will play a crucial role in our approach. After thoroughly defining the system's symmetry, we will provide a comprehensive overview of its application.

In Chapter 4, we will take the first step toward exploring our results. In particular, we will delve into how short-distance correlations can be affected by the smoothness of the trap and how this could be used to probe the state of our system.

With Chapter 5, we end up by giving the outcomes that have provided our symmetries analysis through two examples: What happens when we slightly break the symmetry of the system, and what can furnish the symmetry analysis of a rotating system in a ring?

Chapter 1

Introduction to 1D ultracold atomic gases

1.1 Why one-dimensional ultracold atomic gases?

Now we have explained the appeal for UCAG, let us dive into the 1D specificities with this first legitimate question: why should we "venture" into the Lineland? First and foremost, the 1D realm is an entirely separate domain of quantum mechanics and witnesses of singular behavior compared to higher dimensions.

To begin with a general rule, *only collective excitations are possible in 1D*, as opposed to individual ones. Let us dress a traffic jam analogy to depict this crucial difference with higher dimensions. On a two-lane (or more) road, a single car can acquire speed alone by weaving between the others - this is strictly forbidden on a single-lane road. In 1D quantum systems, particles similarly lose the opportunity to bypass each other, resulting in an impossibility for a singular motion to emerge even at low interaction. As a result, 1D UCAG should not be considered as a first step toward understanding higher dimensions.

On the other hand, in 1D, *quantum fluctuations are significantly enhanced*, meaning that the system will generally struggle to keep its global coherence. A direct consequence is the breaking of long-range order, such as Bose-Einstein condensation. Furthermore, the usual method extensively used in quantum mechanics that relies on the mean-field approach (e.g., Bogoliubov theory, Landau liquid theory) generally fails in 1D. A thriving implication is that new methods [Voit, 1995, Cazalilla et al., 2011] must be invented to deal with these intriguing systems.

Furthermore, 1D UCAG are not only fascinating from a fundamental point of view but also for a rare combination of theoretical and experimental features. Indeed, specific configurations of 1D UCAG are considered one of the few examples of integrable systems accessible experimentally, opening a practical way to investigate integrability and its breaking [Calabrese et al., 2016, Guan & He, 2022]. On a formal side, integrability also implies that one could have control over every step during derivations, hence a deeper understanding of the results. Furthermore, multiple quantities are accessible both experimentally and theoretically, and various parameters can be adjusted. All these parameters could be viewed as knobs, which generally have highly non-trivial effects on the observables. Thereby, UCAG are well-fitted for

benchmark uses or looking forward to building new kinds of more complex quantum simulators. For all these reasons, 1D UCAG should not be viewed as toy models but rather a significant domain of UCAG with its own particularities.

Having discussed the interest in 1D UCAG, let us delve into their practical aspects by briefly outlining the typical experimental scheme.

1.2 Preparing the Lineland journey

To obtain a ready-for-experiment UCAG, some requirements could not be overcome. As a matter of fact, the atoms must be cooled down, trapped (in a 1D, 2D, or 3D geometry), and their interactions must be controlled. It is important to note that each experiment may have unique characteristics and that the following presentation remains an overview. Before going further, the course chosen for this section is worth mentioning. First, we will present the common picture of cooling atoms to ultracold temperatures. Because reaching the 1D regime requires a 3D UCAG, the cooling of 3D gases will be treated beforehand without any loss of generality. Next, we will raise the question of what really characterizes a 1D quantum system. Finally, we will discuss how to experimentally constrain the strength of interaction between atoms and explore the different regimes available. As a side note, these considerations do not constitute the main topic of this thesis and will, therefore, only be touched upon succinctly. For more detail on the cooling of UCAG in 1D, see [Phillips, 1998, Cazalilla et al., 2011, Guan & He, 2022].

1.2.1 Reaching ultracold temperatures with neutral atoms

Atoms are typically obtained by heating a solid block of alkali metals or breaking a gas-filled bulb. It results in the best case of atoms at room temperature and, in the worst, a hot atomic jet. After collimation, this atomic jet is cooled to a few Kelvin, for example, with a Zeeman slower [Phillips & Metcalf, 1982]. Then, atoms will be captured and cooled in Magneto-Optical Trap (MOT) [Raab et al., 1987].

The standard MOT setup is shown in Figure 1.1 and consists of a device combining magnetic forces for the trapping and optical forces for the cooling. Experimentally, the concept for this setup was first demonstrated in [Raab et al., 1987]. On the magnetic side, two magnetic coils generate a magnetic gradient that vanishes at its center of symmetry. While atoms are moving from the center, the Zeeman effect strengthens and pushes the atom toward the center. On the optical side, the cooling relies on the Doppler mechanism [Hänsch & Schawlow, 1975, Wineland & Demhelt, 1975]. The principle relies on laser beams intentionally slightly out-of-sync with ω_0 - the system's resonance frequency - i.e., $\omega_{Laser} = \omega_0 - \Delta\omega$. Because of Doppler shifting, the photons will only interact with particles with velocities directed outside the trap, kicking them toward it. Consequently, the atoms will be effectively cooled down by multiple absorptions and spontaneous emissions to a range of mK up to μK .

Even if this temperature is incomparably colder compared to what we can find in nature, we are still orders of magnitudes away from the ultracold objective. Another mechanism is usually involved to reach this regime: evaporative cooling [Hess, 1986].

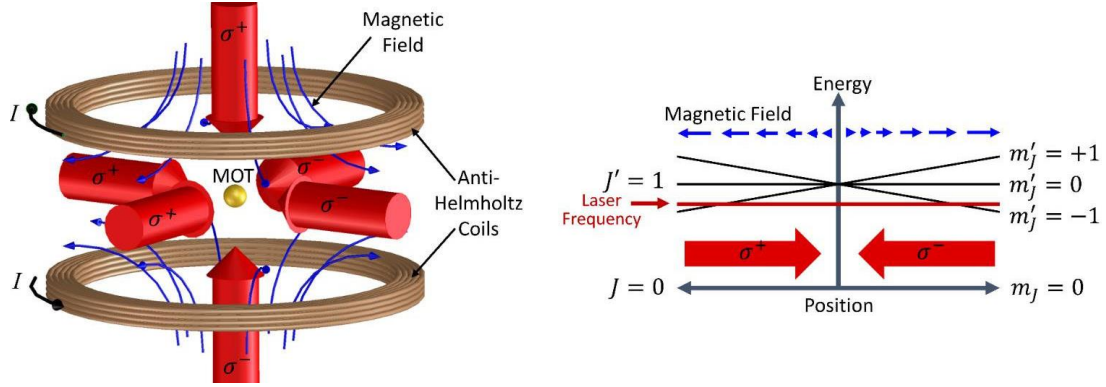


Figure 1.1: (Left) Schematic representation of a MOT. Two anti-Helmholtz coils generate a trapping quadrupolar magnetic field with a zero point at its center, while three counter-propagating circularly polarized laser beams induce Doppler cooling [Hänsch & Schawlow, 1975, Wineland & Demhelt, 1975]. (Right) Diagram depicting the energy levels in the MOT along one axis. On the magnetic side, as far as the particles move away from the trap's center, the Zeeman splitting increases on the $J = 1$ level. On the optical side, the σ_{\pm} incoming light will only interact with the $m'_j = \pm 1$ level. If the laser is slightly out of resonance, the optical force will be directed toward the trap's center, effectively trapping the particles. Figures from [McClelland et al., 2016].

Evaporative cooling refers to the selective removal of high-energy atoms from the trapped sample. This is typically accomplished by slowly lowering the trapping potential, allowing the high-energy atoms to escape and the medium to thermalize along the process.

1.2.2 What is a 1D quantum system?

A 1D system is commonly viewed as a system that shows a preferential direction, in which its size is much larger than the two other directions. That being said, it seems that true 1D systems are, at best, limit cases and, at worst, unrealistic. Nevertheless, the scenario is far more subtle in the domain of quantum mechanics. To gain touch on 1D quantum systems, we will first explore their fundamental aspects and subsequently present the two types of experimental setups that are currently available.

Formally, a 1D system displays a longitudinal size, denoted as L_{\parallel} , which is significantly larger than its transversal sizes, denoted as L_{\perp} . What does this mean for a quantum system from a theoretical perspective? To answer this question, let us examine the energy levels of a quantum box. In this configuration, the excitation levels are quantized and read $E_i = \hbar^2 k_i^2 / 2m$, with $k_i = \pi n_i / L$ the allowed wavelengths, $n_i \in \mathbb{N}^*$ the quantum numbers associated to the excitation level, and $n_i = \parallel$ or \perp . The total energy then takes the ensuing form

$$E = E_0 \left(n_{\parallel}^2 + \frac{L_{\parallel}^2}{L_{\perp}^2} n_{\perp}^2 \right), \quad (1.1)$$

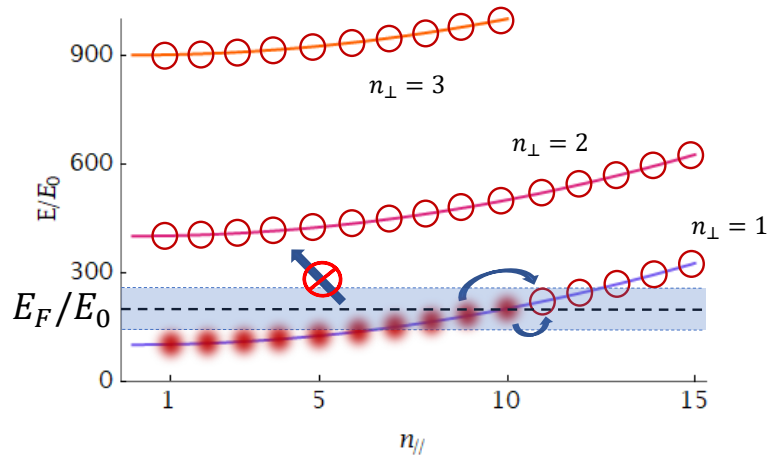


Figure 1.2: First three, rescaled, transversal energy branches E/E_0 of a 1D box as a function of the longitudinal quantum numbers $n_{||}$, as written in Equation (1.1). The dashed line refers to the rescaled Fermi level E_F/E_0 corresponding to 10 trapped particles. The blue zone shows the accessible range of energy for a particle excited during a given process. This pictorial view is adapted from T. Giamarchi's lessons on low dimensional quantum gases at the 2021 session of Boulder summer school [Giamarchi, 2021].

with $E_0 = \hbar^2/8mL_{||}^2$. We suppose now that the system is initially in its ground state (i.e., $n_{||} = n_{\perp} = 1$). During a general process (like scattering, thermal, etc.), particles can be excited within a range of energy of the order of the interaction energy, the temperature, thermal energy, etc. In this situation, we observe that if $L_{||}$ is sufficiently larger than L_{\perp} , only the *longitudinal modes are accessible* through the process, as shown in Figure 1.2. Consequently, the energy dynamic is frozen in the perpendicular axes, effectively rendering the system purely one-dimensional. This picture enlightens us on the fact that too high temperatures, interaction strengths, etc., can push the system beyond the 1D threshold. It also indicates that this specificity is a purely quantum feature. Furthermore, this implies that the total wave function can be expressed in the 1D limit as

$$\Psi(\mathbf{r}) = \psi_{||}(x_1, \dots, x_N)\psi_{\perp}(\mathbf{r}_{\perp 1}, \dots, \mathbf{r}_{\perp N}), \quad (1.2)$$

where $\psi_{\perp}(\mathbf{r}_{\perp 1}, \dots, \mathbf{r}_{\perp N}) = \prod_{i=1}^N \phi_0(\mathbf{r}_{\perp i})$, with $\phi_0(\mathbf{r}_{\perp})$ representing the lowest natural orbital, and $\mathbf{r} = (x, \mathbf{r}_{\perp}) = (x, y, z)$. In this context, $\psi_{\perp}(\mathbf{r}_{\perp 1}, \dots, \mathbf{r}_{\perp N})$ is believed to have a much smoother variation along the main axis, as compared to $\psi_{||}(x_1, \dots, x_N)$, such as the \mathbf{r}_{\perp} dependence of $\Psi(\mathbf{r})$ could be dismissed. Thus, from now on, we will remove the perpendicular and longitudinal indices, and all wave functions will refer to $\psi_{||}(x)$.

Bearing in mind what qualifies 1D UCAG, we can proceed to discuss eventual setups. When it comes to trapping ultra-cold atoms in 1D, there are essentially two methods to consider: optical trapping and magnetic trapping.

As shown in Fig 1.2, the first configuration consists of a counter-propagating combination of waves generating a potential gradient to capture the atoms. The

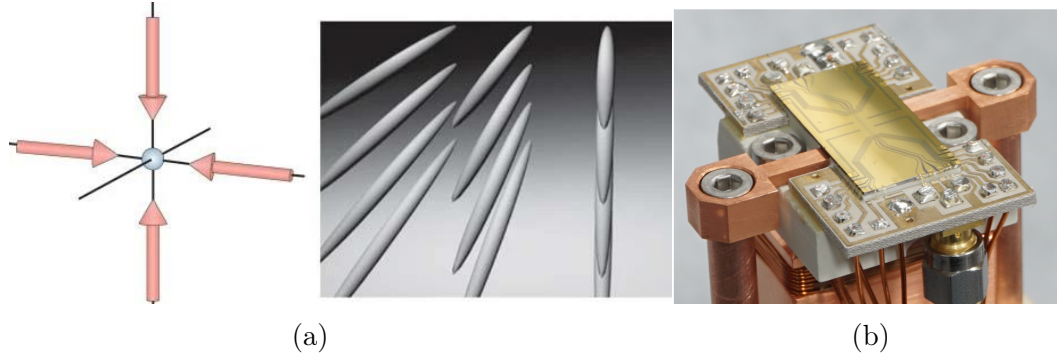


Figure 1.3: (a) Schematic representation of the optical trapping setup and the resulting geometry of the gas. Figure from [Bloch et al., 2000]. (b) Picture of an atomic chip and sub-chip. Image from [Seaward, 2020].

fundamental idea hinges on the dipole force inflicted on the atoms by the laser beams. As atoms move away from the trap's center, the force pulling them toward it increases. Thus, the atoms are trapped in perpendicular directions while free motion is allowed along the longitudinal axis. However, since the trapping potential shows spatial periodicity, a 2D lattice of 1D systems is indeed created, as displayed in Figure 1.3(a). Implementing this setup is generally more straightforward but relatively rigid in terms of modification of the trapping geometry. In addition, isolating a single trap from its neighboring ones can be challenging.

In magnetic trapping, a combination of highly anisotropic magnetic fields is obtained by flowing high-intensity current in wires printed on an atomic chip. For an example of such chipsets, see Figure 1.3(b). By manipulating the magnetic field gradients, the shape of the magnetic potential can be engineered along the desired trapping direction. Similarly to the optical case, trapping is obtained by taking advantage of dipole interactions. Usually more difficult to build, these types of setups allow a single trap of chosen geometry.

Now that we know how to trap 1D UCAG, the last ingredient required for complete control of our systems is managing particle interactions.

1.2.3 Contact interactions tuning: The Feshbach resonance

The following section will briefly outline the experimental technique employed to calibrate interactions. By conveniently modeling the interaction potential, mediating the two-body interactions, we will explain how this description simplifies to a scattering problem with only one parameter - the scattering length. This will help to clarify how precise manipulation over this unique parameter leads to total control of the contact interaction strength g .

For the description of neutral atoms, in 3D, two-body interactions are well represented by the Lennard-Jones potential [Lennard-Jones, 1931, Jones & Chapman, 1924b, Jones & Chapman, 1924a] $V_{LJ}(\mathbf{r}) = A/r^{12} + B/r^6$. However, in the low energy limit, this potential is efficiently described by the so-called Huang's pseudo-potential [Huang & Yang, 1957]

$$U_{Huang}(\mathbf{r}) = g_{3D}\delta(\mathbf{r})\frac{\partial}{\partial r}(r\cdot), \quad (1.3)$$

where $g_{3D} = 4\pi\hbar^2 a_{3D}/m$ is the 3D interaction strength, a_{3D} the 3D s -wave scattering length, and m the particles mass. This description tells that, at low energy, particle scattering is only conveyed by s -waves interactions. Hence, to get a full hand on our system, we must have complete control of a_{3D} . Fortunately, in an external magnetic field, this s -wave scattering process displays a very sharp resonance that can be piloted via magnetic Feshbach resonances.

In quantum mechanics, Feshbach resonances refer to the coupling between two scattering channels of an atom pair controlled by an external magnetic field. These two channels are often called open, for the lowest potential, or closed, for the highest potential, and are both illustrated in Fig 1.5(a). The open - or entrance - channel (V_{bg}), corresponds to free particles moving toward each other, said differently, it is the usual Lennard-Jones potential presented earlier. The closed - or exit - channel (V_C) corresponds to a molecular bound state. Without external intervention, the energy of the closed channel is much higher than that of the open one. However, an external field can modify the energy difference E_C between the two if they possess different internal moments. Precisely, by lowering E_C , it is possible to create a new quasi-bound state, neither free nor molecular, with tunable scattering properties. Effectively, near this resonance, a_{3D} will now highly depend on the magnetic field, as shown in Figure 1.5(b), taking the ensuing form

$$a_{3D}(B) = a_{bg} \left(1 - \frac{\Delta}{B - B_0} \right), \quad (1.4)$$

where a_{bg} is the background scattering, B_0 is position of the resonance, and Δ its width. However, the scattering length in a 3D geometry differs from the scattering length a_{1D} induced by 1D potential. To overcome this issue, the process is to solve the scattering problem associated with $U_{Huang}(\mathbf{r})$, in 1D. By doing so, Olshanii successfully proved that $U_{Huang}(\mathbf{r})$ could accurately be approximated by a Dirac's delta-like potential $U(x) = g_{1D}\delta(x)$ with the tunable interaction strength $g_{1D} = -2\hbar^2/ma_{1D}$ with [Olshanii, 1998]

$$a_{1D} = -\frac{a_{\perp}^2}{2a_{3D}} \left(1 - \mathcal{C} \frac{a_{3D}}{a_{\perp}} \right), \quad (1.5)$$

where $a_{\perp} = \sqrt{2\hbar/m\omega_{\perp}}/|\psi_0(r=0)|$ with ω_{\perp} the transverse pulsation and $\mathcal{C} = 1.4603\dots$. With this celebrated result, we find again that, in 1D, particles are unaware of each other until they collide (as in 3D). According to this analysis, the scattering length a_{1D} appears to be the sole factor governing our 1D two-body interactions problem at low energy. Moreover, we see from Equation (1.4) that *any value can be chosen for the scattering length*. Thus, a range of interactions going from $-\infty$ to ∞ is, in principle, accessible experimentally. Before continuing, we will drop the scattering length indices as we always work in 1D.

As a side note, it is worth mentioning that the interaction can also be increased by diminishing the density of the gas. This astonishing property is another unique feature circumscribed to 1D UCAG. To understand this behavior, let us compare

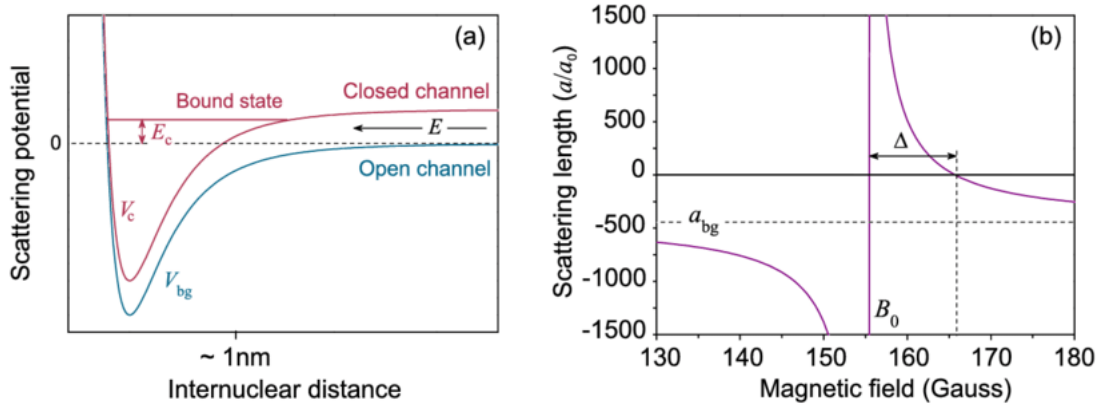


Figure 1.4: (a) Illustration of the two interaction potentials associated with the open channel (V_{bg}) and the close channel (V_C), as a function of the internuclear distance. Considering a pair of particles colliding with energy E , a Feshbach resonance is expected for E close to E_C , the energy of a closed channel bound state. (b) The Feshbach resonance found in the state $F = 2, m_F = -2$ of ^{85}Rb . Figures from [Billam et al., 2013].

the scaling of the interaction energy E_{int} and the kinetic energy E_k . The former scales as $E_{int} \sim gn$ while the latter grows as $E_k \sim n^2$, with n the linear density of the gas. By looking at the energy ratio, one can construct an interaction parameter $\gamma \sim E_{int}/E_k \sim g/n$, which characterizes the interaction regimes. This parameter enlightens that *lowering the density constitutes an alternative lever arm for reaching high interaction regimes*.

We have provided insight into achieving ultra-cold temperatures, trapping atoms in 1D geometries, and adjusting the interaction. It is now possible to explore the possibilities that this setup offers.

1.3 Models and preliminary solutions

In this section, we will introduce the general model used throughout the document and show primary examples of solutions that will prove helpful later on. For this, we have chosen to focus on homogenous configurations. Specifically, we will look at ring-shaped traps, described by Periodic Boundary Conditions (PBC), and box-shaped traps, described by Dirichlet Boundary Conditions (DBC). The Hamiltonian for identical particles with contact interactions in the homogeneous case can be expressed as follows

$$\hat{H} = - \sum_{i=1}^N \frac{\hbar^2}{2m} \frac{\partial^2}{\partial x_i^2} + g \sum_{j>i}^N \delta(x_i - x_j), \quad (1.6)$$

where N is the total number of particles, and m , their mass. Before proceeding, it is important to note that s -wave scattering is absent for identical fermions. As a result, the interaction term is inexistent in this case. To put it differently, the Pauli

principle already prohibits contact for identical fermions. Regarding interactions, two main regimes could be distinguished: the attractive regime with $g < 0$ and the repulsive regime with $g > 0$. For the purpose of this document, we will focus exclusively on the repulsive potential.

Before presenting some preliminary solutions, it is worth emphasizing that this seemingly simple model encompasses a vast zoology of models. For instance, Equation (1.6) reduces to a free Hamiltonian without interactions. For identical bosons, it leads to the Lieb-Liniger Hamiltonian [Lieb & Liniger, 1963]. For spin- $\frac{1}{2}$ fermions, it becomes the Gaudin-Yang Hamiltonian [Yang, 1967, Gaudin, 1976]. All these Hamiltonian are integrable, and thus, exact solutions can be found. In the ensuing part, we will briefly present the scenario involving free particles and strong interactions, leaving a more comprehensive explanation for upcoming chapters. To be precise, details on single species model (including Lieb-Liniger solutions) can be found in Chapter 2, while spin mixtures (including the Gaudin-Yang solutions) will be outlined in Chapter 3. For thorough reviews of the results obtained in the domain, the interested reader can see [Cazalilla et al., 2011, Minguzzi & Vignolo, 2022, Guan & He, 2022].

1.3.1 Non-interacting identical particles

The typical approach is to start with the free Hamiltonian's one-particle solutions to compute the many-body wave function. These solutions are called natural orbitals and will be denoted as $\phi_n(x)$, with n the excitation level of the particle. Once obtained, they serve as building blocks for the many-body wave function, with the final structure dictated by the particle statistic. For clarity, we will separately present the fermionic and bosonic solutions.

Non-interacting Spinless Fermions (SF):

For identical fermions without interaction, the total wave function must be anti-symmetric under the swapping of particles. This condition could be satisfied in a concise way using the so-called Slater's determinant

$$\Psi_{SF}(x_1, \dots, x_N) = \frac{1}{\sqrt{N!}} \det[\phi_m(x_n)]. \quad (1.7)$$

Particle on a L length ring present orbitals of the type $\phi_m(x_n) = e^{ik_m x_n} / \sqrt{L}$, $n, m \in 1, \dots, N$, with $k_m = 2\pi(m - \frac{N+1}{2})/L$ for odd N and $k_m = 2\pi(m - \frac{N}{2})/L$ for even N , with $x_n \in [-L/2, L/2]$. On the other hand, for particles in a box of length L , $\phi_m(x_n) = \sqrt{2/L} \sin[k_m(x_n + L/2)]$ are natural orbitals with $k_m = m\pi/L$, $x_n \in [-L/2, L/2]$ and $n, m \in \{1, \dots, N\}$.

Non-interacting spinless bosons:

In opposition with fermions, non-interacting identical bosons could occupy the same energy state, leading to the following many-body wavefunction

$$\Psi(x_1, \dots, x_N) = \prod_{n=1}^N \phi_0(x_n). \quad (1.8)$$

Notably, these cases will represent a cornerstone for most of the present document. In particular, the case of spinless non-interacting fermions will deliver an elegant way to treat strong interactions, as we will see right after.

1.3.2 Strong interaction limit

In most quantum systems, the treatment of strong interactions is usually simplified or even avoided. Again, 1D UCAG exhibits a unique feature by being more manageable in this regime - compared to arbitrary g - and even leading to exact solutions. On top of that, this limit provides crucial information about how contact interaction impacts the nature of the gas. Therefore, a short investigation of the wavefunction would be valuable at this early stage, while the comprehensive approach will be kept for the upcoming chapters.

Only bosons are concerned here because contact interactions are forbidden for identical fermions. Formally, the strong interactions regime is obtained by pushing interactions up to infinity (i.e., $g \rightarrow \infty$). In this limit, bosons experience such a high repulsion that they can no longer occupy the same position. This new behavior artificially mimics the effects of the Pauli principle. Driven by this idea, Girardeau [Girardeau, 1960] successfully built the many-body wavefunction by mapping on Ψ_{SF} , capitalizing on its Slater's determinantal form, which inherently prevents particles overlap. The total wave function is then obtained by imposing the overall swapping symmetry by adjoining a sign function to every possible permutation of variables. It results in the ensuing Tonks-Girardeau Bosons' (TB) wavefunction

$$\Psi_{TB}(x_1, \dots, x_N) = \prod_{1 \leq i < j \leq N} \text{sign}(x_i - x_j) \Psi_{SF}(x_1, \dots, x_N). \quad (1.9)$$

This mapping on non-interactive spinless fermions is commonly called fermionization, which could be misleading. Although these two types of gas share similarities, their differences are still substantial.

The foundation papers on the TB gas date back to the 60's [Girardeau, 1960, Lenard, 1964, Lenard, 1966]. Since then, this area has been extensively explored, with many notable achievements discussed in Chapter 2, and fully documented in [Bloch et al., 2008, Cazalilla et al., 2011]. Despite early progress, it was not until the 2004 that experimental observation of a TB gas was achieved [Paredes et al., 2004, Kinoshita et al., 2004]. This breakthrough allowed researchers to explore the accessibility of a TG gas, as it is only asymptotically exact from a theoretical perspective. Fortunately, these modern accomplishments have shown that strong interactions are far from inaccessible. In particular, interactions of the order of $\gamma = 10$ are adequate for being classified as strongly interactive [Olshanii, 1998, Kinoshita et al., 2004, Kinoshita et al., 2005, Rizzi et al., 2018], as displayed in Figure 1.5.

Both SF and TB models are remarkably convenient to treat. However, we still lack crucial elements: what and how can information on the system's properties be earned? The final section of this introduction will address this question, including both theoretical and experimental considerations.

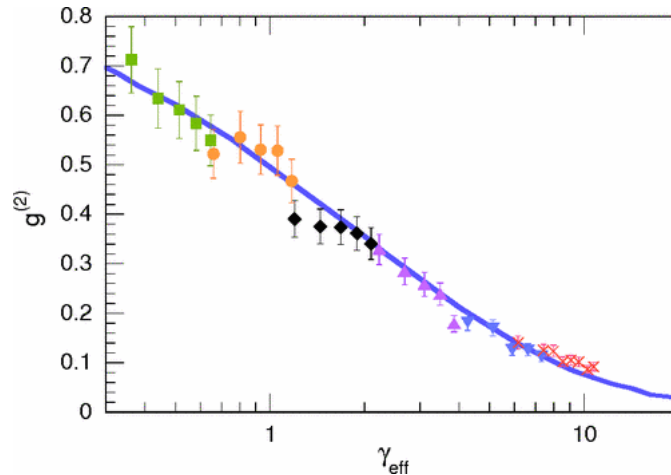


Figure 1.5: Evolution of the local pair correlations $g^{(2)}$ with the interaction parameter γ_{eff} . The multiple points stand for separate experimental realization. The solid line refers to the expectation from a 1D Bose gas theory. For a dense, weakly interacting, gas ($\gamma \ll 1$) the $g^{(2)}$ is close to one, similarly to standard 3D BEC. As far as the interactions increase, the $g^{(2)}$ is decreasing, ultimately going to 0 for $\gamma \gtrsim 10$. This behavior is analogous to 1D identical fermions, betraying that the TB regime has been reached. This figure is taken from [Kinoshita et al., 2005].

1.4 Correlations investigation

When conducting research on UCAG, scientists have access to numerous quantities to probe or compute. Thereby, careful consideration is given to selecting the most appropriate observable. In this section, we will focus on two, both relying on the same concept: correlations. Particularly, we will examine these correlations in real and Fourier space, introducing the correlation functions and momentum distribution. After presenting these two aspects, we will provide a notable example of their success.

1.4.1 Correlations in real space: The correlation functions

The history of correlations is a wonderful journey that entangled mathematics and physics. They are at the heart of numerous intellectual and technological advancements. Indeed, correlations have led to groundbreaking discoveries in various disciplines, such as medicine and social or environmental sciences. These fields often face complex questions implicating numerous variables. In such demanding environments, correlations constitute a salvatory tool to address problems.

The concept of correlations was first introduced by Galton [Galton, 1889], who became curious about the link between the size of sweet peas and the one of their offsprings [Galton, 1877]. F. Galton realized the potential significance of this new field of research from the outset but left further investigations to "any competent person who cares to investigate it" [Galton, 1889]. The first worth continuing F. Galton's works was his colleague and friend K. Pearson. For instance, he proficiently studied a base ground quantity for correlations, later named after him as Pearson's r . This quantity is likely the most immediate when discussing correlations, and it

can be expressed as follows

$$r = \frac{\sum_i (x_i - \bar{x})(y_i - \bar{y})}{\sqrt{\sum_i (x_i - \bar{x})^2 \sum_i (y_i - \bar{y})^2}}, \quad (1.10)$$

where x_i , and y_i are the values that takes the quantities x , and y for their i -th observations, while \bar{x} , and \bar{y} are their mean values. Indeed, Pearson's r simply quantifies the linear co-evolution between two different sets of observations. Precisely, if $r = 1$ (reps. -1), an increase of x by an arbitrary value will provoke the same increase (reps. decrease) by the same value on y . This linked behavior is the essence of correlations, *the characterization and quantification of how random variables are related*.

Over the years, substantial mathematical improvement has enhanced this field [Fisher, 1915, Wiener, 1933, Hotelling, 1936, Wiener, 1938, Shannon, 1948]. Alongside, physics has taken advantage of these new means, and the ease brought by correlations has imbued in numerous domains. For instance, in matter physics or chaotic and dynamical systems. In these, correlations are typically used for two main reasons: 1) to understand how the constituent relationships of a system contribute to its global behavior and 2) to clarify the interdependence of quantities in complex systems. Bearing in mind these benefits, let us delve into its particular use of correlations in our systems.

In quantum mechanics, correlations are essential for several reasons. At first, quantum fluctuations cause for all the particles' properties to be probabilistic. This stochastic essence imposes to consider not only one quantum state but the statistical behavior over multiple realizations. Moreover, all these quantities are intrinsically linked, for example, due to the uncertainty principle. As a consequence, their fundamental connections will have tremendous implications and can not be overcome. On top of that, quantum systems are known to be the theater of highly non-local phenomena such as entanglement. Therefore, characterizing the relation between multiple system regions will be required to understand global behaviors. For all these reasons, quantum mechanics is a perfect realm of knowledge to benefit the toolbox that represents correlations. However, a question remains: how to probe correlations in a 1D UCAG experiment?

To handle this question, the analogy with optical physics can be insightful. In typical experiments, the idea is to halve an incoming wave into two distinct paths. It results in two waves, which will be superposed afterward at the end of the setup, creating interferences. By adjusting the distance of one path, the coherence of the initial light can be scanned. Coherences are correlations of the same quantity (in this example, the electric field) between different positions, time,s etc. Precisely, the changes in the interference pattern is directly related to a coherence function. This can be seen throughout the formal expression of the first-order coherence function [Glauber, 1963]

$$g^{(1)}(x, y) = \frac{\mathcal{E}^*(x)\mathcal{E}(y)}{\langle |\mathcal{E}(x)|^2 \rangle}, \quad (1.11)$$

which basically indicates how the value of an electric field $\mathcal{E}(x)$ in a position x is connected to its value in y , while the mean value $\langle \dots \rangle$ is taken over numerous

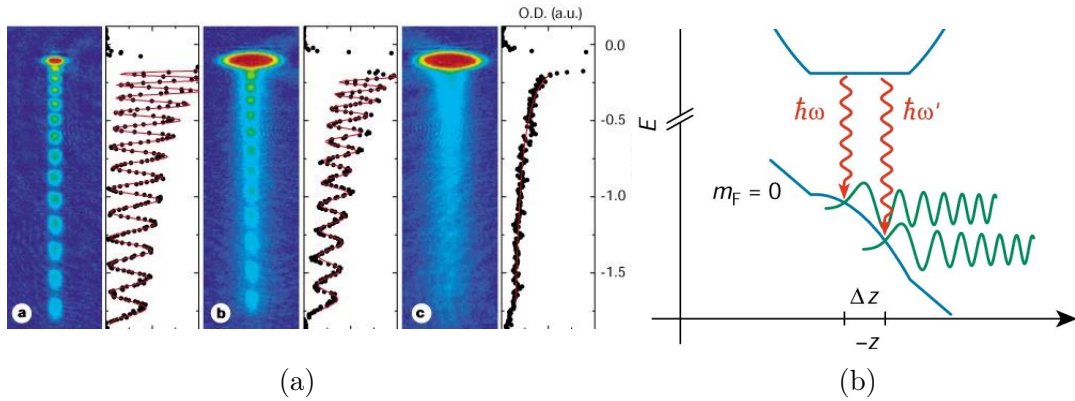


Figure 1.6: Investigation of a 3D Bose gas coherence along phase transition (a) Left panels. Interference pattern in false color obtained by absorption. Right panels: Vertical cut at the center of the left panels. Three results are present for three different temperatures, from left to right $T \ll T_C$, $T < T_C$, and $T > T_C$, with T_C the critical temperature of the gas. (b) Explanation of the mechanism. This experiment involves the $m_F = -1$ (trapped) and the $m_F = 0$ (untapped) atomic state; see Fig 1.1 for details. Through a radio-wave field combining two frequencies (red lines), initially confined atoms can be transferred to a free state in two distinct locations within the trap. This process effectively creates two slits in the trap, separated by a Δz distance. Figures from [Bloch et al., 2000].

repetitions. With light waves, the typical setup uses Young's slits or beam splitter for the duplication. However, while a bunch of photons is quite inclined to split, one can wonder how to obtain the same result with a gas of massive particles. Although not as straightforward, double-slit analog experiments have been realized, as shown in Fig 1.6. In this case, the corresponding one-body correlation function for matter waves reads

$$\rho_1(x, y) = N \int_{\mathcal{D}^{N-1}} \prod_{n=2}^N dx_n \Psi(x, x_2, \dots, x_N) \Psi^*(y, x_2, \dots, x_N), \quad (1.12)$$

here constructed via the wave function Ψ instead of $\mathcal{E}(x)$, with $\int_{\mathcal{D}} dx \rho_1(x, x) = N$, and where \mathcal{D} , is the spatial domain accessible to the particles. The diagonal part $\rho_1(x, x) = n(x)$ represents the one-particle spacial distribution, namely the probability density to find a particle in x , while the off-diagonal part represents the coherences. This function is also named density matrix because of its diagonal part and could be generalized to any order, as we will see in the next chapter.

As illustrated in Figure 1.6, obtaining a correlation function in real space is a complex process, explaining the limited instances of realizations. Consequently, despite its theoretical suitability, one can reasonably ask for a more convenient object to consider experimentally. Fortunately, a quantity conveys similar insights with significantly greater accessibility: the momentum distribution.

1.4.2 Correlations in Fourier space: The momentum distribution

A natural way to circumvent the difficulty of obtaining correlations in real space is to move the analysis toward momenta. Also convenient to treat theoretically, the momentum distribution is only the Fourier transform of the first-order correlation function

$$n(k) = \frac{1}{2\pi} \int_{\mathcal{D}^2} dx dy \rho_1(x, y) e^{ik(x-y)}, \quad (1.13)$$

This function represents the probability density to find a particle having a momentum k . Because the momentum distribution is only a Fourier transformation of ρ_1 it conveys the same information (naturally to an inversion of scale). In the last part of this introductory chapter, we want to briefly touch upon $n(k)$ potentiality, leaving a more comprehensive exploration to Chapter 2. For this purpose, let us consider the two main parts of the momentum distribution: the zeroth momentum distribution and its tail.

Because we have moved to Fourier space, long-distance coherences are carried by the low momentum part of the distribution and, in particular, are quantified by the zeroth momentum distribution n_0 . In particular, this quantity is connected to the global order of the system. Consequently, it constitutes an indicator of some phase transition of the system, such as condensation-like [Ribeiro et al., 2013, Henkel et al., 2017] or superfluid-Mott insulator phase transition [Greiner et al., 2002]. On the other hand, short-distance correlations will impact the large k behavior of the momentum distribution. Precisely, in this region, we can perceive how particles overlap or, in cases of strong repulsions, their brushing against each other. In a less evident way, information regarding the system's symmetry is also included here. As in 1D, particle swapping only involves the immediate next neighbors, so this swapping becomes a purely short-distance phenomenon. Consequently, the effect of the particles' symmetry under these exchanges is carried by the large k distribution of $n(k)$ [Decamp et al., 2016a]. This interplay between interactions and symmetries gives rise to fascinating phenomena that will be investigated deeply in Chapter 3 and Chapter 4.

To conclude, among all possible observables, $n(k)$ is one of the most accessible experimentally. The method usually employed is the so-called time-of-flight. The idea is pretty simple: by turning off the trapping potential and letting the gas expand ballistically, if the interactions become negligible, the position of the particles after a time $\tau \gg mL^2/\hbar$ can be mapped on the initial velocity distribution inside the trap. A significant example of such probing realization in the case of spin mixtures is presented in Figure 1.7.

We have covered the different types of systems that we will be concentrating on. We have discussed the significance of UCAG and the usual approach for their implementation. We have also examined the unique characteristics of the 1D configuration, both in theory and experiments. Furthermore, we have introduced the specific model that will be analyzed in this document and some preliminary solutions. Lastly, we have explained how to obtain information about the system

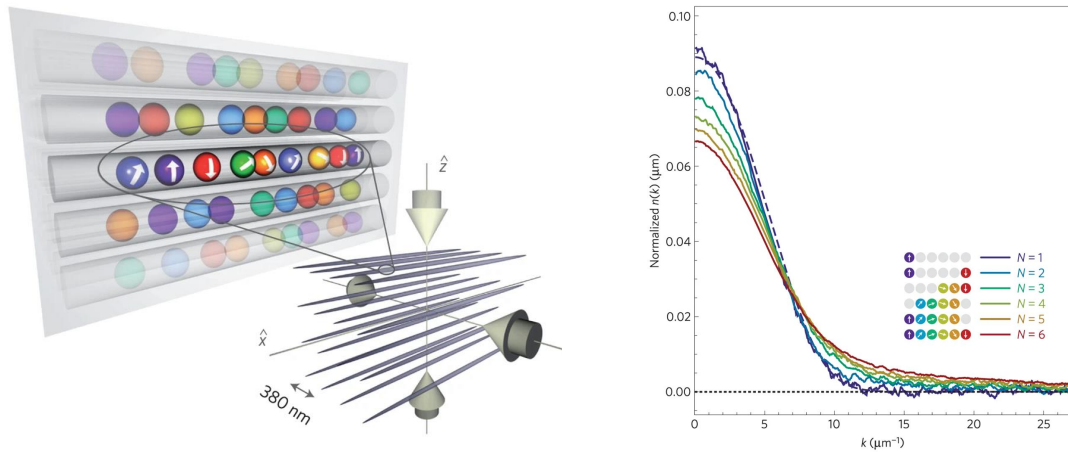


Figure 1.7: First instance of harmonically confined 1D fermionic spin mixtures of 6 different species [Pagano et al., 2014]. (Left) Schematic representation of the setup, which pictures the geometry of the optically trapped array of gases. (Right) Momentum distribution of the gas for different types of fermionic mixture. Solid line: experimental results obtained by time-of-flight absorption imaging. Dashed lines: Theoretical results obtained via ideal Fermi gas theory for $N = 1$ (the total number of species); an overall averaging is performed over the inhomogeneous distribution of atoms in the different traps.

and described two corresponding experimental setups. We will now proceed to the treatment in detail of a particular case: identical particles.

Chapter 2

Ultracold atomic gases of identical particles

In this chapter, we will discuss the effective treatment of 1D UCAG. We will focus on single-species gases as a warm-up for future, more complex systems. Our initial step will be to derive an exact, general, solution from our model, giving us a taste of actual computation. We will then obtain real and Fourier space correlation functions and examine their properties. Throughout this chapter, we will pay special attention to extreme cases, such as non-interacting particles or strong repulsion regimes, which will serve as the foundation for future discussions.

2.1 A first exact solution

Let us proceed into our first theoretical treatment of 1D UCAG with contact interaction between particles. We will present the solution of the Hamiltonian Equation (1.6) for two geometries, a ring-shaped trap (PBC) and a box-shaped trap (DBC). As a kind reminder, this Hamiltonian stands only for bosons, as contact interactions are inexistent between spinless fermions. The corresponding Hamiltonian is the so-called Lieb-Liniger and reads

$$H = -\frac{\hbar^2}{2m} \sum_{i=1}^N \frac{\partial^2}{\partial x_i^2} + g \sum_{1 \leq i < j \leq N} \delta(x_i - x_j). \quad (2.1)$$

The general method for solving this model is usually throughout Bethe ansatz [Bethe, 1931]. In the next section, before tackling the N -body problem, we will gently begin with two particles.

2.1.1 The two-body problem

The Schrödinger equation that corresponds to the Hamiltonian Equation (2.1) for two spinless interacting bosons reads

$$\left[-\frac{\partial^2}{\partial x_1^2} - \frac{\partial^2}{\partial x_2^2} + 2c\delta(x_1 - x_2) \right] \Psi(x_1, x_2) = \epsilon \Psi(x_1, x_2), \quad (2.2)$$

20 Chapter 2. Ultracold atomic gases of identical particles

with $c = \frac{mg}{\hbar^2}$ the scattering strength, and ϵ the energy in unit of $\hbar^2/2m$. The general textbook solution of this differential equation reads

$$\Psi(x_1, x_2) = f(x_1, x_2)\theta(x_1 - x_2) + f(x_2, x_1)\theta(x_2 - x_1), \quad (2.3)$$

with $\theta(x) = 1$ if $x > 0$, and 0 elsewhere. This result is independent of the chosen trapping geometry, and solely the form of f will change with the boundary conditions. Given the significant impact of boundary conditions on the solution, we will address them individually.

Periodic boundary condition

Away from the contact region $x_1 = x_2$, the solution must be the same as for free particles. Said differently, in the sector $x_1 \leq x_2$, the wave function is only a superposition of plane wave

$$f(x_1, x_2) = A_{12}e^{i(k_1x_1+k_2x_2)} + A_{21}e^{i(k_2x_1+k_1x_2)}, \quad (2.4)$$

where the A 's are the amplitudes and the k 's are called charge rapidities. The solutions in other sectors are obtained using the statistic of identical bosons (i.e., $\Psi(x_1, x_2) = \Psi(x_2, x_1)$). The charge rapidities are interpreted as the asymptotic momentum of the particles once the trap is turned off. The amplitudes and rapidities are yet to be determined and will be fixed based on the system's properties. The first step is to employ the usual cusp condition to establish a relationship between them. This condition can be obtained from the Schrödinger equation. The approach is to move in relative and center of mass coordinates and integrate around the non-analyticities introduced by the $c\delta$ interaction potential. This method leads to the following two particles' cusp condition

$$\left[\frac{\partial \Psi}{\partial x_1} - \frac{\partial \Psi}{\partial x_2} \right]_{x_1-x_2=0^+} - \left[\frac{\partial \Psi}{\partial x_1} - \frac{\partial \Psi}{\partial x_2} \right]_{x_1-x_2=0^-} = c\Psi \Big|_{x_1-x_2=0}. \quad (2.5)$$

Inserting the Equation (2.4) ansatz it follows

$$i(k_1 - k_2) [A_{12} - A_{21}] = c [A_{12} + A_{21}], \quad (2.6)$$

which implies that the amplitudes obey the relation

$$\frac{A_{12}}{A_{21}} = \frac{k_1 - k_2 + ic}{k_1 - k_2 - ic} = -e^{i\vartheta(k_1-k_2)}, \quad (2.7)$$

where $\vartheta(x) = -2 \arctan x/c$, and $\vartheta(x) + \pi$ is the phase shift induced by the $c\delta$ scattering potential. We can make the connection with quantum scattering theory, where the ratio Equation (2.7) is commonly expressed with the scattering matrix as $S(k_1, k_2) = S(k_1 - k_2) = e^{\vartheta(k_1-k_2)+\pi}$. At this point, it is too early to make any sweeping statements about the system. We can instead perform a basic check and verify if this solution includes the results discussed earlier. The non-interacting case is rather trivial, so we can proceed directly to the high repulsive limit.

Tonks-Girardeau regime $c \rightarrow \infty$:

In this regime, Equation (2.7) imposes $A_{12} = -A_{21}$, which imply that the phase shift at $c \rightarrow \infty$ is equal to π . In simple terms, the Dirac potential does not scatter in 1D. Thus, the global form of the wave function in a sector, Equation (2.4), becomes $f(x_1, x_2) = e^{ik_1x_1}e^{ik_2x_2} - e^{ik_2x_1}e^{ik_1x_2}$ which is the SF wave function, up to a normalization constant. Noticing that $f(x_1, x_2) = -f(x_2, x_1)$, the complete wave function then takes the expected TB form $\Psi(x_1, x_2) = \text{sign}(x_1 - x_2)\Psi_{SF}(x_1, x_2)$, shown in Equation (1.9).

We can now move to the slightly more complex DBC configuration.

Hardwall boundary conditions

For DBC, the process will be similar. The only difference is that hard walls induce complete reflections, and the superposition must now be taken with all incident and reflected plane waves [Batchelor et al., 2005]. As a consequence, in the sector $0 < x_1 \leq x_2 < L$ the solution takes the form

$$\begin{aligned} f(x_1, x_2) = & A_{12}(k_1, k_2)e^{i(k_1x_1+k_2x_2)} + A_{12}(-k_1, -k_2)e^{i(-k_1x_1-k_2x_2)} \\ & - A_{12}(k_1, -k_2)e^{i(k_1x_1-k_2x_2)} - A_{12}(-k_1, k_2)e^{i(-k_1x_1+k_1x_2)} \\ & - A_{21}(k_1, -k_2)e^{i(-k_2x_1+k_1x_2)} - A_{21}(-k_1, k_2)e^{i(k_2x_1-k_1x_2)} \\ & + A_{21}(k_1, k_2)e^{i(k_2x_1+k_1x_2)} + A_{21}(-k_1, -k_2)e^{i(-k_2x_1-k_1x_2)}. \end{aligned} \quad (2.8)$$

In this scenario, the DBC have introduced a new constraint which reads as follows $A(k_1, \dots, k_N) = A(-k_1, \dots, -k_N)$, where the minus signs represent completely reflected plane waves. This new feature allows for two types of ratios between amplitudes, one now involving reflected waves. By utilizing the cusp condition once more, we can derive the two equivalents of Equation (2.7) for DBC

$$\frac{A_{12}(k_1, k_2)}{A_{21}(k_1, k_2)} = \frac{k_1 - k_2 + ic}{k_1 - k_2 - ic} = -e^{i\theta(k_1-k_2)}, \quad (2.9)$$

$$\frac{A_{12}(k_1, -k_2)}{A_{21}(k_1, -k_2)} = \frac{k_1 + k_2 + ic}{k_1 + k_2 - ic} = -e^{i\theta(k_1+k_2)}, \quad (2.10)$$

which provides the following structure for the two types of amplitudes

$$A_{12}(k_1, k_2) = (k_1 - k_2 + ic)(k_1 + k_2 - ic), \quad (2.11)$$

$$A_{12}(k_1, -k_2) = (k_1 + k_2 + ic)(k_1 - k_2 - ic). \quad (2.12)$$

It should be pointed out that these amplitudes must be normalized to be dimensionless. Similarly to the PBC, we can perform a first validation by considering the strong interaction limit.

Tonks-Girardeau regime $c \rightarrow \infty$:

Again, the amplitudes are just inverted by the scattering (i.e., π phase shift), and we get $A_{12} = -A_{21}$ regardless of the rapidity pair. The wave function in the first sector, Equation (2.8), gives $\Psi(x_1, x_2) = 4 \sin k_1x_1 \sin k_2x_2 - 4 \sin k_2x_1 \sin k_1x_2$, which is unsurprisingly a Slater's determinant. By incorporating the relationship between

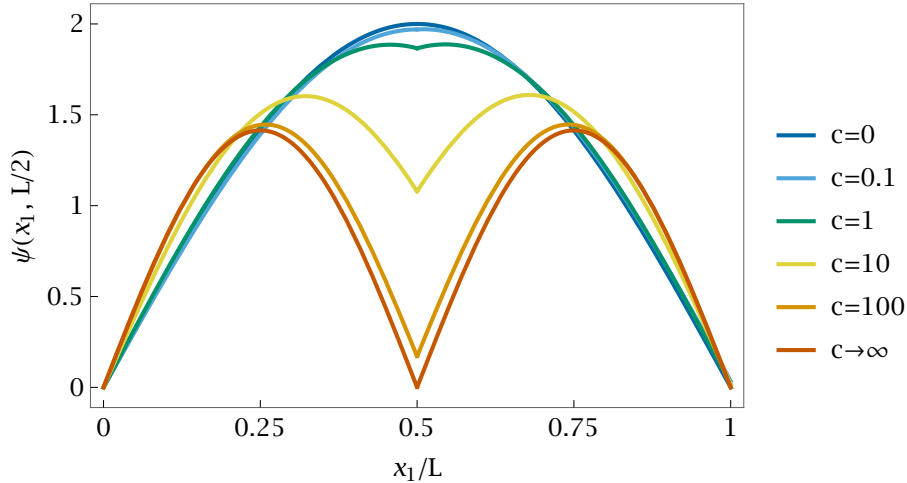


Figure 2.1: Wave function for two particles in a box-shaped trap. The position variable x_2 has been fixed to 0, and the plot is a function of the other, x_1 . The different curves correspond to increasing interaction strength $c = mg/\hbar^2$ to highlight the effect of interaction on the cusp of the wave function.

sectors $f(x_1, x_2) = -f(x_2, x_1)$ and returning to the complete wave function, Equation (2.4), we can find the searched TB wave function, Equation (1.9).

Although these manipulations are still in the early stage, they suggest that diffusive effects may fully explain the behavior of interacting hardcore bosons. It also appears that the cusp of the wave function conveys these diffusive effects. To enlighten this property, we can take a closer look at the evolution of the wave function with the interaction strength. As depicted in Figure 2.1, the increase of interaction gradually digs a cusp where particle positions coincide, revealing the enhancement of diffusive effects. This cusp is a fundamental element of contact interaction and will have a predominant place throughout this document. With that in mind, we can now increase the number of particles to ascertain the general form of the rapidities and amplitudes.

2.1.2 The many-body problem

The strategy employed for two particles can be extended to the N -body case and then will only be partially elaborated. The derivation will be divided as follows. First, we will guess the form of N -body wave function ansatz. Following a similar process to the two-body case, the cusp condition will provide a relation between amplitudes and rapidities. Consecutively, we will obtain a set of linked equations for the rapidities using boundary conditions. Finally, the strong interaction limit will furnish the last ingredient to solve the system completely.

Periodic boundary conditions

We can begin with the most simple case of a ring-shaped trap. The solution must still be a superposition of plane waves away from the contact region. Hence, the N -body wave function is simply the generalization of Equation (2.4) which in the

sector $x_1 < \cdots < x_N$ reads

$$\Psi(x_1, \cdots, x_N) = \sum_P A_P(\{k_i\}, c) e^{i \sum_j k_{P(j)} x_j}, \quad (2.13)$$

where the amplitudes $A_P(\{k_i\}, c)$ refer to the $N!$ possible momentum configurations of the $N!$ plane waves, and P now refer to a permutation inside S_N , the permutation group of N distinct elements. As a side note, the wave function can equivalently be expressed as $\Psi(x_1, \cdots, x_N) = \sum_P A_P(\{k_i\}, c) e^{i \sum_j k_j x_{P(j)}}$, and for instance, will be preferred in the next chapter. From now on, we will also drop the k_i 's and c dependences of the A_P 's seeking conciseness.

We now employ the general procedure to determine the $N!$ amplitudes, starting with the cusp condition stated in Equation (2.5). The cusp condition obtains for neighboring particles labeled 1 and 2 and can be extended for any couple labeled as j and $j+1$ (in the now N -body system). Formally, applying the cusp condition between two particles corresponds to an application across the boundary between two sectors. One sector has the two neighbors in a given order, let us say $x_1 < \cdots < x_j < x_{j+1} < \cdots < x_N$, and the other sector has the two particles swapped, here $x_1 < \cdots < x_{j+1} < x_j < \cdots < x_N$. Thus, for a permutation of type $Q = \tau_{j,j+1}P$, where $\tau_{j,j+1}$ is the transposition of the two elements j and $j+1$, the cusp condition leads to

$$\frac{A_P}{A_Q} = \frac{k_{P(j)} - k_{P(j+1)} + ic}{k_{P(j)} - k_{P(j+1)} - ic} = -e^{-i\vartheta(k_{P(j)} - k_{P(j+1)})}, \quad (2.14)$$

which again physically represents the scattering of two next-neighbor particles. Now, one can verify that a solution to this set of equations is

$$A_P = \prod_{1 \leq j < l \leq N} \left(1 + \frac{ic}{k_{P(j)} - k_{P(l)}} \right). \quad (2.15)$$

In order to determine the N rapidities and benefit from the boundary condition, we must analyze the sequential scattering between each particle from the first to the N -th. It corresponds to searching the ratio between an arbitrary plane wave with amplitude A_P and a second with $A_{P'}$, where $P' = (P(N), P(1), \cdots, P(N-1))$. Using the PBC over the first variable, one can find that $A_P e^{ik_{P'(1)}L} = A_{P'}$ which leads to the so-called Bethe equations

$$e^{ik_j L} = (-1)^{N-1} \prod_{j \neq l} \frac{k_j - k_l + ic}{k_j - k_l - ic}. \quad (2.16)$$

Usually, to solve this non-linear system of equations, it is more convenient to take its logarithm variant

$$k_j L = 2\pi I_j + \sum_{l \neq j} \vartheta(k_j - k_l), \quad (2.17)$$

where we have used $\ln \prod_k (\cdot) = \sum_k \ln (\cdot)$, Equation 2.14 to make the $\vartheta(k_j - k_l)$ dependency explicit, and finally the relation $\ln (-1)^a = a + cte$ to obtain the Bethe quantum number I_j 's. These odd or half-odd numbers (depending on N 's parity) define the rapidities - thus the total momentum $P = \sum_j k_j$, and the energy $E = \sum_j k_j^2$ - of the system. We have technically solved our model, but one must be careful as not every set of I_j 's leads to a physical solution. In order to obtain the I_j 's selection rules, let us begin with the limit case of infinite interaction.

Tonks-Girardeau regime $c \rightarrow \infty$:

We recall that $\vartheta(k) \rightarrow 0$ in this limit, so according to Equation (2.17), k_j must be equal to $2\pi I_j/L$. On its side, Equation (2.14) imposes $A_P = \pm 1$. Hence, the collection of rapidities must be distinct to prevent the wave function from vanishing. This can be transcript in terms of quantum numbers by the inequality $I_j \neq I_l$, for all $j \neq l$. Once again, we encounter the direct consequence of the interaction potential preventing particles from occupying the same place (or having the same energy) and mimicking the Pauli principle.

The ground state Bethe quantum numbers can now be found by minimizing the total energy and momentum. These conditions impose a symmetric repartition of the I_j 's without holes

$$I_j = -\frac{N+1}{2} + j, \quad j = 1, \dots, N, \quad (2.18)$$

which describes a well-known Fermi sphere, enforcing the analogy with SF. On the other hand, one can describe charge excitations by creating holes in the j 's distribution. These results hold even beyond the asymptotic case. It has been proven [Korepin et al., 1993] that the I_j 's values must remain independent of c for $c > 0$. Consequently, the Bethe quantum number will remain unchanged for any positive scattering strength.

It is important to note that the non-interacting case is not included in this formalism and may cause confusion so we will address it promptly. In the non-interactive regime, Equation (2.14) requires all amplitudes A_P to be the same. Therefore, nothing now imposes for the I_j 's to be different. By utilizing this criterion to rebuild the complete wave function, we end up with Equation (1.8), the previously introduced non-interacting spinless bosons' wave function.

The ring-shaped geometry is completely solved, and we can move to the other configuration, the box trap.

Hardwall boundary conditions

The case of DBC is barely more complex, as the hard walls enclosing the system simply induce k to $-k$ reflection for every allowed rapidity. This reflection effectively doubles the number of plane waves in each sector. It means that the superposition must now be between every wave and its reflection. Hence, the N -body wave function in the case of DBC, in the sector $0 < x_1 < \dots < x_N < L$, reads [Gaudin, 1971, Batchelor et al., 2005]

$$\Psi(x_1, \dots, x_N) = \sum_P \sum_{\epsilon_i = \pm} \epsilon_1 \dots \epsilon_N A_P(\{\epsilon_i k_i\}, c) e^{i \sum_j \epsilon_j k_{P_j} x_j}, \quad (2.19)$$

where $\varepsilon_i = \pm$, and the $N!N^2$ amplitudes (N^2 for the possible permutation of k and $-k$) $A_P(\{\varepsilon_i k_i\}, c)$ are given by

$$A_P(\{\varepsilon_i k_i\}, c) = \prod_{j < l} \left(1 + \frac{ic}{\varepsilon_j k_{P_j} - \varepsilon_l k_{P_l}} \right) \left(1 - \frac{ic}{\varepsilon_j k_{P_j} + \varepsilon_l k_{P_l}} \right), \quad (2.20)$$

and the $2N$ rapidities $\varepsilon_j k_j$ are solutions of the following usual (up) and logarithm (down) Bethe equations

$$e^{2ik_j L} = \prod_{l \neq j} \frac{k_j - k_l + ic}{k_j - k_l - ic} \frac{k_j + k_l + ic}{k_j + k_l - ic}, \quad (2.21)$$

$$k_j L = \pi I_j + \frac{1}{2} \sum_{l \neq j} (\vartheta(k_j - k_l) + \vartheta(k_j + k_l)). \quad (2.22)$$

Making no exceptions, the Bethe quantum numbers can be found considering the limit of infinite interactions. The procedure is widely similar to PBC and, therefore, will not be detailed here. In contrast with the precedent case, there is no need for the ground state energy to be zero. As a consequence, we can simply choose the set of N positive non-zero integers as Bethe quantum numbers

$$I_j = j, \quad j = 1, \dots, N. \quad (2.23)$$

We have earned a deeper understanding of our model's solutions for single species. In this section, we have thoroughly explained the general solution for bosons with arbitrary repulsive interaction strength. However, the wave function just constitutes the initial step in investigating our system. We now want to analyze correlations to extract further insights from these solutions. That said, we will first explore the real space correlations in two regimes: with strong and without interactions.

2.2 The correlation functions

In the following section will first explicitly present the correlation functions used in our analysis. We will then solve the simple SF case and showcase the analogy with Random Matrix Theory (RMT). Consecutively, we will address the more challenging problem of TB, exposing its interwoven with SF. Aside from these general considerations, we will give the special form that takes the first-order correlation function in our two preferential geometries.

2.2.1 General definition in quantum mechanics

We have presented in Chapter 1 the one-body correlation function expression in quantum mechanics [Equation (2.24)]. However, for the consistency of this section, let us recall it

$$\rho_1(x, y) = N \int_{\mathcal{D}^{N-1}} \prod_{n=2}^N dx_n \Psi(x, x_2, \dots, x_N) \Psi^*(y, x_2, \dots, x_N). \quad (2.24)$$

This function could be generalized to any higher order throughout the n -th order correlation function

$$\rho_n(X^{(n)}, Y^{(n)}) = \rho_{n,0} \int_{\mathcal{D}^{N-n}} \prod_{j=n+1}^N dx_j \Psi(X^{(n)}, x_{n+1}, \dots, x_N) \Psi^*(Y^{(n)}, x_{n+1}, \dots, x_N) \quad (2.25)$$

with $X^{(n)} = x^{(1)}, \dots, x^{(n)}$ and $\int dX^{(n)} \rho_n(X^{(n)}, X^{(n)}) = \rho_{n,0} = \frac{N!}{(N-n)!}$. Like the first-order, the diagonal part of ρ_n is defined as the n -particles spatial distribution - or equivalently the n -tuple density. This n -th order density displays the joint-probability to find a particle in $x^{(1)}$ while $n-1$ other particles are in the $x^{(i)}$'s positions, with $i = 2, \dots, n$.

With the wave functions obtained earlier, we are ready to explore physical systems. Let us begin with spinless, non-interacting fermions.

2.2.2 Spinless fermions and random matrix theory

Although SF have already been proficiently studied, they represent an excellent warm-up to familiarize with correlations of cold atoms. Despite often considered a basic problem, it is essential to note that phenomena within SF are still yet to be discovered. To explore this topic, we will draw a powerful analogy with RMT. This point of view is frequently chosen for several reasons: 1) it provides an exact solution for all orders of correlation functions ρ_n , 2) by using ρ_n as material, it provides an easy way to extrapolate problems or perform further computation, and 3) it offers an intuitive way to discuss these complex systems.

J. Wishart first introduced the RMT [Wishart, 1928] in mathematical statistics. The parallel between RMT and quantum mechanics arrived later with the early works of E. P. Wigner on nuclear physics [Wigner, 1951]. This correspondence is allowed by their similar underlying random structures. On the quantum side, energy levels are determined by the eigenvalues of a hermitian operator. Afterward, F.Dyson proposed that these eigenvalues could be approximated using random matrices respecting the symmetries of the quantum system. This reasoning appears much more fruitful than he expected, even leading to the exact solution. Consequently, he wrote several articles that paved the way for decades of mathematic and physical research on this topic [Dyson, 2004a, Dyson, 2004b, Dyson, 2004c, Dyson & Mehta, 2004, Mehta & Dyson, 2004].

In fact, the RMT analogy does not begin with the correlation function but takes its roots back to the wave function and its depiction of the probability distribution.

Probability distribution of positions as a point process

To elaborate further, let us discuss the case of particles in a ring and the circular unitary ensemble, also known as $CUE(N)$. $CUE(N)$ is the ensemble of the unitary

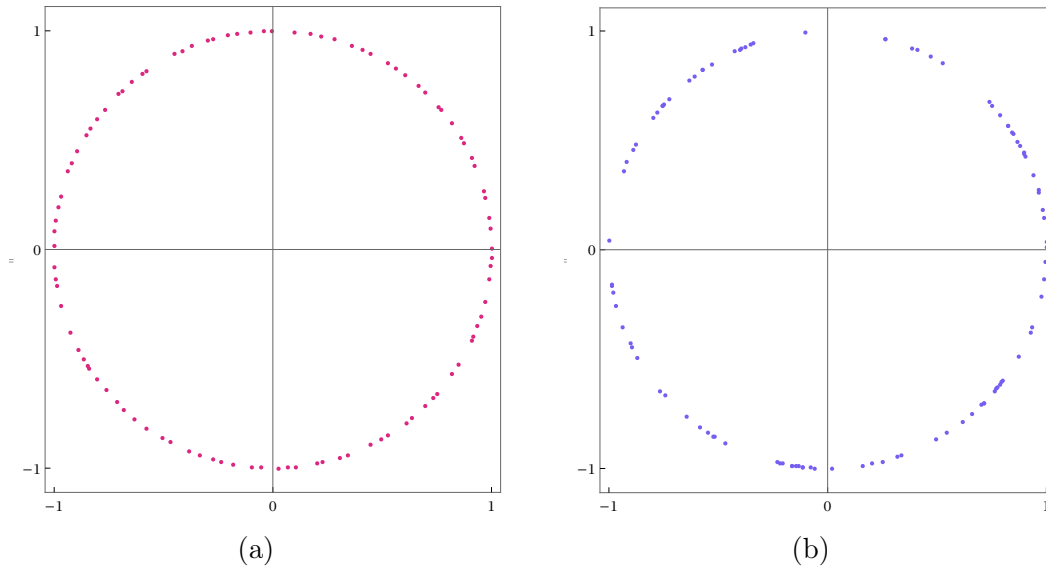


Figure 2.2: (a) Distribution of a $U(100)$ matrix eigenvalues or, equivalently, sampling of $N = 100$ fermions on the unitary circle \mathbb{S}^1 using $|\Psi|^2$ as a Profile Density Function PDF. (b) 100 uniformly distributed points on \mathbb{S}^1 .

matrices $U(N)$ - the group of $N \times N$ matrices filled with uniform random complex entries. These matrices have eigenvalues circumscribed on the unitary circle \mathbb{S}^1 and randomly distributed along it. The sampling of these eigenvalues forms a Point Process (PP), which is essentially a stochastic process. The connection with quantum mechanics is simple: the spatial probability distribution to find particles, $|\Psi|^2$, is precisely the same point process that describes the $U(N)$ eigenvalues distribution. In fact, the eigenvalues distribution of the $U(N)$ matrices and the joint probability distribution of N SF on \mathbb{S}^1 are identical, and can be expressed as

$$\frac{1}{N!(2\pi)^N} \prod_{1 \leq i < j \leq N} |e^{i\theta_j} - e^{i\theta_k}|^2, \quad (2.26)$$

with the angles $\theta \in [0, 2\pi)$. This beautiful correspondence becomes clearer when comparing a sampling of points using Equation (2.26) as a PDF [Figure 2.2(a)] to a uniformly random assembly of points on the same domain [Figure 2.2(b)]. Indeed, the sampled points seem to organize their distribution, which contrasts with the tendency for clusters displayed by the uniformly distributed points. This behavior is known as "eigenvalue repulsion" and perfectly recreates the aversion for SF to be close. Conversely, the uniformly distributed points could represent a sampling of identical non-interacting bosons as $|\Psi|^2$ is constant in this case. To conclude, it is important to note that this point process correspondence is not limited to the ring geometry and applies to various boundary conditions. For a rigorous definition or the treatment of other systems, see [Dean et al., 2019, Meckes, 2019].

This analogy appears to be a beautiful representation of our problem, but no particular outcomes have arisen apart from expressing $|\Psi|^2$ in terms of RMT. Indeed, all the potency of the RMT comes when looking at the correlation functions.

Correlation functions as a determinantal point process

The rigorous definition of a Determinantal Point Process (DPP) is quite complicated, but for our purposes, it can be viewed as a PP that takes the form of a determinant with a kernel $K(x, y)$. Kernels are extremely convenient tools as they encode the pairwise interactions between the particles and their spatial preferences. This simplification helps us to understand the system's overall behavior by characterizing the interdependence between its constituents and providing intuitive interpretation. Furthermore, it allows extrapolation to more complex models by incorporating new dependencies (such as temperature and dimensionality). To demonstrate this determinantal property of 1D processes involving SF, we will rewrite ρ_n using Ψ_{SF} , in Equation (1.7), under the Leibniz form of a determinant. Hence,

$$\Psi_{SF}(x_1, \dots, x_N) = \frac{1}{\sqrt{N!}} \sum_{P \in S_N} \varepsilon(P) \prod_{k=1}^N \phi_{P(k)}(x_k), \quad (2.27)$$

where $\varepsilon(P)$ is the signature of the permutation P . The n -th order correlation function then reads

$$\begin{aligned} \rho_n(X^{(n)}, Y^{(n)}) &= \frac{\rho_{n,0}}{N!} \sum_{P, Q \in S_N} \varepsilon(P)\varepsilon(Q) \prod_{j=1}^n \phi_{P(j)}(x^{(j)})\phi_{Q(j)}^*(y^{(j)}) \\ &\quad \times \prod_{l=n+1}^N \int_{\mathcal{D}} dz \phi_{P(l)}(z)\phi_{Q(l)}^*(z). \end{aligned} \quad (2.28)$$

Thus, using orthonormalization of natural orbitals, one can find

$$\rho_n(X^{(n)}, Y^{(n)}) = \frac{\rho_{n,0}}{N!} \sum_{P, Q \in S_N} \varepsilon(P)\varepsilon(Q) \prod_{j=1}^n \phi_{P(j)}(x^{(j)})\phi_{Q(j)}^*(y^{(j)}) \prod_{l=n+1}^N \delta_{P(l), Q(l)}. \quad (2.29)$$

The next step is to check if this expression could take a determinantal form for the different correlation orders.

1-st order correlation function:

For $n = 1$, $\rho_{1,0} = N$, and $\prod_{l=2}^N \delta_{P(l), Q(l)}$ imply that $P = Q$ (if the $N - 1$ last element are equal, the first element must too) and $\varepsilon(P)\varepsilon(Q) = \varepsilon(P)\varepsilon(P) = 1$. Hence, we only have to consider the $(N - 1)!$ identical series of ordered integers $\{j\}$ (instead of the original disordered and distinct series of $\{P(l), Q(l)\}$). It technically means that $\sum_{P, Q \in S_N} \prod_{l=2}^N \delta_{P(l), Q(l)} \rightarrow (N - 1)! \sum_{j=1}^N$. We then find the much more simple, well-known form of the first-order correlation function for SF

$$\rho_1(x, y) = \sum_{j=1}^N \phi_j(x)\phi_j^*(y). \quad (2.30)$$

Under this form, the one-body correlation function exhibits its determinantal nature. Moreover, looking through the RMT lens, one can recognize the non-trivial

eigenvalues of uniformly distributed $U(N)$ matrices. The correspondence between random matrix and other physical systems, such as DBC or harmonically trapped SF, can be found in [Forrester et al., 2003a, Dean et al., 2019, Meckes, 2019].

If we insert the waves functions for PBC and DBC into Equation (2.30), we end up with the following expressions

$$\rho_1^{Ring,Odd}(x, y) = S_N \left(\frac{2\pi(x-y)}{L} \right), \quad (2.31)$$

$$\rho_1^{Box}(x, y) = \frac{1}{2} \left(S_{2N+1} \left(\frac{\pi(x-y)}{L} \right) - S_{2N+1} \left(\frac{\pi(x+y+1)}{L} \right) \right), \quad (2.32)$$

with $S_N(x) = \sin(Nx/2)/\sin(x/2)$ the sin kernel, and $x, y \in [-L/2, L/2]$. The case of even N for PBC is more delicate and has to be treated separately.

This procedure can be applied to correlations of any order. However, no additional insight are obtained throughout these lengthy derivations. Thus, we will only present the determinantal form of the correlation function for the n -th order.

n -th order correlation function:

Following the same steps as for the first-order, one can end up with the ensuing form

$$\rho_n(X^{(n)}, Y^{(n)}) = \det[\rho_1(x^{(i)}, y^{(j)})]_{i,j=1,\dots,n}, \quad (2.33)$$

which represents a DPP with $\rho_1(x, y)$ for kernel. This result could simply be interpreted as a consequence of the self-reproducibility (i.e., $\int dz K(x, z)K(z, y) = K(x, y)$) of the kernel. This DPP finding is remarkably effective, as it only requires the first-order correlation function to describe the system completely. This result is simply the Wick theorem. It must be pointed out that the RMT analogy breaks out of this regime, like at finite temperatures or higher dimensions. Despite this limitation, the efficiency of DPP does not end up alongside and remains quite robust while considering more complex scenarios. For instance, the temperature or dimension effects could be studied by adding the corresponding dependency to the kernel. Consequently, the DPP point of view is revealed to be extremely useful in many configurations, and its robustness strongly indicates that it is a natural way of thinking about SF processes.

If the DPP formalism is clearly advantageous while dealing with SF, this range of application is not restricted to this case. Indeed, we can attribute another crucial outcome to this development - the connection it allows between SF and TB.

2.2.3 Tonks-Girardeau regime

As observed with the wave function, TB may closely resemble SF even if their statistics display notable discrepancies. This duality is enlightened with the 1-st order correlation function. This one still presents a determinantal form, now belonging to the Fredholm type [Fredholm, 1903], while remarkably keeping a fermionic kernel. Lenard owes the priority of this general form [Lenard, 1966], which reads

$$\rho_1^{TB}(x, y) = \sum_{n=0}^{N-1} \frac{(-\xi)^n}{n!} \int_x^y \cdots \int_x^y dx_{n+1} \rho_{n+1}^{SF}(x, x_2, \dots, x_{n+1}, y, x_2, \dots, x_{n+1}), \quad (2.34)$$

for $x < y$, $\xi = 2$ and with the integrand having the following explicit form

$$\rho_n^{SF}(x, \tilde{X}_n, y, \tilde{X}_n) = \det \begin{bmatrix} K(x, y) & [K(x_j, y)]_{j=2, \dots, n} \\ [K(x, x_k)]_{k=2, \dots, n} & [K(x_j, x_k)]_{j, k=2, \dots, n} \end{bmatrix}, \quad (2.35)$$

$$=: K \begin{pmatrix} x & x_2 & \cdots & x_n \\ y & x_2 & \cdots & x_n \end{pmatrix}, \quad (2.36)$$

with $K(x, y) = \rho_1^{SF}(x, y)$ the Fredholm determinant kernel and $\tilde{X}_n = x_2, \dots, x_n$. The Fredholm determinant form constitutes an elegant way to present ρ_1^{TB} . Although it can be challenging to work with practically, it has proven highly effective in studying short-distance correlations since every term in the corresponding expansion will depend on successive powers of $|x - y|$.

Thankfully, another determinantal form exists for a more general purpose and, this time, integrated. Starting from the identity

$$\begin{aligned} \int_{-1/2}^{1/2} dx_1 \cdots \int_{-1/2}^{1/2} dx_N \prod_{l=1}^N w(z_l) \prod_{1 \leq j < k \leq N} |z_j - z_k|^2 \\ = N! \det \left[\int_{-1/2}^{1/2} dx w(z) z^{k-j} \right]_{j, k=1, \dots, N}, \end{aligned} \quad (2.37)$$

with $z_n = e^{2\pi i x_n/L}$. P.J. Forrester has found a much more convenient Toeplitz determinantal formulation of the 1st-order correlation function for PBC [Forrester et al., 2003a, Forrester et al., 2003b]

$$\rho_1^C(t) = \frac{1}{L} \det[a_{j-k}^C(t)]_{j, k=1, \dots, N-1}, \quad (2.38)$$

with

$$a_n(t) = \frac{1}{\pi} \int_0^{2\pi} du |\cos(u) - \cos(t)| e^{iun} \quad (2.39)$$

$$\begin{aligned} &= 2\delta_{n,0} \cos(t) - \delta_{n,1} - \delta_{n,-1} - \frac{4 \cos[t] \sin[n|t]}{\pi n} \\ &+ \frac{2}{\pi} \left(\frac{\sin[(n+1)|t]}{n+1} + \frac{\sin[(n-1)|t]}{n-1} \right), \end{aligned} \quad (2.40)$$

and $t = 2\pi(x - y)/L$ in $[0, 2\pi)$. Likewise, a similar expression can be found for DBC [Forrester et al., 2003a]

$$\rho_1^B(x, y) = \frac{2^{3N-2}}{L} \sin\left(\frac{\pi(x+1/2)}{L}\right) \sin\left(\frac{\pi(y+1/2)}{L}\right) \det[a_{j,k}^B(x, x')]_{j,k=1,\dots,N-1}, \quad (2.41)$$

with

$$a_{j,k}^B(x, y) = \int_0^1 du \left| \cos\left(\frac{\pi x}{L}\right) - \cos(\pi u) \right| \left| \cos\left(\frac{\pi y}{L}\right) - \cos(\pi u) \right| \sin(\pi j u) \sin(\pi k u). \quad (2.42)$$

Our analysis has explored various methods for determining correlation functions for SF and TB in both PBC and DBC geometry. Additionally, we have discovered a representation that effectively highlights the connection between these two systems. Nevertheless, as previously mentioned, while correlation functions in real space serve as valuable theoretical tools, they can be complex to investigate experimentally. Again, let us shift to Fourier space to overcome this issue.

2.3 The momentum distribution

We previously discussed the purpose of momentum analysis, and we can now move on to the specifics of our systems. In the first place, we will quickly recall the textbook results obtained for the non-interactive scenario. These will serve as a baseline for future comparison and will help the ensuing interpretations of interactive bosons. In a second, we will shortly overview some quantities obtainable via $n(k)$ and related to short- and long-distance correlations. We want to emphasize that the idea is not to give an exhaustive inventory of the current state of the art but rather to depict the typical outcomes. The critical points will be detailed along with the results of this thesis. In particular, in Chapter 4 for the short-distance behavior, and in Chapter 5 for both short and long-distance analysis.

Let us begin with the straightforward ring geometry, where the momentum distribution n_k is discrete due to PBC. The continuous case will just be briefly evoked after as it simply generalizes the discrete case. For bosons, the momentum distribution n_k is proportional to a Kronecker's delta, which tells that every particle is in the same, here lowest, energy state. For SF and odd N , n_k is roughly a centered step function. It portrays a perfectly filled and centered Fermi sphere for odd N , while for even N , a fermion with momentum $\pm\pi N/L$ remains outside the sphere. The continuous case is very similar, with the bosonic distribution becoming Dirac's delta function and the fermionic distribution being a centered step function. These typical forms are shown in Figure 2.3(a) for finite temperatures. In the latter, the broadening is due to thermal energy, which allows for the population of higher energy states.

In the first approximation, the effect of contact interactions can be predicted by analogy with the thermal case. As interactions increase, higher momentum states will slowly become populated, ultimately resulting in the TB spectrum. To be

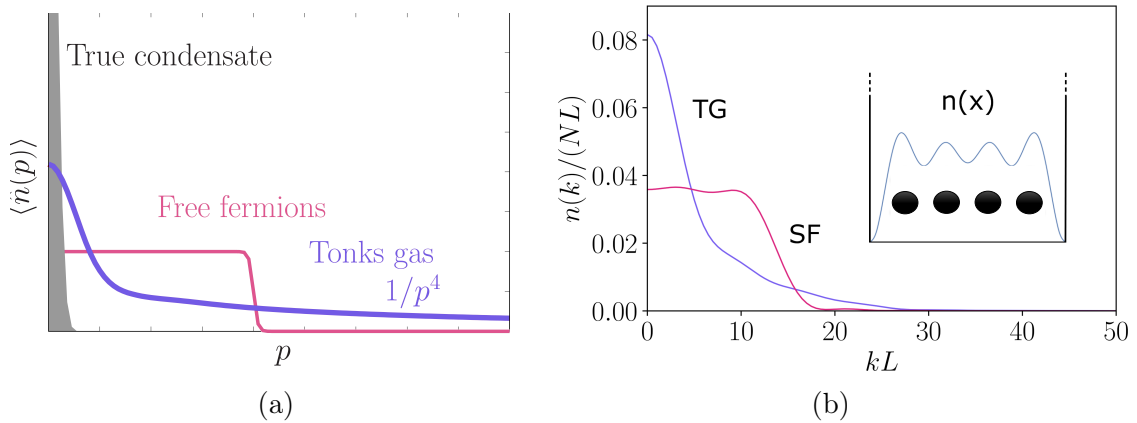


Figure 2.3: (a) Illustration of the momentum distribution at very low temperature in the free space. (Grey-filled curve) 3D gas of non-interactive bosons, (black curve) gas of SF, and (red curve) gas of TB. The special $1/p^4$ decay featured by the momentum distribution of TB has been highlighted. (b) The rescaled momentum distribution of four SF (magenta) and four TB bosons (violet) trapped in a 1D box of length L . The inset illustrates the setup corresponding to the plot and the common density shared by SF and TB.

precise, in this case, it is not directly mediated by the interaction but by the quantum fluctuation generated by the interaction. This distribution is pictured in Figure 2.3(a) and plotted for four particles in a 1D box in Figure 2.3(b). However, the effects of interactions are more subtle, altering also how $n(k)$ decays at large k . This important consequence of interactions will be detailed during the presentation of the short-distance correlations. As a side remark, some overall oscillations can be observed in the distribution of TB and SF for DBC. These are the momentum analogs of Friedel's oscillations caused by the hard walls and originally induced in the density.

In the introductory Chapter 1, we have evoked the critical pieces of information carried by the low and high momentum distribution. Indeed, the global and short-distance behavior of the system is imbued in these regions. These are naturally strongly affected by the particles involved or the regime of interactions, as highlighted in Figure 2.3(a) and Figure 2.3(b). In the last part of this chapter, we will detail these crucial features in our investigation of correlations in the first scenario for TB and in the second for both SF and TB.

2.3.1 Long-distance coherence

To begin our discussion on TB's long-distance behavior, let us introduce the key quantity chosen for assessing this problem - the zeroth momentum distribution. This object takes the following form

$$n(0) = n_0 = \frac{1}{2\pi} \int_{\mathcal{D}^2} dx dy \rho_1(x, y), \quad (2.43)$$

The choice of n_0 for investigating long-distance coherence is first motivated by its

accessibility but also by its connection with the long-distance coherence of matter waves. For instance, in the homogeneous case, it can be linked to the historical quantity used to depict a BEC-like behavior - the population of the lowest energy level λ_0 . In general, the population of a j -th energy level λ_j is determined by solving the eigenvalue equation derived from the first-order correlation function

$$\int_{\mathcal{D}} \rho_1(x, y) \phi_j(y) dy = \lambda_j \phi_j(x). \quad (2.44)$$

In general, solving this set of equations can be challenging, but some configuration widely simplifies the task. Indeed for PBC, n_0 and λ_0 are strictly equal. This indicates that the same qualitative information can be obtained via n_0 , which is considerably easier to obtain than λ_0 . Although not general, these two quantities share a similar scaling with the number of particles in some configurations. For instance, this shared scaling is valid for homogenous trapping. However, one must be careful while relying on the analogy between λ_0 and n_0 as it breaks with a harmonic trap [Forrester et al., 2003b, Papenbrock, 2003, Devillard et al., 2020], for example. In general, we can make this distinction: n_0 probe the long-distance coherence of the gas, λ_0 the existence of a condensate.

With these notions established, we can now explore the behavior of TB. It is known that the standard state of an UCAG of bosons at low temperatures is a BEC. However, strictly speaking, condensation cannot occur in dimensions lower than three, as λ_0 no longer scales with N . Typically, it will scale with \sqrt{N} for 1D UCAG with contact interactions. The inability to achieve true condensation at low dimensions is attributed to quantum fluctuations. These fluctuations are particularly strong in these regimes and significantly reduce the overall coherence of the system, thereby hindering the system from condensing. This result can be obtained by deriving the occupation number with the density of states as entry. Alternatively, we can keep our correlation point of view and find this outcome using n_0 and ρ_1 . In the ring, the asymptotic expansion of ρ_1 at large distance t is $\rho_1^R(t) \sim \rho_\infty \sqrt{N} |\sin(t)|^{-1/2}$, with $\rho_\infty \approx 0.92418$ [Lenard, 1964, Widom, 1973]. This result is the equivalent of the ρ_1 's form in the thermodynamic limit found by H. G. Vaidya and C. A. Tracy [Vaidya & Tracy, 1979]. By inserting this result in Equation (2.43), we obtain the main contribution to the zeroth momentum distribution of a TB gas with PBC, i.e., $n_0^{TB} \approx 1.5427\sqrt{N}$, which was initially found by P.J. Forrester [Forrester et al., 2003b]. To be precise, P.J. Forrester found that we can accurately describe the n_j 's in the ring with the ensuing fit

$$n_j \approx a_j \sqrt{N} + b_j + c_j / \sqrt{N}. \quad (2.45)$$

As an example, in the case of PBC, (a_0, b_0, c_0) was found to be $(1.542, -0.573, 0.004)$ [Forrester et al., 2003b], which matches the earlier expansion result. This property also applies to the zeroth momentum distribution of bosons in a box, with (a_0, b_0, c_0) being $(1.253, -0.466, 0.013)$ and, remarkably, with spin mixtures [Aupetit-Diallo et al., 2022] as discussed in Chapter 5.

2.3.2 Short-distance correlations

On the opposite side of the distribution also lies crucial information: the Tan's contact \mathcal{C}_N [Tan, 2008a, Tan, 2008b, Tan, 2008c]. This quantity encodes numerous details about the system. For instance, how particles will brush themselves and how particles will exchange with each other. This means insights about the system's symmetry could also be extracted using the Tan's contact [Decamp et al., 2017]. Moreover, contact interactions also lead to the universality of many equilibrium and thermodynamic quantities, most of them being summarized by the Tan's relations [Tan, 2008a, Tan, 2008b, Tan, 2008c, Barth & Zwerger, 2011, Păţu & Klümper, 2017]. In one of them, the interplay between contact interactions and exchange symmetry between N particles leads to the appearance of a universal algebraic decay of the tail of the momentum distribution of the form

$$n(k) \underset{k \rightarrow \infty}{\simeq} \frac{\mathcal{K}_N}{k^4}, \quad (2.46)$$

where the power-law decay derives from the type of singularity of ρ_1 or Ψ , and its weight \mathcal{K}_N depends on the slope in the vicinity of these singularities and on their number. This power law effectively arises for momentum $\hbar k$ larger than any other typical momentum scale, such as the Fermi momentum k_F . \mathcal{K}_N is usually identified with \mathcal{C}_N , which is proportional to $\partial E / \partial g^{-1}$, namely to gE_{int} , the product between the interaction strength and the total interaction energy of the system [Lenard, 1964, Minguzzi et al., 2002, Olshanii & Dunjko, 2003]. The equivalence $\mathcal{K}_N = \mathcal{C}_N$ holds at equilibrium both for homogeneous systems with periodic boundary conditions and smoothly trapped systems, for any mixture of interacting particles, and any dimension [Tan, 2008a, Tan, 2008b, Tan, 2008c, Barth & Zwerger, 2011]. The possible scenarios breaking this relation have been discussed in [Bouchoule & Dubail, 2021, Cayla et al., 2023, Aupetit-Diallo et al., 2023] and will be the object of the Chapter 4.

The origin of the $1/k^4$ decay is the universal way the many-body wave function has to accommodate the contact interaction when two particles approach each other. For instance, anti-symmetric exchanges cancel the effects of contact interactions and do not contribute to \mathcal{K}_N , while symmetric exchanges induce in the many-body wave function, and thus in the first-order correlation function, a discontinuity of the derivative, a cusp, that contributes to the $\sim 1/k^4$ behavior of the momentum distribution tail [Minguzzi et al., 2002, Olshanii & Dunjko, 2003, Vignolo & Minguzzi, 2013]. This critical feature is illustrated in Figure 2.4, where the two extremal cases, in terms of symmetry, of SF and TB have been plotted. \mathcal{K}_N is therefore sensitive to the exchange symmetry and can be used as observable for symmetry spectroscopy in quantum mixtures [Decamp et al., 2016b, Decamp et al., 2017]. This interplay between interactions and symmetry is at the origin of the cusp presented in Figure 2.1 and has repercussions on the spectrum of the finite interaction system [Volosniev et al., 2014, Decamp et al., 2016b].

Mathematically the $1/k^4$ tail can be understood using Watson's lemma [Bleistein & Handelsman, 1986, Olshanii & Dunjko, 2003], namely the asymptotics of the Fourier transform of functions having a singularity of the type $f(z) = F(z)|z - z_0|^\alpha$, with $F(z)$ analytic, and $\alpha > -1$ and $\alpha \neq 0, 2, 4, \dots$ reads

$$\int_{\mathcal{D}} dz e^{-ikz} F(z) |z - z_0|^\alpha \underset{k \rightarrow \infty}{=} \mathcal{F}_\alpha \frac{e^{-ikz_0} F(z_0)}{|k|^{\alpha+1}} + \mathcal{O}\left(\frac{1}{|k|^{\alpha+2}}\right), \quad (2.47)$$

with $\mathcal{F}_\alpha = 2 \cos[\pi(\alpha+1)/2] \Gamma(\alpha+1)$ and $\Gamma(\alpha)$ is the Gamma function. Therefore, by looking at Equations (1.13) and (2.24), the possible contributions to the $1/k^4$ tail of $n(k)$ could be seen as non-analytic terms of the form: 1) $|x-y|^3$ in $\rho_1(x, y)$ [Forrester et al., 2003b, Vignolo & Minguzzi, 2013], 2) $|x - \bar{x}|$, with $\bar{x} \in \mathcal{D}$, in $\Psi(x, x_2, \dots)$ [Minguzzi et al., 2002, Olshanii & Dunjko, 2003].

The TB gas provides a pedagogical example of this behavior for a smooth trapping potential. Its 1-st order correlation function behaves as $|x-y|^3$ around $x \sim y$ and, consequently, $n(k)$ displays an algebraic tail [Forrester et al., 2003b]. This differs from the case of free fermions and bosons in the same trap configuration, whose ρ_1 are instead analytical in \mathcal{D} , and their momentum distributions do not have any algebraic tail. This can be shown by expanding the Lenard form of ρ_1 [Equation (2.34)]. For a smooth trapping potential, the only term that contributes to the $1/k^4$ algebraic decay of $n(k)$ is the first term of the expansion in Equation (2.34), namely $-2 \int_x^y dx_2 \rho_2^{\text{SF}}(x, x_2; y, x_2)$ [Olshanii & Dunjko, 2003]. Indeed, by using Equation (4.18) and introducing the change of coordinates $x_r = y - x$ and $x_{cm} = (x + y)/2$, one has [Fang et al., 2009, Vignolo & Minguzzi, 2013]

$$n^{\text{TB}}(k) \underset{k \rightarrow \infty}{\simeq} \frac{1}{2} \int_{2\mathcal{D}} dx_r e^{-ikx_r} \frac{|x_r|^3}{6} \mathcal{C}_N^{\text{TB}}, \quad (2.48)$$

where $1/k^4$ is given by applying Equation (2.47) to the integral in x_r and [Sant'Ana et al., 2019]

$$\mathcal{C}_N^{\text{TB}} \equiv \frac{2}{\pi} \int_{\mathcal{D}} dx_{cm} \lim_{\varepsilon \rightarrow 0} \frac{\rho_2^{\text{SF}}(x_{cm} - \varepsilon, x_{cm}; x_{cm} + \varepsilon, x_{cm})}{\varepsilon^2} \quad (2.49)$$

is the Tan's contact which is equivalent to \mathcal{K}_N in this case. Equation (2.49) enlightens the role of two-body correlations in $\mathcal{C}_N^{\text{TB}}$.

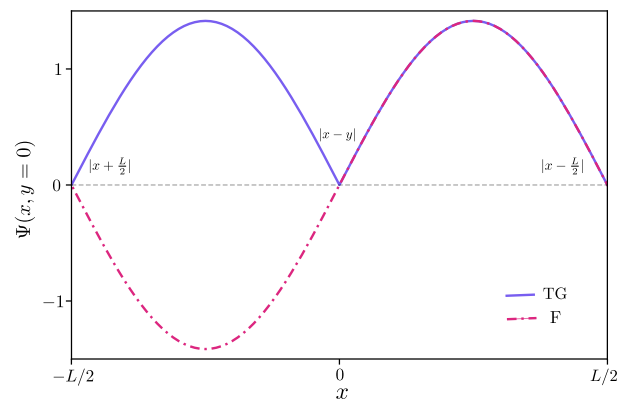


Figure 2.4: Two particles wave function $\Psi(x, y)$ with $y = 0$ for SF (solid line) and TB (dash-dotted line) trapped in a box of size L . We distinguish three different points of non-analyticity, at $|x \pm L/2|$ (for SF and TB) and $|x - y|$ (only for TB).

Chapter 3

Spin mixtures in highly repulsive regime

This chapter will present different methods for investigating 1D spin mixtures' properties at strong interaction. First, we will consider the Bethe ansatz solution of the corresponding Hamiltonian. Although exact, this method is demanding to manipulate efficiently. To circumvent this difficulty, we will detail more convenient ways, suitable for trapped systems, to obtain the wave function in the highly repulsive regime. Afterward, we will explore the remarkable symmetry exhibited by this system using the newly obtained solutions. This investigation will demonstrate the information accessible with the symmetry analysis and how it can be acquired.

We consider spin mixtures of equal-mass ultracold atoms with contact interaction between atoms. In a homogenous configuration and at arbitrary intra- and inter-species interaction strength $g_{\sigma,\sigma}$ and $g_{\sigma,\sigma'}$. The related Hamiltonian reads

$$\hat{H} = \sum_{\sigma',\sigma}^{\kappa} \sum_{i=1}^{N_{\sigma}} \left[-\frac{\hbar^2}{2m} \frac{\partial^2}{\partial x_{i,\sigma}^2} + g_{\sigma,\sigma'} \sum_{j>i}^{N_{\sigma'}} \delta(x_{i,\sigma} - x_{j,\sigma'}) \right], \quad (3.1)$$

where the σ 's stand for spin indices and goes from 1 to κ the total number of spin species. From now on, we will drop the spin indices from variables seeking conciseness. During this chapter, we will place a special focus on the same interaction strength scenario ($g_{\sigma,\sigma} = g_{\sigma,\sigma'} = g > 0$). In this case, the model is integrable at any interaction strength and any type of spin mixture [Sutherland, 1968, Oelkers et al., 2006, Li et al., 2003, Imambekov & Demler, 2006b]. The natural way to obtain the corresponding general solution is, as for single species, through the Bethe ansatz method. In the ensuing part, we will briefly introduce the result of this method at arbitrary g and, in our case of interest, the strongly repulsive regime.

3.1 The Bethe wave function

3.1.1 Arbitrary interaction strength

We present the general Bethe ansatz solution of Equation (3.1) for two-component hardcore bosons or fermions with PBC mixtures. The derivation for larger κ at any

g generalizes the following. For the interested reader, a comprehensive Bethe ansatz overview of spin mixture for PBC and DBC can be found in [Oelkers et al., 2006].

For $\kappa = 2$ bosonic or fermionic mixture with PBC, the Bethe ansatz solution of Equation (3.1) in the sector $x_1 < \dots < x_N$ reads [Li et al., 2003, Oelkers et al., 2006, Imambekov & Demler, 2006b]

$$\Psi(x_1, \dots, x_N) = \sum_{P \in S_N} A_P(\{k_i\}, \{\Lambda_m\}, c) e^{i \sum_j k_{P(j)} x_j}, \quad (3.2)$$

where $N = N_\downarrow + N_\uparrow$ is the total number of particles of spin denoted \downarrow and \uparrow , and $c = 2mg/\hbar$, and P is a permutation of the symmetric group S_N . The amplitudes $A_P(\{k_i\}, \{\Lambda_m\}, c)$ depend on the N charge rapidities $\{k_i\}$ but now also on the N_\downarrow spin rapidities $\{\Lambda_m\}$. It must be pointed out that this notation supposes $N_\downarrow \leq N_\uparrow$ without any loss of generality. The $\{k_i\}$'s are the same as the single species case and will define the state manifold, whereas the $\{\Lambda_m\}$'s correspond to a spin excitation state inside this manifold. The Bethe equations fixing the rapidities for both fermions and bosons at arbitrary c are the ensuing [Oelkers et al., 2006]

$$\left\{ \begin{array}{l} Lk_j = 2\pi I_j + 2\eta_B \sum_{l=1}^N \arctan\left(\frac{k_l - k_j}{c}\right) + 2(1 - 2\eta_B) \sum_{m=1}^{N_\downarrow} \arctan\left(\frac{2(k_j - \Lambda_m)}{c}\right) \\ \sum_{j=1}^N \arctan\left(\frac{2(\Lambda_m - k_j)}{c}\right) = \pi J_m + \sum_{n=1}^{N_\downarrow} \arctan\left(\frac{2(\Lambda_m - \Lambda_n)}{c}\right) \end{array} \right. , \quad (3.3)$$

where we introduced the charge and spin Bethe quantum numbers I_j and J_m , while $\eta_B = 1$ for bosons and 0 for fermions. The I_j 's and J_m 's are integers or half integers depending on the partition of the mixture, and their selection rules are summarized in Table 3.1. The energy of the system is given by $E = \frac{\hbar^2}{2m} \sum_j k_j^2$, and the total momentum is $P = \sum_j \hbar k_j$. The choice of the quantum numbers defines the state of the system. In particular, in the ground state, adjacent quantum numbers are spaced by one unit. Moreover, similarly to identical particles, they are chosen such that the corresponding rapidities k_j minimize the energy E [Li et al., 2003, Imambekov & Demler, 2006a, Imambekov & Demler, 2006b].

Table 3.1: Selection rule for the Bethe quantum numbers of a $SU(2)$ fermionic and bosonic mixture with PBC [Yu & Fowler, 1992, Li et al., 2003]. For fermions N_\downarrow (resp. N_\uparrow) dictates the distribution of the I_j (resp. J_m) while for bosons, only N_\downarrow has to be considered.

	Fermions		Bosons	
Conditions	N_\downarrow even	N_\downarrow odd	N_\uparrow even	N_\uparrow odd
Selection rules	$I_j \in \mathbb{Z}$	$I_j \in \mathbb{Z} + 1/2$	$I_j \in \mathbb{Z} + 1/2$	$I_j \in \mathbb{Z}$
Conditions	N_\uparrow even	N_\uparrow odd	N_\uparrow even	N_\uparrow odd
Selection rules	$J_m \in \mathbb{Z} + 1/2$	$J_m \in \mathbb{Z}$	$J_m \in \mathbb{Z} + 1/2$	$J_m \in \mathbb{Z}$

3.1.2 Highly repulsive regime

We can now move toward the strong repulsion regime by looking at the limit $1/c \rightarrow 0$ of Equation (3.3) and using the symmetry of the arctangent function. While only keeping the 0-th order terms in $1/c$, we end up with

$$\begin{cases} Lk_j = 2\pi \left(I_j - \frac{1}{N} \sum_{m=1}^{N_\downarrow} J_m \right) \\ N \arctan(\lambda_m) = \pi J_m + \sum_{n=1}^{N_\downarrow} \arctan(\lambda_m - \lambda_n) \end{cases}, \quad (3.4)$$

where we have set the rescaled spin rapidities $\lambda_m = 2\Lambda_m/c$ [Ogata & Shiba, 1990, Essler et al., 2005, Oelkers et al., 2006] and suppose them non-zero. The first equation fixes the system's energy. In this interaction regime, the distribution of the quantum numbers J_m , thus the spin excitations, affects the total momentum and the kinetic energy. The second equation coincides with the Bethe equations for an isotropic spin chain [Bethe, 1931, Essler et al., 2005, Franchini et al., 2017] and does not depend on the charge degree of freedom. The same spin-charge decoupling occurs in the wave function Equation (3.2), where the amplitudes satisfy $\lim_{c \rightarrow \infty} A_P(\{k_i\}, \{\Lambda_m\}, c) = \tilde{A}_P(\{\lambda_m\}) = \epsilon(P) A_P(\{\lambda_m\})$ for fermions and $\lim_{c \rightarrow \infty} A_P(\{k_i\}, \{\Lambda_m\}, c) = A_P(\{\lambda_m\})$ for bosons. The presence or absence of the signature $\epsilon(P)$ only reveals the type of symmetry under the involved particle exchange. Moreover, the set of amplitudes $\{A_P(\{\lambda_m\})\}$ doesn't belong anymore to a particular configuration sector but effectively describes the whole space. Precisely, the wave function in a particular sector $x_{P(1)} < \dots < x_{P(N)}$ become in this limit

$$\Psi(x_1, \dots, x_N) = \tilde{A}_P(\{\lambda_m\}) e^{i \sum_j k_{P(j)} x_j}, \quad (3.5)$$

where now every $A_P(\{\lambda_m\})$ is attached to a given sector, and explicitly reads [Essler et al., 2005, Oelkers et al., 2006]

$$A_P(\{\lambda_m\}) \propto \sum_{Q \in S_{N_\downarrow}} \prod_{1 \leq m < n \leq N_\downarrow} \frac{\lambda_{Q(m)} - \lambda_{Q(n)} - 2i}{\lambda_{Q(m)} - \lambda_{Q(n)}} \prod_{l=1}^{N_\downarrow} \left(\frac{\lambda_{Q(l)} - i}{\lambda_{Q(l)} + i} \right)^{y_{P(l)}}, \quad (3.6)$$

where the integer $y_{P(l)}$ labels the position of the l -th spin down in the coordinate sector P . One can obtain these labels by placing back the spin indices on each variable. For instance, for a $2+2$ mixture, in the sector $x_{1,\uparrow} < x_{2,\uparrow} < x_{3,\downarrow} < x_{4,\downarrow}$ the $y_{P(l)}$'s are 3, and 4 while, in the sector $x_{3,\downarrow} < x_{1,\uparrow} < x_{4,\downarrow} < x_{2,\uparrow}$ the $y_{P(l)}$'s are 1, and 3.

Considering Equation (3.6), it becomes apparent that not every $N!$ amplitude is independent. As the only difference between sectors is the labels $y_{P(l)}$ if we take the example of the two sectors $x_{1,\uparrow} < x_{2,\uparrow} < x_{3,\downarrow} < x_{4,\downarrow}$ and $x_{2,\uparrow} < x_{1,\uparrow} < x_{3,\downarrow} < x_{4,\downarrow}$, because their corresponding $y_{P(l)}$ are equals they must lead to the same $A_P(\{\lambda_m\})$'s. Consequently, moving from one sector to another by swapping identical particles will not affect the $A_P(\{\lambda_m\})$'s. It results for $\kappa = 2$ mixtures that only $D = N!/(N_\downarrow!N_\uparrow!)$ amplitudes remain independent. This feature is only a consequence of the symmetry under exchanges of identical particle systems inherent to quantum mechanics. As an

amplitude is adjoined to each sector, a crucial consequence is that only a fraction of sectors are mandatory to describe the whole wave function. This huge simplification will constitute one of the lever arms of the following methods, allowing an alternative and much simpler obtaining of the solutions at large repulsion.

3.2 Spin mixtures in the high repulsion regime

To construct the wave function at large interaction, we can adopt a slightly different point of view than the Bethe ansatz. For this, we place ourselves in the scenario of strong, repulsive, and equal interaction strength. The corresponding Hamiltonian will be Equation (3.1) where $g_{\sigma\sigma} = g_{\sigma\sigma'} = g$ and g goes to infinity.

In this model, because of infinite repulsive interaction, the wave function again vanishes in the contact regions $x_i = x_j$. This mimics the Pauli's principle, meaning we can map the total wave function on a Slater's determinant. This could be synthesized under the form of an ansatz [Volosniev et al., 2014]

$$\Psi(x_1, \dots, x_N) = \sum_{P \in S_N} a_P \theta_P(x_1 < \dots < x_N) \Psi_{SF}(x_1, \dots, x_N), \quad (3.7)$$

with $\theta_P(x_1 < \dots < x_N)$ the generalized Heaviside function which is equal to 1 if $x_{P(1)} < \dots < x_{P(N)}$ and 0 elsewhere. This form can be found straightforwardly starting from Equation (3.5) as the spin-charge decoupling holds for every κ .

Analogously to the precedent case, utilizing the statistic of identical particles, we can restrict the sum over the P sectors in Equation (3.7) to $D = N! / \prod_{\sigma} N_{\sigma}!$ independent elements instead of $N!$. This set of particular sectors represents all the possible spin configurations and are usually called *snippets* [Fang et al., 2009, Volosniev et al., 2014]. They constitute the proper basis for describing a multicomponent spin mixture and will be used throughout this document.

This approach is extremely convenient to work with. To completely solve the system, we only need the natural orbitals corresponding to the trapping geometry and determine the a_P 's - the coefficient of the various snippets. In most configurations, the boundary conditions are reasonable, and we already know the orbitals and then Ψ_{SF} . Therefore, the problem boils down to finding the sets of $\{a_P\}$. Specifically, we now require a method to link each $\{a_P\}$'s set to a state, find their energies and understand the ordering of the given spectrum.

To reach this objective, two approaches will be preferred. Firstly, we will perform an expansion on the energy around $1/g = 0$. By maximizing the first-order coefficient, we will construct a matrix in which eigenvalues and vectors give the energy and $\{a_P\}$'s of every state. This development must be credited to A. G. Volosniev and collaborators [Volosniev et al., 2014]. In consequence, we have chosen to name after Volosniev the matrix, as well as the formalism behind it. Secondly, we will introduce an analogy with spin chains. The same matrix can be obtained by conveniently mapping the Hamiltonian Equation (3.1) at large repulsion on an XXZ spin chain. These two methods provide different insights about the system and will be presented separately.

3.2.1 The Volosniev formalism

When dealing with identical particles, we have directly considered the limit of infinite repulsive interaction. For spin mixtures, the treatment of strong interaction is more subtle. If we push g to infinity, we prevent the N particles from swapping with each other or precisely exchanging spin. Thus, we have frozen the spin dynamics. In this case, the ground state becomes highly degenerated with an energy E_F - the ground state energy of N spinless fermions. To recover the spin features, a more accurate technique has been developed [Volosniev et al., 2014]. The idea is to perform a first-order expansion of the energy around $1/g = 0$

$$E(1/g) \xrightarrow{1/g \rightarrow 0} E_{1/g \rightarrow 0} - \frac{1}{g}K + o(1/g^2), \quad (3.8)$$

where $E_{1/g \rightarrow 0} = E_F$ and K - the slope in energy - reads [Volosniev et al., 2014]

$$K = - \lim_{1/g \rightarrow 0} \frac{\partial E}{\partial g^{-1}} = \lim_{g \rightarrow \infty} g^2 \frac{\partial E}{\partial g}. \quad (3.9)$$

Under this limit, the probability of finding particles at the same place remains 0, so the hardcore nature of the particles is maintained, but now particle swapping is permitted. Considering the limit Equation (3.8), we can create a criterion for ordering states in the manifold and achieve the first objectives. To minimize the energy, a state should exhibit the highest energy slope. For the next step, let us investigate further this quantity and find an explicit expression.

The energy slope

For this, one can go through the Feynman-Hellman theorem

$$\frac{dE_\lambda}{d\lambda} = \langle \phi_\lambda | \frac{dH_\lambda}{d\lambda} | \phi_\lambda \rangle. \quad (3.10)$$

This theorem connects the derivative of a specific portion of energy, denoted as E_λ , which depends on a parameter λ , to the mean value of the Hamiltonian derivative with respect to this parameter. In our case, we choose $\lambda = g^{-1}$ as the parameter. It results in the parts of Equation (3.1) (with equal g 's) that depends on λ to be in the interaction potentials $V_{int} = g \sum_{i < j} \delta(x_i - x_j)$. Therefore, the derivative of the Feynman-Hellmann theorem right-hand-side gives

$$\begin{aligned} \frac{dH_\lambda}{d\lambda} &= - \frac{\partial V_{int}}{\partial g^{-1}} = -g^2 \frac{\partial V_{int}}{\partial g} \\ &= -g^2 \frac{\partial g \sum_{1 \leq i < j \leq N} \delta(x_i - x_j)}{\partial g} \\ &= -g^2 \sum_{1 \leq i < j \leq N} \delta(x_i - x_j). \end{aligned} \quad (3.11)$$

Taking the mean value of Equation (3.11) it follows

$$\langle \Psi | \frac{dV_{int}}{d\lambda} | \Psi \rangle = -g^2 \sum_{1 \leq i < j \leq N} \int_{\mathcal{D}_N} dx_1 \dots dx_N \delta(x_i - x_j) |\Psi|^2. \quad (3.12)$$

If we recall that K can be expressed as an energy derivative, one can find the limit of the Feynman-Hellmann theorem left-hand-side

$$\lim_{1/g \rightarrow 0} \frac{dE_\lambda}{d\lambda} = \lim_{1/g \rightarrow 0} \frac{\partial E}{\partial g^{-1}} = -K. \quad (3.13)$$

Equating the two sides of Equation (3.10), we end up with

$$K = \lim_{g \rightarrow \infty} g^2 \sum_{1 \leq i < j \leq N} \int_{\mathcal{D}_N} dx_1 \dots dx_N \delta(x_i - x_j) |\Psi|^2. \quad (3.14)$$

To get rid of the interaction strength dependence, we can use the many-body version of the cusp condition introduced for two particles in Equation (2.5)

$$\left[\frac{\partial \Psi}{\partial x_i} - \frac{\partial \Psi}{\partial x_j} \right]_{x_i - x_j = 0^-}^{x_i - x_j = 0^+} = \frac{2mg}{\hbar^2} \Psi(x_i = x_j). \quad (3.15)$$

Inserting the precedent cusp condition in Equation (3.14), one can obtain the energy slope

$$K = \frac{\hbar^2}{4m} \sum_{1 \leq i < j \leq N} \int_{\mathcal{D}_N} dx_1 \dots dx_N \delta(x_i - x_j) \left| \left[\frac{\partial}{\partial x_i} - \frac{\partial}{\partial x_j} \right]_{x_i - x_j = 0^-}^{x_i - x_j = 0^+} \Psi \right|^2, \quad (3.16)$$

where the derivatives must be taken before applying Dirac's delta. This sum of integrals could be widely simplified by taking out θ_P from the wave function and summing over the $N!$ possible sectors

$$K = \frac{\hbar^2}{4m} \sum_{1 \leq i < j \leq N} \sum_P \int_{\Gamma_P} dx_1 \dots dx_N \delta(x_i - x_j) \left| \left[\frac{\partial}{\partial x_i} - \frac{\partial}{\partial x_j} \right]_{x_i - x_j = 0^-}^{x_i - x_j = 0^+} \Psi \right|^2, \quad (3.17)$$

where Γ_P is the region circumscribed by the generalized Heaviside function θ_P . Under this form, we can isolate the spin and spatial contribution of the energy slope. Such integral is non-zero only in the close vicinity of the separatrix between two sectors, denoted P and Q to refer to the permutations generating them. On the 0^+ (resp. 0^-) side of the separatrix $x_i - x_j = 0$, the limit of the derivative will give a_P (resp. a_Q) times $\frac{\partial \Psi_{SF}}{\partial x_k}$ where k depend on the couple P and Q . As a result, for each neighboring sector, the energy contribution is $(a_P - a_Q)^2$ times an integral of $|\frac{\partial \Psi_{SF}}{\partial x_k}|^2$. Thus, the energy slope can be expressed in a concise way [Volosniev et al., 2014]

$$K(a_P) = \frac{\hbar^4}{m^2} \sum_{P,Q} (a_P - a_Q)^2 \alpha_{P,Q}, \quad (3.18)$$

where the sum runs over all the permutations P and Q of the type

$$P = \begin{pmatrix} 1 & \cdots & k & k+1 & \cdots & N \\ P(1) & \cdots & P(k) & P(k+1) & \cdots & P(N) \end{pmatrix}, \quad (3.19)$$

which correspond to the sectors $x_{P(1)} < \cdots < x_{P(k)} < x_{P(k+1)} < \cdots < x_N$, and

$$Q = \begin{pmatrix} 1 & \cdots & k & k+1 & \cdots & N \\ P(1) & \cdots & P(k+1) & P(k) & \cdots & P(N) \end{pmatrix}, \quad (3.20)$$

which correspond to $x_{P(1)} < \cdots < x_{P(k+1)} < x_{P(k)} < \cdots < x_N$. On the other hand, α_k refers to the nearest-neighbor exchange constant. This constant is defined as the energy cost for exchanging nearest-neighbor particles and reads as [Volosniev et al., 2014, Deuretzbacher et al., 2014, Deuretzbacher et al., 2016]

$$\alpha_{P,Q} = \alpha_k = N! \int_{x_1 < \cdots < x_N} dx_1 \dots dx_N \delta(x_k - x_{k+1}) \left| \frac{\partial \Psi_{SF}}{\partial x_k} \right|^2. \quad (3.21)$$

where we have eliminated the dependence over the neighboring sectors as α_k depends only on the trapping geometry throughout Ψ_{SF} . Consequently, integrals over Γ_P must be equal for every P , which means that α_k does not rely on the spin configuration. We have chosen $P = \text{Id}$, the identity permutation, to define the arbitrary sector. Hence, rather than having a variation of α for every configuration, we have to consider $(N - 1)$ (or N for PBC) - one for each adjacent "slot" inside the trap. Furthermore, as we consider the unique integration domain Γ_{Id} , the sum over P reduces to an $N!$ prefactor. These simplifications are responsible for the factorization in Equation (3.18) and are a direct consequence of the spin-charge decoupling at large interaction.

The energy slope, expressed as (3.18), does not discriminate the contributions of particles within or between different species. While this equation is complete for fermions, it is important to stress out the influence of identical particles when dealing with bosons. To recover the different contribution, the spin indices must be reintroduced on the variables in the Hamiltonian Equation (3.1) and the ansatz Equation (3.7). By returning back to the Feynmann-Hellmann theorem, one can find the inter- and intra-species energy slopes $K_{\sigma,\sigma}$, and $K_{\sigma,\sigma'}$. This derivation can be found in [Volosniev et al., 2015] and leads to the following separation

$$K(a_P) = \frac{\hbar^4}{m^2} \left(\sum_{P,Q} (a_P - a_Q)^2 \alpha_k + 2 \sum_{P'} a_{P'}^2 \alpha_{k'} \right), \quad (3.22)$$

if P and Q (resp. P and P') are equal up to a transposition of two consecutive distinguishable particles (resp. indistinguishable bosons). Formally the first couple P and Q refers to the snippets of the type $\{\cdots < x_{\sigma,P(k)} < x_{\sigma',P(k+1)} < \dots\}$ and

$\{\dots < x_{\sigma',P(k+1)} < x_{\sigma,P(k)} < \dots\}$ while the couple P and P' refers to the snippets of the type $\{\dots < x_{\sigma,P(k)} < x_{\sigma,P(k+1)} < \dots\}$, and $\{\dots < x_{\sigma,P(k')} < x_{\sigma,P(k'+1)} < \dots\}$. It is worth noting that the bosonic contribution has been halved because the sum over the snippets P' is effectively counting twice the corresponding number of adjacent sectors.

This outcome is general and holds from any trapping configuration. However, we have still not benefited from the simplification that allows a homogeneous trap. For this, we can return briefly to α_k 's definition.

The homogeneous configuration

For a homogeneous trapping geometry, we can simplify the nearest-neighbor exchange constant by setting $\alpha_k = \alpha_N$ and adjusting Equation (3.21) accordingly

$$\alpha_N = N! \int_{x_1 < \dots < x_N} dx_1 \dots dx_N \delta(x_1 - x_2) \left| \frac{\partial \Psi_{SF}}{\partial x_1} \right|^2. \quad (3.23)$$

Using this form, one can compute the thermodynamic limit of the α_N 's. The detail of the derivation can be found in Appendix A.2 and lead to [Barfknecht et al., 2021, Aupetit-Diallo et al., 2022]

$$\alpha_N = \sum_{n=1}^N (k_n^\infty)^2 = \begin{cases} \frac{N(N^2 - 1)}{3L^3} \pi^2, & \text{for PBC} \\ \frac{N(N+1)(2N+1)}{6L^3} \pi^2, & \text{for DBC} \end{cases}. \quad (3.24)$$

This result was already found in [Barfknecht et al., 2021] and can be guessed from Equation (3.23).

Consequently, we can rewrite the energy slope in a concise way as

$$K(a_P) = \frac{\hbar^4}{m^2} 2S \alpha_N, \quad (3.25)$$

where $S = \sum_{P,Q} (a_P - a_Q)^2 \alpha_k / 2 + \sum_{P'} a_{P'}^2 \alpha_{k'}$ is a ponderated counting of the number of possible symmetric exchanges in the system. For instance, if we consider a gas of N TB, every exchange will be fully symmetric and contribute with a weight of 1 to S . In contrast, a not fully symmetric exchange, generated between particles of different spins, for instance, will contribute with a lower weight, while a fully anti-symmetric state will not contribute at all. It means that for TB or the ground state of a spin mixture (which must be the most symmetric), we have $S = N$ in the presence of PBC and $S = N - 1$ for DBC, while $S = 0$ for SF in any geometry.

We have found a criterion to order the different states of a spin mixture at large repulsion - the energy slope must be maximum - and have also expressed this energy slope in terms of the a_P 's. Thus, we have gathered all the elements for building the procedure, allowing us to find the a_P 's and the energies of each state.

The Volosniev matrix

For the method to be complete, we still have to find a manner to compute the a_P 's that define the ground state manifold. We can rely on the functional $K(a_P)$ for this. We know that this quantity must be maximized for the energy to be minimized. One common method for solving such optimization problems is through the Lagrange multipliers. This technique requires constraints, and in our case, we have two: 1) the normalizations of the a_P 's, $\sum a_P^2 = 1$, and 2) the maximization of the slope. With these two conditions, we can build the Lagrange function \mathcal{L} with one multiplier λ

$$\mathcal{L} = K(a_P) + \lambda \left[\sum a_P^2 - 1 \right], \quad (3.26)$$

which leads to the following system for fermionic mixtures

$$\begin{cases} \frac{\partial \mathcal{L}}{\partial a_P} = 0 \\ \frac{\partial \mathcal{L}}{\partial \lambda} = 0 \end{cases} \implies \begin{cases} \frac{\partial K}{\partial a_P} = -2\lambda \sum a_P \\ \sum a_P^2 = 1 \end{cases}. \quad (3.27)$$

Thus, taking the first line of the precedent system, we find for mixtures of fermions

$$\alpha_N \sum_{P,Q} (a_P - a_Q) = -\lambda \sum_P a_P, \quad (3.28)$$

and this is equivalent to diagonalizing a matrix V with $+\alpha_N$ coefficient in diagonal and $-\alpha_N$ off-diagonal. However, when working with bosons, we must include an additional $+2\alpha_N$ diagonal term for every adjacent indistinguishable boson. This can be expressed for the element of the Volosniev matrix as

$$[V]_{i,j} = \begin{cases} \sum_{d,k \neq i} \alpha_N + 2 \sum_{b,k \neq i} \alpha_N & i = j \\ -\alpha_N & i \neq j \end{cases}, \quad (3.29)$$

where the d -sum has to be taken over snippets k that transpose distinguishable particles, while the b -sum involves snippets that transpose identical bosons. We can obtain the b -sum by incorporating the $K_{\sigma,\sigma}$ contribution to K in the Lagrange function. Following the same steps as for spin mixtures of fermions, a $+2 \sum_P a_P$ term will be added to Equation (3.28) whose P sum runs over snippet containing adjacent identical bosons. To clarify the obtaining of V , we have provided in Appendix A.2, examples of the derivation of V for $2 + 2$ bosonic and fermionic mixtures in the presence of PBC and DBC.

As a side note, we need to discuss the variations found on this matrix briefly. The Volosniev matrix is affected by the choice of mapping for the ansatz. Here, we have set the mapping on Ψ_{SF} , which means that moving from one snippet to another (by swapping particles) is anti-symmetric by default. This explains the minus sign on the off-diagonal part of the matrix. Moreover, it implies that the a_P 's - the coefficient of the snippets - must compensate for this anti-symmetry with identical

bosons. In contrast, if we select a mapping on Ψ_{TB} , the exchanges will be symmetric, and the compensation will be on fermions, leading to positive off-diagonal terms.

Prior to moving forward, it should be noted that the Volosniev formalism assumes a_P to be real-valued. As a result, the approach produces the same state as the Bethe ansatz method up to a phase. While this method is ideal for any trapped mixtures, one must be careful while describing PBC. However, a particularly well-fitted system for this method and still having PBC are balanced bosonic and fermionic mixtures. No phase is exhibited while placed in their ground state or most excited state, and this method gives the exact states, as we will explore in Chapter 5.

In summary, the Volosniev method requires only two ingredients: *natural orbitals* for constructing the mapping spatial wave function and *diagonalization of a simple matrix* for obtaining the $K(a_P)$'s and a_P 's for the spin part of the wave function and spectrum. These two essential components are readily available in most configurations, which accounts for the success of this approach.

3.2.2 Equivalence to the XXZ spin chain

The following part will present the analogy between our 1D spin model at large contact interaction and an anisotropic spin chain. For this, let us consider Equation (3.1) in the case of a two-component mixture and rewrite in the ensuing way

$$\hat{H}_{\uparrow\downarrow} = - \sum_{\sigma=\uparrow,\downarrow} \left[\sum_{i=1}^{N_\sigma} \frac{\hbar^2}{2m} \frac{\partial^2}{\partial x_{\sigma,i}^2} + g_{\sigma,\sigma} \underbrace{\sum_{1 \leq i < i' \leq N_\sigma} \delta(x_{\sigma,i} - x_{\sigma,i'})}_{V_{int}^{(\sigma,\sigma)}} \right] + g_{\uparrow,\downarrow} \underbrace{\sum_{i=1}^{N_\sigma} \sum_{i' < i'}^{N_{\sigma'}} \delta(x_{\uparrow,i} - x_{\downarrow,i'})}_{V_{int}^{(\uparrow,\downarrow)}}, \quad (3.30)$$

where we have separated the inter-species and intra-species interaction potential $V_{int}^{(\uparrow,\downarrow)}$ and $V_{int}^{(\sigma,\sigma)}$. In this configuration, the spin part of this model can be mapped onto the anisotropic Heisenberg spin chain \hat{H}_{XXZ} . This is made possible by suitably redefining the strengths of the interactions as $g_{\sigma,\sigma} = \frac{2}{1-\Delta}g$ and $g_{\uparrow,\downarrow} = g$, with Δ the z -axis anisotropy of \hat{H}_{XXZ} .

The method for connecting the two precedent models is to introduce another spin Hamiltonian \hat{H}_σ , which will be an intermediary. This one reads [Volosniev et al., 2015]

$$\hat{H}_\sigma(J_N, \Delta) = -J_N \sum_{j=1}^{\tilde{N}} \left[\underbrace{\frac{1}{2}(\vec{\sigma}^j \vec{\sigma}^{j+1} - \mathbb{1})}_{V_{int}^{(\sigma,\sigma')}} - \underbrace{\frac{1-\Delta}{2}(\sigma_z^j \sigma_z^{j+1} + \mathbb{1})}_{\sum_\sigma V_{int}^{(\sigma,\sigma)}} \right], \quad (3.31)$$

where the J_N 's are the hopping constants which take the form $J_N = \alpha_N/g$, the σ_i matrices refer to the i component of the Pauli matrix $\vec{S} = (S_x, S_y, S_z)$, and $\tilde{N} = N$ for PBC and $N - 1$ otherwise. This Hamiltonian has a simple expression in terms of the anisotropic spin chain in the homogeneous H_{XXZ} [Volosniev et al., 2015]

$$H_\sigma(J_N, \Delta) = H_{XXZ}(2J_N, \Delta, h = 0) - \frac{2 - \Delta}{2} J_N \sum_{j=1}^n \mathbb{1}, \quad (3.32)$$

where in the homogeneous case we have

$$\hat{H}_{XXZ}(J_j, \Delta, h) = -J_N \sum_{j=1}^{\tilde{N}} [S_x^j S_x^{j+1} + S_y^j S_y^{j+1} + \Delta S_z^j S_z^{j+1}] - 2h \sum_{j=1}^{\tilde{N}} S_z^j, \quad (3.33)$$

In general, this Hamiltonian is defined with the strength h of an external magnetic field in the z -axis. In the framework of our discussion, we have decided to set it to zero. Still, it could be placed back at any moment to generalize the future results to the application of an external magnetic field in the z -axis. The hopping constants are chosen to be positive, which means that \hat{H}_{XXZ} corresponds to an anti-ferromagnetic spin chain. Thus, the case $\Delta = 1$ will correspond to a fermionic mixture. In contrast, we fall back to the Hamiltonian describing bosons by setting $\Delta = -1$ in Equation (3.30) with the redefined interaction strengths. With this model, we can also move from describing fermions to bosons - thus to ferromagnetic chain - by changing the sign of J . However, in our case, it would correspond to changing the mapping from Ψ_{SF} to Ψ_{TB} and then all the precedent definitions. So, to seek consistency, we will only use Δ to choose which type of particle we want to describe.

After taking the limit of large repulsion $g \rightarrow \infty$, the relation between the three Hamiltonians can be summarized as follows

$$\hat{H}_{\uparrow\downarrow}(g, \Delta) \xrightarrow{g \rightarrow \infty} = H_\sigma(J_N, \Delta) \quad (3.34)$$

$$= H_{XXZ}(2J_N, \Delta, h = 0) - \frac{2 - \Delta}{2} J_N \sum_{j=1}^{\tilde{N}} \mathbb{1}. \quad (3.35)$$

With that in mind, we can rewrite a Volosniev matrix that accounts for a slight difference between the inter- and intra-species strength at large interaction. This matrix can be defined as follows

$$[V]_{i,j} = \begin{cases} \sum_{d,k \neq i} \alpha_N + (1 - \Delta) \sum_{b,k \neq i} \alpha_N & k = i \\ -\alpha_N & k \neq i \end{cases}, \quad (3.36)$$

with $\Delta = 1$ corresponding to Fermions, and $\Delta = -1$ to Bosons.

This mapping has important implications for the theoretical treatment of 1D spin mixtures. Since the XXZ spin chain is an integrable model, $\hat{H}_{\uparrow\downarrow}$ must have at least the same domain of integrability, opening up a new class of integrable systems where $g_{\sigma,\sigma}, g_{\uparrow,\downarrow} \rightarrow \infty$ but $g_{\sigma,\sigma} \neq g_{\uparrow,\downarrow}$. A special case within this category of integrable models will be explored further in Chapter 5 [Aupetit-Diallo et al., 2022].

3.3 The $SU(n)$ symmetry

The concept of symmetry is fundamental to the field of physics and deeply rooted in nature. It has significant implications for understanding the laws governing the universe [Curie, 1894]. Symmetry refers to physical laws' invariance under certain transformations, like translational or rotational. For instance, symmetry analysis is an indispensable tool in field theory, such as electromagnetism or relativity [Curie, 1894, Einstein, 1905a]. This is thanks to E. Noether's theorem [Noether, 1918], which establishes a link between symmetries and conserved quantities - essential in physical systems. Yet, the importance of symmetry is not limited to its direct presence; it is also relevant when broken. Symmetry breaking plays a crucial role in explaining phenomena like the origin of mass [Englert & Brout, 1964, Higgs, 1964], phase transitions [Kittel, 1976], and the formation of structures in the universe [Kibble, 1976].

In quantum mechanics, the significance of symmetries makes no exception [Landau & Lifshitz, 2013, Greiner & Müller, 1989]. In this formalism, considering the group representation of these symmetries is often more convenient. For instance, the translational or rotational invariance will now be mediated by the representation of $E(3)$ (3D Euclidean group) and $SO(3)$ (3D rotational group). Although this approach adds a layer of abstraction, it provides an efficient tool for analyzing complex systems, such as unveiling more subtle symmetries with no classical counterpart. Among these intriguing group symmetries, we will carry our interest onto the special unitary group $SU(n)$.

This symmetry generally arises when a quantum process conserves an intrinsic quantity of the system constituents. For instance, the $SU(2)$ symmetry is associated with spin- $\frac{1}{2}$ conservation, or the $SU(3)$ with the color charge conservation in quantum chromodynamics [Kota, 2020]. In the context of 1D spin mixtures with contact interactions, we need the masses of the particles m , and the interaction strengths ($g_{\sigma\sigma}$, and $g_{\sigma\sigma'}$) to be equal while the particles must feel the same overall potential. In this configuration, the interaction - thus the collisions - prevents spin-flip, and the number of particles per spin state (labeled for 1 to κ) is conserved. Thereby, the corresponding Hamiltonian will present a $SU(\kappa)$ interaction symmetry and will read in the homogeneous case

$$\hat{H}_{SU} = -\frac{\hbar^2}{2m} \sum_{i=1}^N \frac{\partial^2}{\partial x_i^2} + g \sum_{i<j} \delta(x_i - x_j), \quad (3.37)$$

From now on, we will refer to this model as $SU(\kappa)$ spin mixture.

Although the symmetry of the Hamiltonian is well-established, defining the symmetry of an arbitrary state is not straightforward. The common method employs the much simpler and well-known symmetric group S_n , which shares the same representation than $SU(n)$ [Greiner & Müller, 1989]. Before going into detail, let us briefly outline the following process.

The representations of S_n are called Young's Diagrams. These representations, constituted of collections of rows and columns of boxes, are often used to discuss the overall symmetry of functions. In physics, they have been extensively used for describing many-particle systems. Precisely, by assigning the canonical symmetrizer

and anti-symmetrizer to rows and columns, a line diagram $\square\square\square$ will then corresponds to a fully symmetric state and a column $\begin{array}{|c|} \hline \square \\ \hline \square \\ \hline \square \\ \hline \end{array}$ to a fully anti-symmetric state,

with all other possibilities representing more exotic states. However, a more efficient method is required to link a state and a symmetry when N increases. For this, we will construct a Complete Set of Commuting Operators (CSCO), including \hat{H}_{SU} , in the same way that we treat angular momentum in quantum mechanics. Once diagonalized, numbers will label each state - the central characters - (the analogous to n , l , and m in moment study), which will allow a one-to-one correspondence between the states of \hat{H}_{SU} and the Young's diagrams, thus the symmetry.

As a preliminary step, we will first present some generalities about S_n , its representations, and then properly define what we imply by "symmetry of a physical state".

3.3.1 Define and characterize permutational symmetry: the Young's diagrams

The S_n symmetry is a standard feature of many-particle systems. In the $SU(\kappa)$ configuration, swapping two particles will not change the system's solution (up to a sign) because the collisions do not modify the particle's spin. Formally, this exchange (or permutational) symmetry is translated by a symmetry group (S_n) invariance of the Hamiltonian.

To understand which ingredients are needed to discuss the symmetry of our system, let us go back to the definition of the group invariance of a Hamiltonian \hat{H} . If \hat{H} present a certain group symmetry G we have that for every element g of G [Hamermesh, 1962]

$$[\hat{H}, \hat{D}(g)] = 0, \tag{3.38}$$

where the representation \hat{D} belong to the Hilbert space of the system. Because \hat{D} can be split as a direct sum of irreducible representation (irreps.) - or non-zero representation, which has no sub-representation - \hat{H} can be split equivalently to these irreps. as well as its spectrum [Maschke, 1898, Maschke, 1899].

To understand the implication on our system, let us consider the strong interaction limit of the $SU(\kappa)$ scenario. In this case, we have seen that \hat{H}_{SU} reduces to a spin chain Hamiltonian. This Hamiltonian can easily be expressed in terms of permutation matrices as [Deuretzbacher et al., 2014]

$$\hat{H}_P = (E_F - \tilde{N}J_N)\mathbb{1} \pm J_N \sum_{j=1}^{\tilde{N}} \hat{P}_{j,j+1}, \tag{3.39}$$

where the + (resp. -) sign stands for fermions (resp. bosons), and $\tilde{N} = N$ for PBC and $N - 1$ otherwise. Because every permutation matrices commute two by two, it implies that the $N!$ \hat{P} 's commute with \hat{H}_P . These permutation matrices are, in fact, the representation of the element of the symmetric group, meaning that \hat{H}_P presents a S_N symmetry. The intuition from this little development is that if one

can find irreps. of S_N it will provide an eigenbasis to investigate the permutational symmetry of \hat{H}_P .

Generalities about S_n and their irreps.

As an initial step, we must properly characterize the permutational group and some notion belonging to it. First of all, S_n is defined as the group of all permutations of n distinct elements

$$P = \begin{pmatrix} 1 & 2 & \cdots & n \\ P(1) & P(2) & \cdots & P(n) \end{pmatrix}. \quad (3.40)$$

Every permutation could be decomposed as a product of cyclic permutation or cycle. A l -order cycle is a permutation that preserves $(n-l)$ objects invariants and changes the l others in order, formally they read [Ma, 2007]

$$S_l = \begin{pmatrix} a_1 & a_2 & \cdots & a_{l-1} & a_l & b_1 & \cdots & b_{n-l} \\ a_2 & a_3 & \cdots & a_l & a_1 & b_1 & \cdots & b_{n-l} \end{pmatrix}, \quad (3.41)$$

$$= (a_1 \ a_2 \ \cdots \ a_{l-1} \ a_l) = (a_2 \ a_3 \ \cdots \ a_l \ a_1), \quad (3.42)$$

with the following property $S_l S'_l = S'_l S_l$. As a consequence, it appears that all $n!$ permutations of S_n are not independent. However, in our search of irreps. of S_n , we rather have to consider the l -cycle as opposed to the elementary permutations. Thus, we need a strategy to categorize the $n!$ permutation composing S_n in terms of their l -cycle decomposition. For this, let us introduce the notion of the conjugacy class of a permutation $cc_{[\Lambda]}(P)$. This class gathers all permutations whose decomposition in disjoint cycles has the same structure as P and is defined by the partitions $[\Lambda] = [\lambda_1, \dots, \lambda_j]$ of $\{1, \dots, n\}$ of the form

$$\lambda_1 \geq \cdots \geq \lambda_n > 0, \quad \text{with} \quad \sum_l \lambda_l = n. \quad (3.43)$$

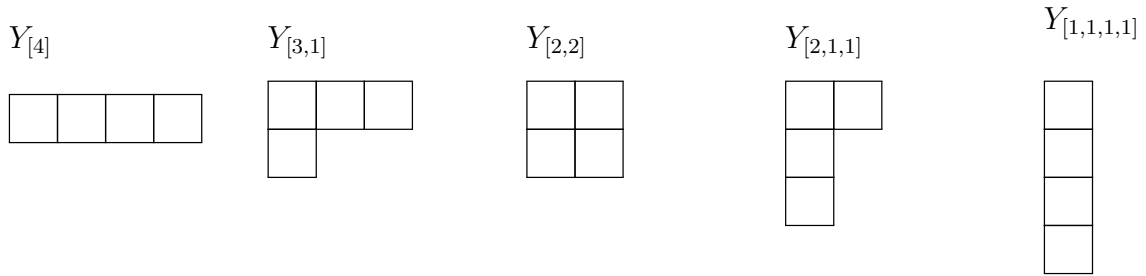
As the number of unequal irreps. of a finite group is equal to its number of classes [Ma, 2007], these classes constitute proper tools to classify all the irreps. of S_n . To be precise, it implies that every irrep. of S_n can be described by a partition $[\Lambda]$ of n . The number of these partitions $p(n)$ for the group S_n is given by a generating function of the form [Abramowitz et al., 1971]

$$\sum_{n=0}^{\infty} p(n) q^n = \prod_{j=1}^{\infty} \sum_{i=0}^{\infty} q^{ji} = \prod_{j=1}^{\infty} \frac{1}{1 - q^j}, \quad (3.44)$$

which, for $N = 0, 1, 2, \dots$, gives $1, 1, 2, 3, 5, 7, 11, 15, 22, 30, 42, 56, 77, 101, \dots$ [OEIS Web Site]. For every $[\Lambda]$ - thus irrep. of S_n - one can associate a Young's diagram (or pattern) $Y_{[\Lambda]}$. These diagrams are collections of boxes that, by convention, have equal or increasing numbers of boxes per line from right to left and line while going up. For instance the partition $[3, 2, 2, 1]$ of 8 will correspond to the ensuing Young's diagram

$$Y_{[3,2,2,1]} = \begin{array}{|c|c|c|} \hline \square & \square & \square \\ \hline \square & \square & \\ \hline \square & \square & \\ \hline \square & & \\ \hline \end{array} . \quad (3.45)$$

Let us illustrate the different results presented by considering the irreps. of S_4 . Using Equation (3.44), we know that the set $\{1, 2, 3, 4\}$ presents five distinct partitions of the type $[\Lambda]$. Thus, the Young's diagrams associated with the five possible irreps. of S_4 are the following



Along with $Y_{[\Lambda]}$, introducing the Young's tableaux is often convenient. Young's tableaux are simply Young's diagrams filled with digits or letters. They could be of a large variety of forms depending on the filling rules, but they are merely divided into two categories: standard and non-standard. The standard Young's tableaux gather the ways to fill Young's diagrams with digits strictly increasing from left to right and going up. The non-standard Young's tableaux are all the others. The two possibilities are illustrated in Table 3.2 for the case of $Y_{[3,2,2,1]}$ filling.

Table 3.2: Example of standard and non-standard filling of $Y_{[3,2,2,1]}$.

Standard				Non-standard								
1	2	3		4	7	8	10	7	3	<i>a</i>	<i>a</i>	<i>a</i>
4	5			2	6		3	2		<i>b</i>	<i>b</i>	
6	7			3	7		1	2		<i>a</i>	<i>b</i>	
8				4			1			<i>a</i>		

For a given Young's diagram $Y_{[\Lambda]}$, the number of standard Young's tableaux (i.e. standard filling of $Y_{[\Lambda]}$) is

$$d_{[\Lambda]}(S_N) = \frac{N!}{\prod_{ij} h_{ij}}, \quad \text{with} \quad \sum_{[\Lambda]} (d_{[\Lambda]}(S_N))^2 = N!, \quad (3.46)$$

where h_{ij} refer to the Hook's length of the (i, j) box of $Y_{[\Lambda]}$. For a box at position (i, j) , the Hook's length is the number of boxes at its right and under, plus one. In order to clarify this notion, let's fill $Y_{[3,2,2,1]}$ with its Hook's lengths

6	4	1	
4	2		
3	1		,
1			

which give for the associated dimension, $d_{[3,2,2,1]}(S_8) = 8!/(6 \cdot 4 \cdot 1 \cdot 4 \cdot 2 \cdot 3 \cdot 1 \cdot 1) = 70$.

We have successfully obtained the irreps. of S_n and defined all the necessary elements to build a basis for discussing symmetry. Therefore, we have everything we need to define permutational symmetries properly.

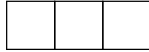
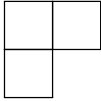

Young's diagrams and permutational symmetries

In general, Young's diagrams can be used to schematize various problems. Their meaning is only fixed when is specified the relation between the boxes. As an illustration, Young's diagram range of applications goes from card game theory to word classification [Ma, 2007]. However, these representations have particularly shone in quantum mechanics using their faculty to describe the symmetry of functions. Indeed, as we have two types of exchange of symmetry (symmetric or anti-symmetric), by assigning one kind to the column and the other to the line, we can virtually describe any type of spin mixture. Precisely, two boxes on the same horizontal and vertical line, we now adjoin the symmetrizer and anti-symmetrizer $\hat{S} = \mathbb{1} + \hat{P}$ and $\hat{A} = \mathbb{1} - \hat{P}$. By this means, the application of the operators \hat{S} and \hat{A} associated with a Young diagram $Y_{[\Lambda]}$ on an arbitrary spin configuration $|1, 2, 3, \dots\rangle$ will result in a vector decomposed on the sectors' basis with the symmetry of $Y_{[\Lambda]}$.

To illustrate this description of physical states, let us consider an arbitrary mixture of three particles. The corresponding symmetry group will be S_3 whose irreps. are $Y_{[3]} = \square\square\square$, $Y_{[2,1]} = \begin{array}{|c|c|} \hline \square & \square \\ \hline \square & \\ \hline \end{array}$, and $Y_{[1,1,1]} = \begin{array}{|c|} \hline \square \\ \hline \square \\ \hline \square \\ \hline \end{array}$. $Y_{[3]}$ represents a fully symmetric vector, $Y_{[1,1,1]}$ a fully anti-symmetric vector, and $Y_{[2,1]}$ a vector with partial (or mixed) overall symmetry. In order to visualize and clarify what represents these diagrams in terms of symmetry, we have to explicitly state which operators \hat{S} and \hat{A} are associated in Table 3.3. It is important to note that applying \hat{A} before \hat{S} will change the result. In particular *the operator applied last controls the result* [Greiner & Müller, 1989].

The vectors $\{\Phi_S, \Phi_1, \Phi_2, \Phi_3, \Phi_4, \Phi_A\}$ are linearly independent and constitute a proper basis, although not irreducible, for describing all symmetry states possible of any three-particle mixture. However, while $Y_{[3]}$ and $Y_{[1,1,1]}$ are described by one vector, the mixed symmetry diagram generates a subspace of higher dimension. Indeed, while mixed diagrams properly characterize an overall symmetry, they left undefined the inner relation between its elements. To lift this degeneracy, a natural way is to label the boxes and consider Young's tableaux instead of diagrams. The correct vectors are then the standard Young's diagrams if we choose the snippet basis to describe our state. If, instead, we prefer the sectors basis, we must consider all non-standard Young's tableaux that correspond to a horizontal permutation of the entries of the standard ones. For more details, see [Greiner & Müller, 1989].

Table 3.3: Young's diagrams of S_3 and their corresponding physical states.

	$\Phi_S = \hat{S}_{123}(1, 2, 3)$
	$\Phi_1 = \hat{A}_{13}\hat{S}_{12}(1, 2, 3), \quad \Phi_2 = \hat{A}_{23}\hat{S}_{12}(1, 2, 3),$ $\Phi_3 = \hat{A}_{12}\hat{S}_{13}(1, 2, 3), \quad \Phi_4 = \hat{A}_{23}\hat{S}_{13}(1, 2, 3).$
	$\Phi_A = \hat{A}_{123}(1, 2, 3)$

We have the tools to assign a clear symmetry to the physical states obtained through Volosniev formalism. However, finding all the irreps. and good tableaux to form the proper basis can be time-consuming as the vectors generated by the Young's diagrams (resp. the Young's tableaux) are not orthogonal in the snippet basis (resp. the sectors basis). With that in mind, we will present a procedure to ease the link between the spin states and their symmetries.

3.3.2 Complete set of commuting operators of S_n

The theory of representation of S_n is an elegant manner to address the symmetry analysis of functions, with the heavy counterpart of being effectively hard to handle for newcomers. A. V. Sokolov has enlightened this statement [Sokolov & Shirokovskii, 1961] in the following way: "Due to the fact that group, especially the theory of representation of the permutation group, is extremely difficult even for specialists, there arose the tendency of opposing the so-called 'group pest' in quantum mechanics.". Thus, to extend the utilization of this method, we need to make the austere group theory formalism more accessible. In our context, a natural way is to move toward to the quantum mechanics language and construct CSCO [Cohen-Tannoudji et al., 1986] of S_n . For the reader interested in the original group formalism, see [Frobenius, 1896, Yamanouchi, 1937, Hamermesh, 1962]

In the following part, the approach will rely on the class sum method, namely the first kind of CSCO of S_n (or CSCO-I). For more information on the theory of CSCO of S_n or an example of other CSCO types used for physical applications, see [Ping et al., 2002] and [Nataf & Mila, 2014].

CSCO-I and class-sum operators

In group theory, the class sum method is used to compute the number of elements in each conjugacy class of a finite group and classify them. The motivation was initially to investigate and characterize the structure of the numerous finite groups and was developed in the late 19th and early 20th thanks to G. Frobenius [Frobenius, 1896] but was already used by C. F. Gauss. Soon, physicists understood the efficiency of this method in studying the symmetry of states. First, by P. Dirac [Dirac, 1929] in the context of many-body systems of electrons. Afterward, it has spread into

particle [Greiner & Müller, 1989] and nuclear physics [Kota, 2020] for its efficiency in addressing many-particle problems, furnishing an efficient way to compute Clebsh-Gordan coefficients for instance.

In the context of 1D strongly interactive spin mixtures, the utility of the class sum method has first been unveiled in [Fang et al., 2011]. The complete group theory background, and particularly the class-sum method application to the irreps. of S_n , has been presented in [Katriel, 1993, Decamp et al., 2016a, Decamp et al., 2016b]. For our purpose, this method boils down to finding a basis where \hat{H}_P , Equation (3.39), and some wisely chosen sum of \hat{P} , commute altogether. The idea is analogous to the procedure for analyzing the angular momentum of an isolated system with rotational symmetry. While the momentum components $\hat{L}_{x,y,z}$ all commute with the Hamiltonian of the system, they do not commute with each other. However, one can construct a sum operator $\vec{L}^2 = \hat{L}_x^2 + \hat{L}_y^2 + \hat{L}_z^2$ which form the CSCO $\{\hat{H}, \vec{L}^2, L_z\}$ whose states are characterised by their quantum numbers $\{n, l, m\}$.

While dealing with permutational symmetry, the sum operators commuting with \hat{H}_P and altogether are called class sum operators and reads for the conjugacy class of permutation $[\Lambda]$

$$\hat{\Gamma}^{[\Lambda]} = \sum_{P \in cc_\Lambda} P, \quad (3.47)$$

where the sum has to be taken over all the elements of the conjugacy class. The dimension of cc_Λ of S_n for the partition $[\Lambda] = [(a_1)_1(a_2)_2 \cdots]$ composed by a number a_1 of 1-cycles, a_2 of 2-cycles, and so on is given by

$$|cc_\Lambda| = \frac{n!}{\prod_j (j)^{a_j} (a_j!)}. \quad (3.48)$$

In our case, the only relevant class sum operator will correspond to a single r -cycle, namely to the class $[\Lambda] = [r, 1, \dots, 1] = [r]$ with dimension $|cc_r| = n!/(n-r)!r$. For this scenario, the class sum operators read

$$\hat{\Gamma}^{[2]} = \frac{1}{2} \sum_{i \neq j} \hat{P}_{ij}, \quad (3.49)$$

$$\hat{\Gamma}^{[3]} = \frac{1}{2} \sum_{i \neq j \neq k} \hat{P}_{ij} \hat{P}_{jk}, \quad (3.50)$$

and so on. The factor $\frac{1}{2}$ must be taken as these expressions count twice the elements of the conjugacy class (it is a consequence of the symmetry of the permutations). It must be pointed out that these expressions of the class sum operators do not depend on the representation chosen for the \hat{P} . To explain the subtleties of this procedure, a comprehensive derivation of the $\Gamma^{[r]}$ matrices in the case of 2 + 2 mixtures has been provided in Appendix B.

The eigenvalues $\gamma_{[\nu]}^{[\Lambda]}$ of the operators $\hat{\Gamma}^{[\Lambda]}$ are called central characters, with the partition $[\nu] = [\nu_1, \dots, \nu_m]$ referring to a Young's diagram $Y_{[\nu]}$. For r -cycles, i.e. $[\Lambda] = [r]$, they admit the following analytic expression [Katriel, 1993, MacDonald, 1979, Decamp et al., 2016a]

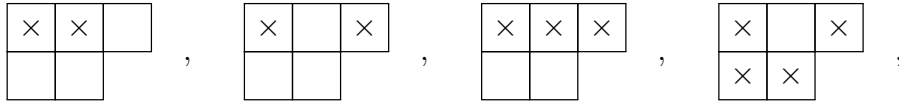
$$\gamma_{[\nu]}^{[r]} = \frac{1}{r} \sum_{i=1}^m \frac{\mu_i!}{(\mu_i - r)} \prod_{j \neq i} \frac{\mu_i - \mu_j - r}{\mu_i - \mu_j}, \quad (3.51)$$

with $\mu_i = \nu_i - i - m$, and the product is put to unity when $[\nu]$ represent a line diagram ($m = 1$). For $n = 2$, and 3 Equation (3.51) reduces to more practical formulas [Ping et al., 2002]

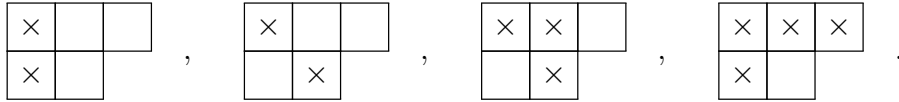
$$\gamma_{[\nu]}^{[2]} = \left\{ \begin{array}{l} \frac{n}{2} + \frac{1}{2} \sum_{i=1}^m \nu_i (\nu_i - 2i) \\ \sum_{(i,j) \in [\nu]} (j - i) \end{array} \right\}, \quad (3.52)$$

$$\gamma_{[\nu]}^{[3]} = \frac{1}{3} \left\{ 2n - \frac{3}{2} n^2 + \sum_{i=1}^m \nu_i \left[\nu_i^2 - \left(3i - \frac{3}{2} \right) \nu_i + 3i(i - 1) \right] \right\}. \quad (3.53)$$

In the case of r -cycle, all the possible values of the $\hat{\Gamma}^{[r]}$ matrices can be linked with Young's diagrams. Moreover, the values of $\gamma_{[\nu]}^{[r]}$ are directly interpreted as the counting of r -cyclic permutation in the Young's diagram $Y_{[\nu]}$. In these eigenvalues, the symmetric permutation will count as +1, and the anti-symmetric permutation will count as -1. For instance, the permutation associated with the following boxes, indicated with a cross, will count as +1



whereas the permutation associated with the following boxes will count as -1



To summarize, if a permutation involves an odd (reps. even) number of boxes in different lines, it will count as +1 (resp. -1). To clarify this statement, we have presented the central characters for $r = 2, 3$ corresponding to the irreps. of S_n for $n = 4$, and 6 in Table 3.4.

For $N < 6$, there is a one-to-one correspondence between the 2-cycle central character and Young's diagrams. Consequently, if we consider the eigenstates $|a_P\rangle$ of the Hamiltonian \hat{H}_P we can assign them a unique, well-defined, symmetry using only the 2-cycle class sum operator. Precisely, we can write the central characters as $\gamma_{[\nu]}^{[2]} = \langle a_P | \hat{\Gamma}^{[2]} | a_P \rangle$ and link every physical state $|a_P\rangle$ to a $Y_{[\nu]}$. We present a complete example of such a procedure in the case of 2+2 spin mixtures in Appendix B. Interestingly, degeneracies occur when we increase the number of particles, as shown in Table 3.4. It results in the necessity to consider a higher order of class sum operators to lift the ambiguity during the assignation of Young's diagrams.

To clarify the different mandatory steps of the procedure, let us make a summary. To assign a well-defined symmetry to the N -particles eigenstates $|a_P\rangle$ of \hat{H}_{SU} , one has to

- 1) Compute all possible characters $\gamma_{[\nu]}^{[r]}$ of S_N up to an order r' that allows to lift any degeneracy,
- 2) Find all the $|cc_r|$ elements of the one r -cycle conjugacy classes cc_r of S_N , up to the order r' ,
- 3) Choose a representation to express the swapping operators \hat{P}_{ij} in the same basis than the eigenstates of \hat{H}_{SU} - the $|a_P\rangle$'s (usually sector or snippet),
- 4) Construct the class sum operators $\Gamma^{[r]}$ up to the order r' , and
- 5) Compute all the mean values $\langle a_P | \Gamma^{[r]} | a_P \rangle$ to assign a Young diagram $Y_{[\nu]}$ to every $|a_P\rangle$ without ambiguity.

Luckily, the order r' , which lifts the degeneracy of the central characters, is much lower than N , and the procedure is tractable for a reasonable number of particles.

Table 3.4: In the following, we gather all the Young's diagrams $Y_{[\nu]}$ of S_N for $N = 4$ and $N = 6$. We also provide the corresponding partitions $[\nu]$, and $\gamma_{\nu}^{[2]}$ and $\gamma_{\nu}^{[3]}$ the corresponding eigenvalues of $\hat{\Gamma}^{[2]}$ and $\hat{\Gamma}^{[3]}$, respectively.

$Y_{[\nu]}$	$[\nu]$	$\gamma_{\nu}^{[2]}$	$\gamma_{\nu}^{[3]}$
	[4]	6	8
	[3,1]	2	0
	[2,2]	0	-4
	[2,1,1]	-2	0
	[1,1,1,1]	-6	8

$Y_{[\nu]}$	$[\nu]$	$\gamma_{\nu}^{[2]}$	$\gamma_{\nu}^{[3]}$
	[6]	15	40
	[5,1]	9	16
	[4,2]	5	0
	[3,3]	3	-8
	[4,1,1]	3	4
	[3,2,1]	0	-5
	[3,1,1,1]	-3	4
	[2,2,2]	-3	-8
	[2,2,1,1]	-5	0
	[2,1,1,1,1]	-9	16
	[1,1,1,1,1,1]	-15	40

Chapter 4

Breakdown of Tan's relations induced by trapping discontinuity

This chapter constitutes the first part of the document dedicated to results obtained during this thesis. This one has been published in [Aupetit-Diallo et al., 2023]. We will focus on the momentum distribution's large k behavior. In Chapter 2, we have discussed the motivations for its study and the key results. For the consistency of the following discussion, we will perform a quick reminder here.

The momentum distribution is defined as the Fourier transform of the first-order correlation function and reads as follows

$$n(k) = \frac{1}{2\pi} \int_{\mathcal{D}^2} dx dy \rho_1(x, y) e^{ik(x-y)}, \quad (4.1)$$

Shifting to Fourier space implies that the same information as ρ_1 is carried by $n(k)$ up to an inversion of scale. Thus, the particles' behaviors at short distances, such as how they will brush themselves or their exchange symmetry [Decamp et al., 2017], will impact the large- k distribution. Precisely, the interplay between the symmetry and the contact interactions creates an algebraic decay of the momentum distribution of the form

$$n(k) \underset{k \rightarrow \infty}{\simeq} \frac{\mathcal{K}_N}{k^4}. \quad (4.2)$$

This decay arises for momentum $\hbar k$ larger than any other typical momentum scale, such as the Fermi momentum $\hbar k_F$. In general, the weight \mathcal{K}_N is directly identified as the Tan's contact \mathcal{C}_N . However, we show in this chapter how the presence of discontinuity of the confining potential, here the hard walls of the box, breaks down the Tan's relations for 1D gases at equilibrium and zero temperature [Aupetit-Diallo et al., 2023]. We find that \mathcal{K}_N not only has an average value larger than \mathcal{C}_N , but also, for strong interactions, develops oscillations, which are connected to the spin-coherence properties of the gas from one border of the potential to the other [Figure 4.1].

Trapping atoms in optical-box potentials has become increasingly popular over the last years, leading to important results in three-dimensional and two-dimensional gases [Navon et al., 2021]. Therefore, this work aims to guide future experiments using box potentials in one dimension.

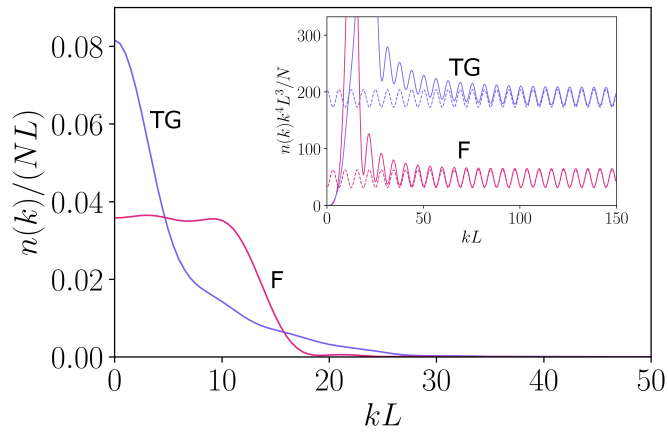


Figure 4.1: Normalized momentum distribution $n(k)/N$, in units of $1/L$, as a function of kL for four SF (magenta) and four TB (light violet). In the inset, the solid lines are the same $n(k)/N$ multiplied by k^4 , in units of L^3 , while the dashed lines correspond to the asymptotic analytical expressions given in Equations (4.21) and (4.4). Figure from [Aupetit-Diallo et al., 2023].

We exemplify our findings using the two one-component systems of SF and TB before generalizing them to arbitrary mixtures of quantum particles with infinite interactions. Using this last case, we will demonstrate how the new behavior of the momentum distribution can be used experimentally to probe the state of a spin mixture of a 1D system.

4.1 Large- k tail of the momentum distribution in the box for identical particles

In order to investigate the effect of hard walls, we will discuss in this section two simple examples of 1D quantum gases at equilibrium in a box geometry ($x \in [-L/2, L/2]$) and at zero temperature. We begin with a non-interacting Fermi gas whose momentum distribution does present algebraic tail in the homogeneous ring trap or in the presence of smoothly varying potentials [Figure 4.1]. The second example will be the TG gas in a box, whose many-body wave function only differs from one of the SF by the particle-exchange symmetry.

4.1.1 Spinless non-interacting fermions

We now consider 1D spinless fermions trapped in a box of size L . As we have seen in Chapter 2, the first-order correlation function can be expressed as a DPP, which takes the explicit form [Lacroix-A-Chez-Toine et al., 2018, Meckes, 2019]

$$\rho_1^{SF}(x, y) = \frac{1}{2L} \left[\frac{\sin \left[(2N+1) \frac{\pi}{2L} (x-y) \right]}{\sin \left[\frac{\pi}{2L} (x-y) \right]} - \frac{\sin \left[(2N+1) \frac{\pi}{2L} (x+y+L) \right]}{\sin \left[\frac{\pi}{2L} (x+y+L) \right]} \right], \quad (4.3)$$

with $|x|, |y| \leq L/2$. As explained in Chapter 2, calculating the momentum distribution tail boils down to investigating non-analyticities (or cusps) of ρ_1 . We recall that such cusps are usually developed by the interplay between the interaction potential (the vanishing of Ψ in the contact regions) and the type of exchange symmetry of the particles. In particular, only symmetric exchanges between particles generate cusps. To clarify this statement, we have provided in Figure 4.2 the two-body wave function $\Psi(x, y)$ at fixed $y = 0$, for $N = 2$ SF and TB, in the system under consideration. As expected, at the contact point, we observe no cusps for fermions. However, two new non-analiticities appear at the borders for both SF and TB. It implies that $n(k)$ of SF must now exhibit a $1/k^4$ power law decay despite having no Tan's contact. This constitutes the first evidence of a breakdown of Tan's relation. In particular, considering Figure 4.1 it appears that $n(k)$ of SF displays an oscillatory algebraic decay of the form [De Bruyne et al., 2021, Aupetit-Diallo et al., 2023]

$$\lim_{k \rightarrow \infty} k^4 n^{SF}(k) = \mathcal{K}_N^{SF} = \mathcal{B}_N + (-1)^{N+1} \mathcal{A}_N \cos(kL), \quad (4.4)$$

whose contribution \mathcal{B}_N , \mathcal{A}_N , and the oscillation period are explicitly derived right after. We remark that contrary to the cusp induced by contact, the singularities at the borders do not appear if we plot $\Psi(x, y)$ as a function of the relative distance $x - y$. Therefore, they cannot be derived by a change of coordinates in $\rho_1(x, y)$ as done in Equation (2.48).

The developed method separates the asymptotic treatment of the momentum distribution. First, we consider the same edge contribution and, afterward, the opposite edges to obtain new terms of the tail's algebraic decay \mathcal{K}_N^{SF}/k^4 . To achieve this, we recall the Watson's lemma: the asymptotics of the Fourier transform of functions of the form $f(z) = F(z)|z - z_0|^\alpha$, with $F(z)$ a regular function, and $\alpha > -1$ and $\alpha \neq 0, 2, 4, \dots$ reads [Bleistein & Handelsman, 1986, Olshanii & Dunjko, 2003]

$$\int_{\mathcal{D}} dz e^{-ikz} F(z)|z - z_0|^\alpha \underset{k \rightarrow \infty}{=} \mathcal{F}_\alpha \frac{e^{-ikz_0} F(z_0)}{|k|^{\alpha+1}} + \mathcal{O} \left(\frac{1}{|k|^{\alpha+2}} \right), \quad (4.5)$$

with $\mathcal{F}_\alpha = 2 \cos[\pi(\alpha + 1)/2] \Gamma(\alpha + 1)$ and $\Gamma(\alpha)$ is the Gamma function, and rewrite the momentum distribution in a suitable form

$$n(k) = \frac{1}{2\pi} \int_{-L/2}^{L/2} dx e^{ikx} \int_{-L/2}^{L/2} dy e^{-iky} \rho_1(x, y). \quad (4.6)$$

Therefore, by looking at Figure 4.2, the contributions to the $1/k^4$ tail of $n(k)$ emerging from the presence of the border could be seen as non-analytic terms of the form $|x - \pm L/2|$ in $\Psi(x, x_2, \dots)$.

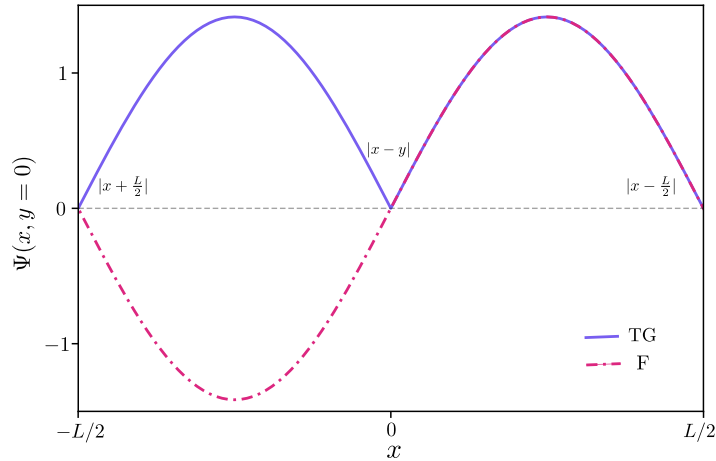


Figure 4.2: Two-body wave function $\Psi(x, y)$ with $y = 0$ for SF (solid line) and TB (dash-dotted line) trapped in a box of size L . We clearly distinguish three different points of non-analyticity, at $|x \pm L/2|$ (for SF and TB) and $|x - y|$ (only for TB). Figure from [Aupetit-Diallo et al., 2023].

Same edge contribution:

We identify a first type of singularity of ρ_1 - in the vicinity of $|x \pm L/2||y \pm L/2|$ - and will refer to the corresponding contribution to \mathcal{K}_N^{SF} as \mathcal{B}_N . This one is defined as

$$\frac{\mathcal{B}_N}{k^4} \underset{k \rightarrow \infty}{=} \int_{-L/2}^{L/2} dx e^{ikx} \int_{-L/2}^{L/2} dy e^{-iky} \left[\underbrace{\lim_{\substack{x \rightarrow +L/2 \\ y \rightarrow +L/2}} \frac{\rho_1^{SF}(x, y)}{|x - \frac{L}{2}||y - \frac{L}{2}|}}_{=F(L/2, L/2)} |x - \frac{L}{2}||y - \frac{L}{2}| \right. \\ \left. + \underbrace{\lim_{\substack{x \rightarrow -L/2 \\ y \rightarrow -L/2}} \frac{\rho_1^{SF}(x, y)}{|x + \frac{L}{2}||y + \frac{L}{2}|}}_{=F(-L/2, -L/2)} |x + \frac{L}{2}||y + \frac{L}{2}| \right], \quad (4.7)$$

where we have split $\rho_1(x, y)$ to emphasize on the two type of contribution. The $F(x_0, y_0)$ terms are constructed such that they reduce to a constant and can be taken out of the integral. Thus, Equation (4.7) becomes

$$\frac{\mathcal{B}_N}{k^4} \underset{k \rightarrow \infty}{=} \frac{1}{2\pi} \left[F(+L/2, +L/2) \mathcal{B}_N^{+L/2}(-k) \mathcal{B}_N^{+L/2}(k) \right. \\ \left. + F(-L/2, -L/2) \mathcal{B}_N^{-L/2}(-k) \mathcal{B}_N^{-L/2}(k) \right], \quad (4.8)$$

where the integrals $\mathcal{B}_N^{z_0}(k)$ can be obtained via the Watson's lemma and reads

$$\mathcal{B}_N^{z_0}(k) \underset{k \rightarrow \infty}{=} \int_{-L/2}^{L/2} dz e^{-ikz} |z - z_0| \underset{k \rightarrow \infty}{=} \frac{1}{2} \mathcal{F}_1 \frac{e^{-ikz_0}}{k^2} = -\frac{e^{-ikz_0}}{k^2}. \quad (4.9)$$

The factor $1/2$ signifies that each term counts as half of a cusps. Indeed, in the Watson's lemma, the integration domain includes both sides of the singularities. As the non-analiticities are at the edges of the box, this domain inevitably passes only through one side, effectively halving the contribution. Hence,

$$\frac{\mathcal{B}_N}{k^4} \underset{k \rightarrow \infty}{=} \frac{1}{\pi} \frac{F(+L/2, +L/2)}{k^4}, \quad (4.10)$$

where we have used the symmetry of ρ_1 (i.e. $\rho_1^{SF}(x, x) = \rho_1^{SF}(-x, -x)$) to set $F(+L/2, +L/2) = F(-L/2, -L/2)$. Finally, the edges' constant contribution to \mathcal{K}_N^{SF} takes the ensuing form

$$\mathcal{B}_N = \frac{1}{\pi} \lim_{\substack{x \rightarrow +\frac{L}{2} \\ y \rightarrow +\frac{L}{2}}} \frac{\rho_1^{SF}(x, y)}{|x - \frac{L}{2}||y - \frac{L}{2}|} = \frac{N(N+1)(2N+1)}{3L^3} \pi. \quad (4.11)$$

Opposite edges contribution:

The idea for opposite edges' contribution is exactly the same. By isolating the second type of singularity of ρ_1 - present in the vicinity of $|x \pm L/2||y \mp L/2|$ - we can write the opposite edges contribution to \mathcal{K}_N as

$$\begin{aligned} \frac{\mathcal{A}_N \cos kL}{k^4} \underset{k \rightarrow \infty}{=} & \frac{1}{2\pi} \int_{-L/2}^{L/2} dx e^{ikx} \int_{-L/2}^{L/2} dy e^{-iky} \left[\underbrace{\lim_{\substack{x \rightarrow +\frac{L}{2} \\ y \rightarrow -\frac{L}{2}}} \frac{\rho_1^{SF}(x, y)}{|x - \frac{L}{2}||y + \frac{L}{2}|}}_{=F(+L/2, -L/2)} \right. \\ & \left. + \underbrace{\lim_{\substack{x \rightarrow -\frac{L}{2} \\ y \rightarrow +\frac{L}{2}}} \frac{\rho_1^{SF}(x, y)}{|x + \frac{L}{2}||y - \frac{L}{2}|}}_{=F(-L/2, +L/2)} \right]. \end{aligned} \quad (4.12)$$

Similarly to the same edge contribution, we have

$$\frac{\mathcal{A}_N \cos kL}{k^4} \underset{k \rightarrow \infty}{=} \frac{1}{2\pi} \left[F(+L/2, -L/2) \mathcal{B}_N^{+L/2}(-k) \mathcal{B}_N^{-L/2}(k) \right. \quad (4.13)$$

$$\left. + F(-L/2, +L/2) \mathcal{B}_N^{-L/2}(-k) \mathcal{B}_N^{+L/2}(k) \right]. \quad (4.14)$$

Using the expression of $\mathcal{B}^{z_0}(k)$ [Equation (4.9)], it follows

$$\begin{aligned} \frac{\mathcal{A}_N \cos kL}{k^4} \underset{k \rightarrow \infty}{=} & \frac{1}{2\pi} \left[F(+L/2, -L/2) \frac{e^{ikL/2}}{k^2} \frac{e^{ikL/2}}{k^2} + F(-L/2, +L/2) \frac{e^{-ikL/2}}{k^2} \frac{e^{-ikL/2}}{k^2} \right] \\ & \underset{k \rightarrow \infty}{=} \frac{1}{\pi} \frac{F(+L/2, -L/2)}{k^4} \cos kL. \end{aligned} \quad (4.15)$$

By comparison with the expected form of the algebraic decay [Equation (4.4)], we finally have

$$(-1)^{N+1} \mathcal{A}_N = \frac{1}{\pi} \lim_{x \rightarrow -\frac{L}{2}, y \rightarrow +\frac{L}{2}} \frac{\rho_1^{SF}(x, y)}{|x - \frac{L}{2}| |y + \frac{L}{2}|} = (-1)^{N+1} \frac{N(N+1)\pi}{L^3}. \quad (4.16)$$

We observe that the oscillating part is given by contributions of half cusps at opposite walls ($x \rightarrow \pm L/2, y \rightarrow \mp L/2$). At first sight, it could be seen as an effect of diffraction by the box. However, its interpretation is more subtle and will become clearer when we will consider the case of a general mixture.

As we could see from Equation (4.11) and (4.16), the computation of ρ_1 's straightforward limits directly gives the constant contribution of \mathcal{K}_N^{SF} . This important assertion holds for mixtures, as we will see later on.

As expected, we have found that the hard walls induce an algebraic decay of the momentum distribution of SF of the form

$$\mathcal{K}_N^{SF} = \mathcal{B}_N + (-1)^{N+1} \mathcal{A}_N \cos(kL), \quad (4.17)$$

with $\mathcal{A}_N = N(N+1)\pi/L^3$ and $\mathcal{B}_N = (2N+1)\mathcal{A}_N/3$. To roughly sum up the outcomes, the effect of a hard wall in $\pm L/2$ introduces a half cusp, with respect to the coordinates x and y , of the form $|x \mp L/2|$ and $|y \mp L/2|$. In contrast, the oscillating part is given by contributions of half cusps at opposite walls ($x \rightarrow \pm L/2, y \rightarrow \mp L/2$). To support our conclusions, we have computed numerically the momentum distribution of a spinless Fermi gas of $N = 4$ particles, and we have compared it with the asymptotic behavior given in Equation (4.4) (see Figure 4.1).

4.1.2 Tonks-Girardeau bosons

In order to calculate the asymptotic behavior of the momentum distribution for N TG bosons trapped in a box, we start from the expression as an expansion in terms of the spinless fermions n -body density matrices, as shown in Chapter 2

$$\rho_1^{TB}(x, y) = \sum_{n=0}^{N-1} \frac{(-2)^n}{n!} \int_x^y \cdots \int_x^y dx_{n+1} \rho_{n+1}^{SF}(x, x_2, \dots, x_{n+1}, y, x_2, \dots, x_{n+1}), \quad (4.18)$$

for $x < y$. In the presence of smooth trapping potentials, we have already seen [Chapter 2] that only the $n = 1$ term of the series contributes to the contact. For TG in a box, we can individuate three different contributions to the momentum distribution's $1/k^4$ tail. The first contribution comes from $\rho_1^{SF}(x, y)$ and gives the terms in Equation (4.4). This contribution is similar to the result found in [Bouchoule & Dubail, 2021] showing that the discrepancy between \mathcal{K}_N and \mathcal{C}_N in a Lieb-Liniger gas with losses is due to the contribution of the rapidities. The second contribution comes from $-2 \int_x^y dx_2 \rho_2^{SF}(x, x_2; y, x_2)$ (the $n = 1$ term of Equation (4.18)) and gives the usual Tan's contact \mathcal{C}_N [Equation (2.49)], connected to the short-distance two-body correlations. Thus, for N TG bosons in a box, we obtain (see Appendix C)

$$\mathcal{C}_N^{TG} = \frac{N(N^2 - 1)(2N + 1)}{3L^3} \pi = (N - 1)\mathcal{B}_N. \quad (4.19)$$

Indeed, the two half cusps in $(+L/2, +L/2)$ and $(-L/2, -L/2)$ contribute to \mathcal{B}_N equivalently as the $(N - 1)$ other interparticles TG cusps \mathcal{C}_N^{TG} .

Remarkably, there is a third, non-local contribution entering the momentum distribution tail, which can be derived by integrating *all* the higher-order fermionic density matrices of the second term in Equation (4.18) over *all* the system. Indeed, it can be shown that (see Appendix C)

$$\begin{aligned} & \lim_{\substack{x \rightarrow -\frac{L}{2} \\ y \rightarrow \frac{L}{2}}} \sum_{j=1}^{N-1} \frac{(-2)^j}{j!} \prod_{\ell=2}^{j+1} \int_x^y dx_\ell \rho_{j+1}^{SF}(x, x_2, \dots; y, x_2, \dots) \\ & = -2\rho_1^{SF}(x, y)|_{x \sim -\frac{L}{2}, y \sim \frac{L}{2}}, \end{aligned} \quad (4.20)$$

if N is even and 0 otherwise. Such a term changes the sign of the oscillating part, with respect to the fermionic case *if the number of particles is even*. This means that for the TG gas, the sign of the oscillating part does not depend on the number of trapped bosons. Ultimately, we find that the asymptotic behavior of the momentum distribution for N TG bosons in the box can be written as

$$\begin{aligned} \mathcal{K}_N^{TG} &= \mathcal{C}_N^{TG} + \mathcal{B}_N + \mathcal{A}_N \cos(kL) \\ &= \frac{N}{N-1} \mathcal{C}_N^{TG} + \mathcal{A}_N \cos(kL). \end{aligned} \quad (4.21)$$

The average effect of the border (\mathcal{B}_N) is equivalent to adding a boson to the system. Moreover, it induces oscillations of the same amplitude as for a spinless Fermi gas but with a phase that does not depend on the particle number parity. In order to elucidate this result, we plot in the inset of Figure 4.1 the comparison between Equation (4.21) and the numerical calculation of \mathcal{K}_N for the case of $N = 4$ particles. Notice that, in the thermodynamic limit, we recover the known result for the contact density \mathcal{C}_N^{TG}/L of a homogeneous TG gas with density $n = N/L$: $\lim_{N,L \rightarrow \infty} \mathcal{K}_N^{TG}/L = \lim_{N,L \rightarrow \infty} \mathcal{C}_N^{TG}/L = \frac{2}{3}n^4\pi$ [Decamp et al., 2017].

4.2 Large- k tail of the momentum distribution in the box for spin mixtures

The aim of this section is to generalize our results to strongly interacting bosonic and fermionic mixtures. We will begin by presenting some generalities about spin mixtures. Afterward, we will calculate the weight of the large- k tail of the momentum distribution for spin mixtures $\mathcal{K}_N^{\text{mix}}$. Once obtained, we will examine the valuable information carried by this quantity and how it can be used experimentally.

4.2.1 Generalities about spin mixtures

We consider a 1D mixture of N particles with κ components and interacting via a two-body contact interaction. As a reminder, the Hamiltonian for this system presented in Chapter 3 reads

$$\hat{H} = \sum_{\sigma, \sigma'}^{\kappa} \sum_i^{N_{\sigma}} \left[-\frac{\hbar^2}{2m} \frac{\partial^2}{\partial x_{i, \sigma}^2} + g_{\sigma \sigma'} \sum_{j>i}^{N_{\sigma'}} \delta(x_{i, \sigma} - x_{j, \sigma'}) \right], \quad (4.22)$$

and its ansatz solution in the limit of infinite inter- and intra-species interaction strength $g_{\sigma \sigma'}$ and $g_{\sigma \sigma}$ takes the form [Volosniev et al., 2014, Deuretzbacher et al., 2014]

$$\Psi(X) = \sum_{P \in S_N} a_P \theta_P(X) \Psi_{SF}(X), \quad (4.23)$$

where $i, j \in [1, N]$ and $\sigma, \sigma' \in [1, \kappa]$ are the particle and spin indices, and $X = (x_{1, \sigma_1}, \dots, x_{N, \sigma_N})$ collects these indices. The index P indicates a permutation inside the permutation group of N elements, S_N , $\theta_P(X)$ is the generalized Heaviside function, which is equal to 1 in the coordinate sector $x_{P(1), \sigma_{P(1)}} < \dots < x_{P(N), \sigma_{P(N)}}$ and 0 elsewhere, and Ψ_{SF} is the wave function for N spinless fermions.

For a multi-component system, the first-order correlation function can be written as

$$\rho_1(x, y) = \sum_{\sigma} N_{\sigma} \rho_{1, \sigma}(x, y), \quad (4.24)$$

with

$$\rho_{1, \sigma}(x, y) = \sum_{i, j=1}^N c_{\sigma}^{(i, j)} \rho^{(i, j)}(x, y), \quad (4.25)$$

where $\rho^{(i, j)}(x, y)$ and $c_{\sigma}^{(i, j)}$ are the spatial and spin parts calculated on the sector $x_{1, \sigma_1} < \dots < x_{i-1, \sigma_{i-1}} < x < x_{i+1, \sigma_{i+1}} < \dots < x_{j, \sigma_j} < y < x_{j+1, \sigma_{j+1}} < \dots < x_{N, \sigma_N}$ [Deuretzbacher et al., 2016]. In particular,

$$c_{\sigma}^{(i, j)} = \delta_{\sigma_i}^{\sigma} \sum_{P \in S_N} a_P a_{P_{i \rightarrow j}}, \quad (4.26)$$

where $\delta_{\sigma_i}^{\sigma}$ selects only the sites with spin $\sigma_i = \sigma$ and $a_{P_{i \rightarrow j}}$ is the sector coefficient obtained by starting from the spin configuration labeled as a_P and applying a cyclic permutation which takes the i -th element into the j -th position, and vice versa.

4.2.2 Derivation of \mathcal{K}_N

To derive the equivalent of Equation (4.4) and (4.21) for mixtures, we now consider $\rho^{(i, j)}(x, y)$, which is defined for $x < y$ as [Deuretzbacher et al., 2016]

$$\rho^{(i,j)}(x,y) = \theta(x,y)N! \int_{x_2 < \dots < x_i < x < x_{i+1} < \dots < x_j < y < x_{j+1} < \dots < x_N} dx_2 \dots dx_N \times \Psi_{SF}^*(x, x_2, \dots, x_N) \Psi_{SF}(y, x_2, \dots, x_N). \quad (4.27)$$

where we have used the product identity

$$\Psi_{SF}^*(x_1, \dots, x_{i-1}, x, x_{i+1}, \dots, x_N) \Psi_{SF}(x_1, \dots, x_{i-1}, y, x_{i+1}, \dots, x_N) = \Psi_{SF}^*(x, x_2, \dots, x_N) \Psi_{SF}(y, x_2, \dots, x_N), \quad (4.28)$$

to move x and y from x_i to x_1 . For completeness, the $y < x$ part of Equation (4.27) can be obtained using the symmetry relation $\rho^{(i,j)}(x,y) = \rho^{(j,i)}(y,x)$. For hard-core particles in a box of length L , we can rewrite Equation (4.27) as

$$\rho^{(i,j)}(x,y) = \frac{\theta(x,y)N!}{(i-1)!(j-i)!(N-j)!} \int_{-L/2}^x dx_2 \dots dx_i \int_x^y dx_{i+1} \dots dx_j \times \int_y^{L/2} dx_{j+1} \dots dx_N \Psi_{SF}^*(x, x_2, \dots, x_N) \Psi_{SF}(y, x_2, \dots, x_N). \quad (4.29)$$

As presented in Chapter 1, in presence of DBC, the fully anti-symmetric wave function Ψ_{SF} reads

$$\Psi_{SF} = \frac{1}{\sqrt{N!}} \det [\phi_m(x_n)], \quad (4.30)$$

where $\phi_m(x_n) = \sqrt{2/L} \sin[k_m(x_n + L/2)]$ are natural orbitals of the box, with $k_m = m\pi/L$, for $x_n \in [-L/2, L/2]$ and $n, m \in \{1, \dots, N\}$. Following [Deuretzbacher et al., 2016, Decamp et al., 2016a, Decamp et al., 2017], we use the Leibniz formula for a determinant such that $\Psi_{SF} = (1/\sqrt{N!}) \sum_{P \in S_N} \epsilon(P) \prod_{i=1}^N \phi_{P(i)}(x_i)$, where $\epsilon(P)$ is the signature of the permutation P , to express Equation (4.29) as

$$\rho^{(i,j)}(x,y) = \frac{1}{(i-1)!(j-i)!(N-j)!} \theta(x,y) \sum_{P,Q \in S_N} \epsilon(P,Q) \phi_{P(1)}(x) \phi_{Q(1)}(y) \times \prod_{k=2}^N \int_{L_{ij}(k)}^{U_{ij}(k)} \phi_{P(k)}(z) \phi_{Q(k)}(z), \quad (4.31)$$

where $\epsilon(P,Q) = \epsilon(P)\epsilon(Q)$, and the integration intervals are defined as

$$(L_{ij}(k), U_{ij}(k)) = \begin{cases} (y, L/2) & \text{if } j \leq k, \\ (x, y) & \text{if } i \leq k < j, \\ (-L/2, x) & \text{if } k < i. \end{cases} \quad (4.32)$$

We then define, for convenience

$$X_{p,q}(x, y) = \phi_p(x)\phi_q(y), \quad (4.33)$$

$$A_{p,q}(z) = \int_z^{L/2} du \phi_p(u)\phi_q(u) \quad (4.34)$$

$$= \frac{\sin\left(\frac{\pi}{2L}(p+q)(2z+L)\right)}{\pi(p+q)} - \frac{\sin\left(\frac{\pi}{2L}(p-q)(2z+L)\right)}{\pi(p-q)}, \quad (4.35)$$

and rewrite Equation (4.31) as follows:

$$\begin{aligned} \rho^{(i,j)}(x, y) &= \frac{1}{(i-1)!(j-i)!(N-j)!} \theta(x, y) \sum_{P, Q \in S_N} \epsilon(P, Q) X_{P(1), Q(1)}(x, y) \\ &\times \prod_{k=2}^i (\delta_{P(k), Q(k)} - A_{P(k), Q(k)}(x)) \prod_{l=i+1}^j (A_{P(l), Q(l)}(x) - A_{P(l), Q(l)}(y)) \prod_{m=j+1}^N A_{P(m), Q(m)}(y), \end{aligned} \quad (4.36)$$

where we have used that the integrals in the three intervals defined in Equation (4.32) can be written all in terms of $A_{p,q}(z)$. Equation (4.36) represents the starting point of the derivation of every term of the large- k tail of the momentum distribution for spin mixtures. As for identical particles, we expect three types of contribution: 1) a first constant part related to the usual contact, 2) a second constant part induced by same walls, and 3) an oscillatory part generated by opposite walls. Seeking clarity, we will consider each contribution separately in the following paragraphs.

The Tan's contact term:

The Tan's contact term does not depend on the finite size of the system and can be derived by standard methods (see, for example, [Decamp et al., 2016b, Aupetit-Diallo et al., 2022]). For completeness, here we give a few details of the derivation. One can start from the Tan's relation

$$\mathcal{C}_N^{\text{mix}} = -\frac{m^2}{\pi \hbar^4} \frac{\partial E}{\partial(1/g)} \Big|_{g \rightarrow \infty} = \frac{S \alpha_N}{\pi}, \quad (4.37)$$

where the total energy for the mixture in the limit $g \rightarrow \infty$ can be written as $E \simeq E_F - m^2 S \alpha_N / (\hbar^4 g)$ with [Appendix A]

$$\alpha_N = \frac{N(N+1)(2N+1)\pi^2}{6L^3}, \quad (4.38)$$

and

$$S = \sum_P \sum_{i=1}^{N-1} \left[\frac{1}{4} (a_P - a_{P_{i,i+1}})^2 (1 - \delta_{\sigma_i}^{\sigma_{i+1}}) + \eta_B a_P a_{P_{i,i+1}} \delta_{\sigma_i}^{\sigma_{i+1}} \right], \quad (4.39)$$

with η_B is equal to 1 for bosons and 0 for fermions. S is a pondered counting of the system's possible symmetric exchanges. For instance, if we consider a gas of N TB, every exchange will be fully symmetric and contribute with a weight of one to S . In contrast, a not fully symmetric exchange, generated between particles of different

spins, for instance, will contribute with a lower weight, while a fully anti-symmetric state will not contribute at all. It means that for TB or the ground state of a $SU(\kappa)$ mixture, we have $S = N$ in the presence of PBC and $S = N - 1$ for DBC, while $S = 0$ for SF in any geometry. One then notices that $\alpha_N = \mathcal{B}_N \pi/2$ and, using that $\mathcal{C}_N^{TG} = (N - 1)\mathcal{B}_N$ [Equation (4.19)], one can collect the two constant terms as

$$\mathcal{C}_N^{\text{mix}} + \mathcal{B}_N = \frac{S}{N - 1} \mathcal{C}_N^{TG} + \frac{\mathcal{C}_N^{TG}}{(N - 1)} = \frac{S + 1}{N - 1} \mathcal{C}_N^{TG}. \quad (4.40)$$

The constant hard wall induced term:

Following the method used for SF, we first evaluate Equation (4.36) in the limit $(x, y) \rightarrow (\pm L/2, \pm L/2)$. To do so, we first notice that

$$\lim_{\substack{x \rightarrow -\frac{L}{2} \\ y \rightarrow -\frac{L}{2}}} X_{p,q}(x, y) = \frac{2\pi^2}{L^3} pq \left(x + \frac{L}{2}\right) \left(y + \frac{L}{2}\right), \quad (4.41)$$

$$\lim_{z \rightarrow -\frac{L}{2}} A_{p,q}(z) = \delta_{p,q}, \quad \text{and} \quad \lim_{z \rightarrow \frac{L}{2}} A_{p,q}(z) = 0 \quad \forall p, q. \quad (4.42)$$

Therefore, the only non-zero terms in Equation (4.36) correspond to $i = j = 1$ for the case $(x, y) \rightarrow -L/2$ and $i = j = N$ for the case $(x, y) \rightarrow L/2$. Using Equation (4.25), we can write

$$\begin{aligned} \mathcal{B}_N &= \frac{1}{2\pi} \left(\lim_{\substack{x \rightarrow -\frac{L}{2} \\ y \rightarrow -\frac{L}{2}}} \frac{\rho^{(1,1)}(x, y)}{|x + \frac{L}{2}| |y + \frac{L}{2}|} \sum_{\sigma} N_{\sigma} c_{\sigma}^{(1,1)} + \lim_{\substack{x \rightarrow +\frac{L}{2} \\ y \rightarrow +\frac{L}{2}}} \frac{\rho^{(N,N)}(x, y)}{|x - \frac{L}{2}| |y - \frac{L}{2}|} \sum_{\sigma} N_{\sigma} c_{\sigma}^{(N,N)} \right) \\ &= \frac{N}{\pi} \lim_{\substack{x \rightarrow -\frac{L}{2} \\ y \rightarrow -\frac{L}{2}}} \frac{\rho^{(1,1)}(x, y)}{|x + \frac{L}{2}| |y + \frac{L}{2}|}, \end{aligned} \quad (4.43)$$

where we have used that $\rho^{(1,1)}(x, y)|_{(x,y) \rightarrow (-\frac{L}{2}, -\frac{L}{2})} = \rho^{(N,N)}(x, y)|_{(x,y) \rightarrow (\frac{L}{2}, \frac{L}{2})}$ and $N = \sum_{\sigma} N_{\sigma} c_{\sigma}^{(i,i)} = \sum_{\sigma} N_{\sigma} \forall i$, and

$$\rho^{(1,1)}(x, y) = \frac{1}{(N - 1)!} \theta(x, y) \sum_{P, Q \in S_N} \epsilon(P, Q) X_{P(1), Q(1)}(x, y) \prod_{k=2}^N A_{P(k), Q(k)}(y). \quad (4.44)$$

Using Equations (4.41) and (4.42), we can replace $A_{P(k), Q(k)}(y)$ with $\delta_{P(k), Q(k)}$ and obtain

$$\begin{aligned}
\lim_{\substack{x \rightarrow -\frac{L}{2} \\ y \rightarrow -\frac{L}{2}}} \frac{\rho^{(1,1)}(x, y)}{|x + \frac{L}{2}| |y + \frac{L}{2}|} &= \frac{1}{(N-1)!} \frac{2\pi^2}{L^3} \sum_{P \in S_N} P(1)^2 \\
&= \frac{(N-1)!}{N(N-1)!} \frac{2\pi^2}{L^3} \sum_{n=1}^N n^2 \\
&= \frac{(N+1)(2N+1)}{3L^3} \pi^2.
\end{aligned} \tag{4.45}$$

Finally, by inserting Equation (4.45) in Equation (4.43), we find

$$\mathcal{B}_N = \frac{N(N+1)(2N+1)}{3L^3} \pi, \tag{4.46}$$

which is exactly Equation (4.11). Therefore, we have shown how to derive Equation (4.11) by starting from this more general problem.

The oscillating term:

We now evaluate the amplitude of the oscillation in Equation (4.43). As discussed for SF, this derives from the contribution at the borders of the trap, namely, by taking the limit $(x, y) \rightarrow (\mp L/2, \pm L/2)$. To do so, we first notice that

$$\lim_{\substack{x \rightarrow -\frac{L}{2} \\ y \rightarrow \frac{L}{2}}} X_{p,q}(x, y) = \frac{2\pi^2}{L^3} (-1)^q pq \left(x + \frac{1}{2}\right) \left(y - \frac{1}{2}\right), \tag{4.47}$$

$$\lim_{\substack{x \rightarrow -\frac{L}{2} \\ y \rightarrow \frac{L}{2}}} (A_{p,q}(x) - A_{p,q}(y)) = \delta_{p,q}. \tag{4.48}$$

Thanks to these limits and using the symmetries of $\rho^{(i,j)}(x, y)$, we see that the only non-zero terms in Equation (4.36) correspond to $(i, j) = (1, N)$ for $(x, y) \rightarrow (-L/2, L/2)$ and $(i, j) = (N, 1)$ for $(x, y) \rightarrow (L/2, -L/2)$. Following the SF process, we can define

$$\begin{aligned}
(-1)^{N+1} \mathcal{A}_N^{\text{mix}} &= \frac{1}{2\pi} \left(\lim_{\substack{x \rightarrow -\frac{L}{2} \\ y \rightarrow +\frac{L}{2}}} \frac{\rho^{(1,N)}(x, y)}{|x + \frac{L}{2}| |y - \frac{L}{2}|} \sum_{\sigma} N_{\sigma} c_{\sigma}^{(1,N)} \right. \\
&\quad \left. + \lim_{\substack{x \rightarrow +\frac{L}{2} \\ y \rightarrow -\frac{L}{2}}} \frac{\rho^{(N,1)}(x, y)}{|x - \frac{L}{2}| |y + \frac{L}{2}|} \sum_{\sigma} N_{\sigma} c_{\sigma}^{(N,1)} \right) \\
&= \frac{1}{\pi} \left(\lim_{\substack{x \rightarrow -\frac{L}{2} \\ y \rightarrow +\frac{L}{2}}} \frac{\rho^{(1,N)}(x, y)}{|x + \frac{L}{2}| |y - \frac{L}{2}|} \right) \sum_{\sigma} N_{\sigma} c_{\sigma}^{(1,N)},
\end{aligned} \tag{4.49}$$

where we have used the symmetry properties $c_{\sigma}^{(1,N)} = c_{\sigma}^{(N,1)}$ and $\rho^{(1,N)}(x, y) = \rho^{(N,1)}(y, x)$ and that

$$\rho^{(1,N)}(x, y) = \frac{1}{(N-1)!} \sum_{P, Q \in S_N} \epsilon(P, Q) X_{P(1), Q(1)}(x, y) \prod_{l=2}^N (A_{P(l), Q(l)}(x) - A_{P(l), Q(l)}(y)). \quad (4.50)$$

Using Equation (4.47), (4.48) and (4.42), we can therefore replace the difference $A_{p,q}(x) - A_{p,q}(y)$ with a $\delta_{p,q}$, which corresponds to have $P = Q$, and obtain

$$\begin{aligned} \lim_{\substack{x \rightarrow -\frac{L}{2} \\ y \rightarrow \frac{L}{2}}} \frac{\rho^{(1,N)}(x, y)}{|x + \frac{L}{2}| |y - \frac{L}{2}|} &= \frac{1}{(N-1)!} \frac{2\pi^2}{L^3} \sum_{P \in S_N} (-1)^{P(1)} P(1)^2 \\ &= \frac{2\pi^2}{L^3} \frac{(N-1)!}{N(N-1)!} \sum_{n=1}^N (-1)^n n^2 \\ &= \frac{\pi^2}{L^3} (-1)^{N+1} (N+1). \end{aligned} \quad (4.51)$$

Finally, we find a more general definition of the amplitude of the oscillation, namely,

$$(-1)^{N+1} \mathcal{A}_N^{\text{mix}} = (-1)^{N+1} \mathcal{A}_N \sum_{\sigma} \frac{N_{\sigma}}{N} c_{\sigma}^{(1,N)}, \quad (4.52)$$

which is consistent with Equation (4.16) and takes into account the presence (resp. absence) of the factor $(-1)^{N+1}$ for fermions (resp. bosons).

4.2.3 Investigation on \mathcal{K}_N for a mixture

By gathering Equation (4.37), (4.46), and (4.49), we find that the asymptotic behavior of the momentum distribution in the case of spin mixtures assumes the form

$$\begin{aligned} \mathcal{K}_N^{\text{mix}} &= \mathcal{C}_N^{\text{mix}} + \mathcal{B}_N + (-1)^{N+1} \mathcal{A}_N \sum_{\sigma} \frac{N_{\sigma}}{N} c_{\sigma}^{(1,N)} \cos(kL) \\ &= \frac{S+1}{N-1} \mathcal{C}_N^{\text{TG}} + (-1)^{N+1} \mathcal{A}_N \sum_{\sigma} \frac{N_{\sigma}}{N} c_{\sigma}^{(1,N)} \cos(kL), \end{aligned} \quad (4.53)$$

With the quantity

$$S = \sum_P \sum_{i=1}^{N-1} \left[\frac{1}{4} (a_P - a_{P_{i,i+1}})^2 (1 - \delta_{\sigma_i}^{\sigma_{i+1}}) + \eta_B a_P a_{P_{i,i+1}} \delta_{\sigma_i}^{\sigma_{i+1}} \right] \quad (4.54)$$

taking into account the number of symmetric exchanges between particles [Aupetit-Diallo et al., 2022] and is proportional to the eigenvalue of the rescaled Voloniev matrix $V' = V/\alpha_N$ [see Equation (3.29)]. P runs over the snippets, and η_B equals 1 for identical bosons and 0 otherwise. As expected, we can recover Equations (4.4) and (4.21) for the cases of spinless fermions and TG bosons, respectively. Indeed,

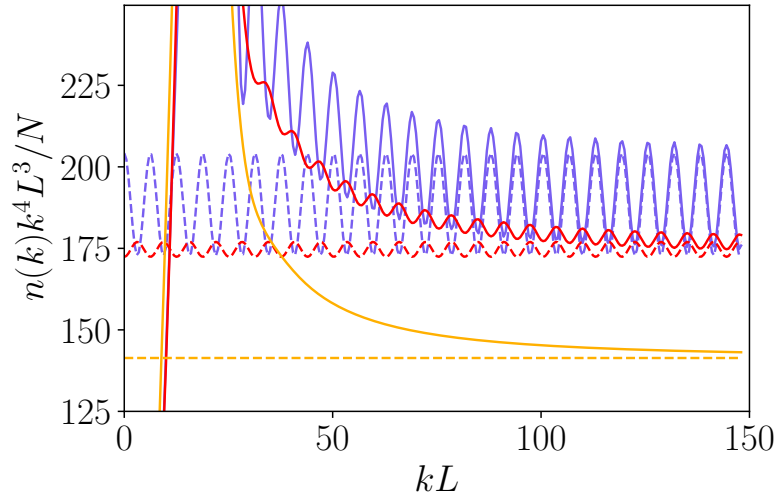


Figure 4.3: The solid lines stand for normalized momentum distribution $n(k)/N$ multiplied by k^4 , in units of L^3 , for the case of $2 + 2$ $SU(2)$ bosons 1) in the ground state (violet, upper curve), 2) in the first excited state (orange, central curve), and 3) in the third excited state (yellow, lower curve). The dashed lines stand for the analytical expression of $\mathcal{K}_N^{\text{mix}}/N$, Equation (4.53), evaluated for cases 1), 2), and 3) (same color code). Figure from [Aupetit-Diallo et al., 2023].

it can be shown that for spinless fermions $S = 0$ and $c_\sigma^{(1,N)} = 1$, and for a TG gas $S = N - 1$ and $\sum_\sigma \frac{N_\sigma}{N} c_\sigma^{(1,N)} = (-1)^{N+1}$. The following part of this section provides examples of $c_\sigma^{1,N}$ computation to exemplify the precedent result.

As for the one-component cases, the large- k tail of $n(k)$ is not given solely by the Tan's contact but includes two additional terms. The first - the k -independent contribution \mathcal{B}_N - does not depend on the type of particles or mixture and counts such as an extra symmetric exchange in the mixture. The second - the oscillating part - is more intriguing since the oscillations' amplitude remarkably depends on long-distance spin coherence. Indeed, the only term of Equation (2.24) that does not vanish in the limit $x \rightarrow -L/2$ and $y \rightarrow +L/2$ corresponds to the cyclic permutation $P_{1 \rightarrow N}$. Therefore, $c_\sigma^{(1,N)}$ can be interpreted as the one-body spin coherence through the whole system. Let us illustrate this statement with the explicit computation of some $c_\sigma^{(1,N)}$'s.

Example of $c_\sigma^{(1,N)}$ calculation

In this paragraph, we detail the construction of the quantity $c_\sigma^{(1,N)}$ for the case of a balanced mixture of $N = 4$ bosons with spin components $\sigma = \uparrow$ or \downarrow . As a reminder, the general one-spin correlations expression reads

$$c_\sigma^{(i,j)} = \delta_\sigma^{\sigma_i} \sum_{P \in S_N} a_P a_{P_{i \rightarrow j}}, \quad (4.55)$$

where $\delta_\sigma^{\sigma_i}$ selects only the sites with spin $\sigma_i = \sigma$ and $a_{P_{i \rightarrow j}}$ is the sector coefficient obtained by starting from the spin configuration related to a_P and applying a cyclic permutation, which takes the i -th into the j -th position, and vice versa.

Let us start considering the \uparrow spin-component. The a_P coefficients that are involved in the calculation of $c_{\uparrow}^{(1,4)}$ have been gathered in Table 4.1.

Table 4.1: Coefficients a_i corresponding to the different spin sectors P and $P_{1 \rightarrow 4}$ with the selection rule $\delta_{\uparrow, \sigma_1}$, for the case of a $2 + 2$ bosonic mixture.

Sector P $\delta_{\uparrow, \sigma_1}$	a_P	Sector $P_{1 \rightarrow 4}$ $\delta_{\uparrow, \sigma_1}$	$a_{P_{1 \rightarrow 4}}$
$x_{1, \uparrow} < x_{2, \uparrow} < x_{3, \downarrow} < x_{4, \downarrow}$	a_1	$x_{2, \uparrow} < x_{3, \downarrow} < x_{4, \downarrow} < x_{1, \uparrow}$	$-a_3$
$x_{1, \uparrow} < x_{2, \uparrow} < x_{4, \downarrow} < x_{3, \downarrow}$	$-a_1$	$x_{2, \uparrow} < x_{4, \downarrow} < x_{3, \downarrow} < x_{1, \uparrow}$	a_3
$x_{1, \uparrow} < x_{3, \downarrow} < x_{2, \uparrow} < x_{4, \downarrow}$	a_2	$x_{3, \downarrow} < x_{2, \uparrow} < x_{4, \downarrow} < x_{1, \uparrow}$	$-a_5$
$x_{1, \uparrow} < x_{4, \downarrow} < x_{2, \uparrow} < x_{3, \downarrow}$	$-a_2$	$x_{4, \downarrow} < x_{2, \uparrow} < x_{3, \downarrow} < x_{1, \uparrow}$	a_5
$x_{1, \uparrow} < x_{3, \downarrow} < x_{4, \downarrow} < x_{2, \uparrow}$	a_3	$x_{3, \downarrow} < x_{4, \downarrow} < x_{2, \uparrow} < x_{1, \uparrow}$	$-a_6$
$x_{1, \uparrow} < x_{4, \downarrow} < x_{3, \downarrow} < x_{2, \uparrow}$	$-a_3$	$x_{4, \downarrow} < x_{3, \downarrow} < x_{2, \uparrow} < x_{1, \uparrow}$	a_6

The coefficients $\{a_1, \dots, a_6\}$ in Table 4.1 are related to the sectors collected in the snippet basis $\{|\uparrow\uparrow\downarrow\downarrow\rangle, |\uparrow\downarrow\uparrow\downarrow\rangle, |\uparrow\downarrow\downarrow\uparrow\rangle, |\downarrow\uparrow\uparrow\downarrow\rangle, |\downarrow\uparrow\downarrow\uparrow\rangle, |\downarrow\downarrow\uparrow\uparrow\rangle\}$. Furthermore, because we use as a basis the anti-symmetric fermionic many-body wave function Ψ_{SF} , we have to include a minus sign if we switch two bosons (see, for instance, the first two rows of Table 4.1).

Using Equation (4.26), one obtains

$$c_{\uparrow}^{(1,4)} = -2a_1a_3 - 2a_2a_5 - 2a_3a_6. \quad (4.56)$$

Table 4.2: Coefficients a_i corresponding to the different spin sectors P and $P_{1 \rightarrow 4}$ with the selection rule $\delta_{\downarrow, \sigma_1}$, for the case of a $2 + 2$ bosonic mixture.

Sector P $\delta_{\downarrow, \sigma_1}$	a_P	Sector $P_{1 \rightarrow 4}$ $\delta_{\downarrow, \sigma_1}$	$a_{P_{1 \rightarrow 4}}$
$x_{3, \downarrow} < x_{1, \uparrow} < x_{2, \uparrow} < x_{4, \downarrow}$	a_4	$x_{1, \uparrow} < x_{2, \uparrow} < x_{4, \downarrow} < x_{3, \downarrow}$	$-a_1$
$x_{3, \downarrow} < x_{2, \uparrow} < x_{1, \uparrow} < x_{4, \downarrow}$	$-a_4$	$x_{2, \uparrow} < x_{1, \uparrow} < x_{4, \downarrow} < x_{3, \downarrow}$	a_1
$x_{3, \downarrow} < x_{1, \uparrow} < x_{4, \downarrow} < x_{2, \uparrow}$	a_5	$x_{1, \uparrow} < x_{4, \downarrow} < x_{2, \uparrow} < x_{3, \downarrow}$	$-a_2$
$x_{3, \downarrow} < x_{2, \uparrow} < x_{4, \downarrow} < x_{1, \uparrow}$	$-a_5$	$x_{2, \uparrow} < x_{4, \downarrow} < x_{1, \uparrow} < x_{3, \downarrow}$	a_2
$x_{3, \downarrow} < x_{4, \downarrow} < x_{1, \uparrow} < x_{2, \uparrow}$	a_6	$x_{4, \downarrow} < x_{1, \uparrow} < x_{2, \uparrow} < x_{3, \downarrow}$	$-a_4$
$x_{3, \downarrow} < x_{4, \downarrow} < x_{2, \uparrow} < x_{1, \uparrow}$	$-a_6$	$x_{4, \downarrow} < x_{2, \uparrow} < x_{1, \uparrow} < x_{3, \downarrow}$	a_4

Analogously, using Table 4.2, one can show that

$$c_{\downarrow}^{1,4} = -2a_4a_1 - 2a_5a_2 - 2a_6a_4. \quad (4.57)$$

In order to streamline our understanding of the oscillations of $\mathcal{K}_N^{\text{mix}}$, we must establish a definition for the cosine of its phase,

$$\Phi_N^{\text{mix}} = (-1)^{N+1} \sum_{\sigma} \frac{N_{\sigma}}{N} c_{\sigma}^{(1,N)} = (-1)^{N+1} \frac{\mathcal{A}_N^{\text{mix}}}{\mathcal{A}_N}, \quad (4.58)$$

where $\mathcal{A}_N^{\text{mix}}$ is defined in Equation (4.52). For the mixture of $2 + 2$ bosons, Equation (4.58) becomes

$$\Phi_4^{2+2} = a_1a_3 + a_1a_4 + 2a_2a_5 + a_2a_6 + a_3a_6. \quad (4.59)$$

Due to the specific permutation rule present in $c_\sigma^{(1,N)}$, Equation (4.59) clearly involves only certain products of $a_i a_j$ with $i \neq j$. This means that, for example, there is no possibility to connect the snippet $|\uparrow\downarrow\downarrow\uparrow\rangle$ corresponding to the coefficients $\pm a_3$ to the snippet $|\downarrow\uparrow\uparrow\downarrow\rangle$ corresponding to the coefficients $\pm a_4$. This justifies the fact that the third excited state of the $SU(2)$ 2 + 2 bosonic mixture [see Figure 4.3] shows no oscillations in the tails of the momentum distribution. Indeed, the spin part of the many-body wave function for this state is given by $|\uparrow\downarrow\downarrow\uparrow\rangle - |\downarrow\uparrow\uparrow\downarrow\rangle$ (up to a normalization factor) and, consequently, Φ_4^{2+2} is zero.

It appears that Φ_N^{mix} is a preferential quantity in this analysis. Indeed, through the $c_\sigma^{(1,N)}$'s, it carries important information about the spin state of the system. To better understand the behavior of Φ_N^{mix} , we will calculate it for all the states in the ground state manifold of various $SU(2)$ mixtures. Our aim being to show how Φ_N^{mix} can be utilized to deduce the system's state.

4.2.4 Φ_N^{mix} as a ground state probe

The quantity Φ_N^{mix} depends on the number of particles N , the type of mixture, and the system state (ground-state or excited states). Indeed, it can be positive or negative, with a magnitude between 0 and 1. This is shown in Table 4.3, where we have gathered the values of Φ_N^{mix} for the case of $SU(2)$ bosonic and fermionic mixtures for a different number of total particles and particles per component.

From 4.3, we see that Φ_N^{mix} varied a lot from a mixture, or one excited state, to another. Moreover, no particular pattern seems to emerge apart from the ground and most excited state. In those, the value of Φ_N^{mix} can be predicted exactly. Remarkably, this property of spin mixture can be used experimentally to infer the system's state.

In typical UCAG experimental setups, we have seen that the momentum distribution is obtained by switching off the trapping potential and imaging the cloud after a ballistic expansion [Paredes et al., 2004, Pagano et al., 2014]. These measurements are obtained by averaging over system realizations where particles fluctuate from shot to shot. As a consequence, the probed Φ_N^{mix} will cancel out if the values fluctuate between prepared states. Fortunately, a state presents the same Φ_N^{mix} independently of the prepared state: the ground state for bosonic mixtures. Indeed, we can observe, Table 4.3, that for the ground state of $SU(2)$ bosonic mixtures, $\Phi_N^{SU(2)}$ is equal to 1, $\forall N$. Thus, we state that the measured amplitude oscillations $\langle \Phi_N^{\text{mix}} \mathcal{A}_N \rangle$ will generally vanish except if the system is a $SU(2)$ bosonic mixture and is prepared mostly in the ground state. This conclusion can be generalized to the case of $SU(\kappa)$ bosons, $\forall \kappa$, but does not hold if the $SU(\kappa)$ symmetry is broken or for other types of mixtures. Therefore, the observation of oscillating tails in $n(k)$ of $SU(\kappa)$ bosonic mixtures could be used to determine whether the system is mainly cooled down in its ground state or not. This ability is of particular interest as identifying the exact populated state might be experimentally difficult since the spectrum of a strongly interacting mixture is characterized by the presence of a large number of states very close in energy to the ground state [Deuretzbacher et al., 2008, Decamp et al., 2016b].

Table 4.3: Cosine of $\mathcal{K}_N^{\text{mix}}$'s phase Φ_N^{mix} (Equation (4.58)) as a function of spin excitation state for the case of $SU(2)$ bosonic mixtures (central columns) and fermionic mixtures (right columns) with $1+4$, $2+2$, $2+3$, and $3+3$ particles. “GS” stands for Ground State and “MS” for the Most excited State of the lowest energy manifold.

Excitation level	$1B+4B$	$2B+2B$	$2B+3B$	$3B+3B$	$1F+4F$	$2F+2F$	$2F+3F$	$3F+3F$
GS	1	1	1	1	-0.81	-0.87	0.33	0.78
1	0.09	-0.15	0.08	0.24	-0.6	0.85	0.28	-0.74
2	0.31	-0.87	-0.6	-0.37	0.31	0	-0.81	0.18
3	-0.59	0	0.31	-0.81	0.09	0.87	0.76	-0.77
4	-	-0.85	-0.78	0.5	-	0.15	-0.58	-0.2
5	-	-	-0.58	-0.47	-	-	-0.78	-0.07
6	-	-	0.76	-0.78	-	-	0.31	-0.5
7	-	-	-0.81	-0.33	-	-	-0.6	0.91
8	-	-	0.28	0.63	-	-	0.09	-0.15
9	-	-	-	0.32	-	-	-	0.5
10	-	-	-	-0.5	-	-	-	-0.32
11	-	-	-	0.15	-	-	-	-0.63
12	-	-	-	-0.91	-	-	-	0.33
13	-	-	-	0.5	-	-	-	0.78
14	-	-	-	0.07	-	-	-	0.47
15	-	-	-	0.2	-	-	-	-0.5
16	-	-	-	0.77	-	-	-	0.81
17	-	-	-	-0.18	-	-	-	0.37
18	-	-	-	0.74	-	-	-	-0.24
MS	-0.81	0.87	0.33	-0.78	1	-1	1	-1

4.2.5 Concluding remarks

In conclusion, we have shown that the presence of a hard wall trapping potential breaks down the Tan's relation connecting the $1/k^4$ decay of the momentum distribution of a 1D gas characterized by repulsive contact interactions to the adiabatic derivative of the energy with respect to the inverse of the interaction strength. This result remains valid even if the system is at equilibrium. In the strongly interacting limit, the presence of the two hard walls has a double effect. The first is rather trivial: it mimics the presence of an additional boson or impurity in the system. The second is more subtle: the tails develop oscillations whose *amplitude depends on the non-local spin coherence over the whole system size*. The sign of this contribution depends generally on the number of particles, except for the ground state of a bosonic $SU(\kappa)$ mixture. Ultimately, we have demonstrated that this remarkable feature can be used as a ground-state probe for bosonic spin mixtures.

To pursue this investigation, we have undertaken in our group (mainly by Silvia Musolino) the analysis of the dynamic behavior of these interesting outcomes. In the same idea, we aim to generalize our findings to scenarios where the trap has other types of discontinuities and explore any new contributions and applications that may arise.

Chapter 5

Symmetry analysis

In this chapter, we will detail the outcomes related to the $SU(\kappa)$ symmetry analysis obtained in the context of this thesis. We will heavily rely on the notion introduced in Chapter 3. To start off, we will examine a scenario that breaks this symmetry [Aupetit-Diallo et al., 2022]. By slightly detuning one interaction strength compared to the others, the $SU(\kappa)$ symmetry no longer holds, whereas the system's Hamiltonian remarkably remains integrable. Following this scheme, new states can be engineered. Moreover, these solutions are obtained exactly, which enables a rigorous symmetry analysis of a $SU(\kappa)$ Symmetry Breaking (SB) system. Since this system has not yet been explored, we will also thoroughly characterize its long- and short-distance correlation properties. Although the symmetry is weakly broken, we will show that it has important consequences on spin coherence in the system. In a second time, we will consider spin mixtures with an additional artificial gauge field induced by a rotating system [Pecci et al., 2023]. Again, the corresponding model is integrable. After developing a method to compute the solutions, we will demonstrate that the $SU(\kappa)$ symmetry analysis allows a deeper understanding of the system and could open setups to constrain the symmetry state of a spin mixture.

5.1 Exact solution for $SU(2)$ symmetry breaking of bosonic mixtures at strong interactions

This section is dedicated to the study of the equilibrium properties of a 1D mixture of two Tonks-Girardeau gases on a ring geometry in the limit of strongly repulsive inter-species interactions. The discussion is organized as follows. We will first present the model and discuss in detail our procedure to obtain the ground-state many-body wave function for the $SU(2)$ Hamiltonian as for the SB one. Then, we will quantify the breaking of the symmetry associated with the SB many-body ground-state by calculating the expectation value of the 2-cycle-sum operator [Katriel, 1993, Fang et al., 2011, Decamp et al., 2016a, Decamp et al., 2016b]. We will show that for a large number of particles, the SB state is halfway between the most symmetric and the most anti-symmetric states allowed by the $SU(2)$ Hamiltonian. Afterward, we will calculate the momentum distribution given by the Fourier transform of the one-body density matrix. In particular, we will study the zero-mode occupation

number and the Tan's contact. Finally, some remarks on the relation between our approach and the Bethe ansatz solution will conclude the analysis.

5.1.1 The model

We consider a balanced two-component 1D Bose gas in a ring geometry characterized by contact interactions. The general Hamiltonian for N bosons reads

$$\hat{H} = \sum_{\sigma=\uparrow,\downarrow} \sum_i^{N_\sigma} \left[-\frac{\hbar^2}{2m} \frac{\partial^2}{\partial x_{i,\sigma}^2} + g_{\sigma\sigma} \sum_{j>i}^{N_\sigma} \delta(x_{i,\sigma} - x_{j,\sigma}) \right] + g_{\uparrow\downarrow} \sum_i^{N_\uparrow} \sum_j^{N_\downarrow} \delta(x_{i,\uparrow} - x_{j,\downarrow}), \quad (5.1)$$

with $g_{\uparrow\downarrow}$ the inter-species, $g_{\uparrow\uparrow}$ ($g_{\downarrow\downarrow}$) the intra-species interaction strengths and $N_\downarrow = N_\uparrow = N/2$ the number of particles per component. The aim of this work is to analyze the ground-state correlation properties of the symmetry breaking case with $g_{\uparrow\uparrow} = g_{\downarrow\downarrow} \neq g_{\uparrow\downarrow}$ in comparison to the $SU(2)$ case with $g_{\uparrow\uparrow} = g_{\downarrow\downarrow} = g_{\uparrow\downarrow}$.

General solution in the strongly interacting limit

In this introductory part, we recall the general solution of the Hamiltonian Equation (5.1) as well as the Volosniev matrix developed to solve the model fully. All the details of the method to get these results and examples of solving have been provided in Chapter 3 and Appendix A. We first remind that the wave function solution of Equation (5.1), in the limit $g_{\sigma\sigma'} \rightarrow +\infty$, for any σ, σ' takes the form [Volosniev et al., 2014, Deuretzbacher et al., 2014]

$$\Psi(x_1, \dots, x_N) = \sum_{P \in S_N} a_P \theta_P(x_1 < \dots < x_N) \Psi_{TB}(x_1, \dots, x_N). \quad (5.2)$$

The index P indicates a permutation inside the permutation group of N elements, S_N , $\theta_P(x)$ is the generalized Heaviside function, which is equal to 1 in the coordinate sector $x_{P(1),\sigma_{P(1)}} < \dots < x_{P(N),\sigma_{P(N)}}$ and 0 elsewhere. In this discussion, we will work in the snippets basis [Fang et al., 2009, Volosniev et al., 2014], meaning that the sum over P refers to the $N!/(\frac{N}{2}!\frac{N}{2}!)$ independent sectors instead of the $N!$ possible. Since we will exclusively discuss bosonic mixtures, we have decided to map the spatial part of the ansatz in Equation (5.2) on the TB wave function. It's important to note that this mapping decision does not alter the symmetry of the entire wave function. However, the spin part must compensate for the natural symmetry of Ψ_{TB} so caution is necessary when interpreting the solution. Precisely, moving between different sectors will now be performed symmetrically by default.

We focus on the ground state and the most excited state solution that is not degenerate for balanced mixtures (in the limit $g_{\sigma\sigma'}$ very large but finite) so that we can set a_P real without loss of generality, and use the strong-coupling expansion approach [Volosniev et al., 2014].

The $SU(2)$ case :

As a reminder, the $SU(2)$ case refer to equal infinite interaction strengths ($g_{\uparrow\downarrow} = g_{\uparrow\uparrow} = g_{\downarrow\downarrow} = g \rightarrow \infty$). In this scenario, we have seen [Chapter 3] that the conditioned maximization of the energy slope $K(a_P)$ is equivalent to solving the eigenvalue problem for a matrix V whose expression depends on the type of mixture and trapping potential [Volosniev et al., 2014]. In the bosonic $SU(2)$ case, we have

$$[V^{SU}]_{i,j} = \frac{\hbar^4}{m^2} \begin{cases} \sum_{d,k \neq i} \alpha_{i_k} + 2 \sum_{b,k \neq i} \alpha_{i_k} & j = i \\ \alpha_{i,j} & j \neq i \end{cases}, \quad (5.3)$$

where the d -sum has to be taken over snippets k that transpose distinguishable particles, while the b -sum runs over sectors that transpose identical bosons.

The explicit form of V^{SU} for the case of a $2 + 2$ bosonic mixture is given in Appendix A and will be recalled at the end of this part. We note that the positive sign of the off-diagonal part depends on the preference made while building the many-body wave function in Equation (5.2), namely, on the choice to map on Ψ_{TB} instead of Ψ_{SF} .

The largest eigenvalues of this matrix correspond to the ground state and reads

$$K^{SU} = [\vec{a}_P^{SU}]^t V^{SU} \vec{a}_P^{SU}, \quad (5.4)$$

with \vec{a}_P^{SU} being the eigenvector of V^{SU} corresponding to this eigenvalue, which can be written under the form $K^{SU} = K_{\uparrow\downarrow}^{SU} + \sum_{\sigma=(\uparrow,\downarrow)} K_{\sigma\sigma}^{SU}$, to highlight the inter-component and intra-component contributions to the energy. Finally, we obtain $K^{SU} = 2N\alpha_N \hbar^4/m^2$.

The symmetry breaking case :

We now move to the more complicated case of two interacting TG gases, where $g_{\uparrow,\uparrow}$ and $g_{\downarrow,\downarrow}$ are infinite and the inter-components interaction strength $g_{\uparrow,\downarrow}$ is very large, but finite ($g_{\sigma,\sigma} \rightarrow \infty$ and $g_{\sigma,\sigma'} \rightarrow \infty$ but $g_{\sigma,\sigma} \neq g_{\sigma,\sigma'}$). The optimization procedure, outlined in Chapter 3, with respect to the small parameter $1/g_{\uparrow,\downarrow}$ leads to a matrix V^{SB} that now does not take into account any intra-component interaction terms

$$[V^{SB}]_{i,j} = \frac{\hbar^4}{m^2} \begin{cases} \sum_{d,k \neq i} \alpha_{i_k} & j = i \\ \alpha_{i,j} & j \neq i \end{cases}. \quad (5.5)$$

Note that the largest eigenvalue of V^{SB} , denoted as $K_{\uparrow\downarrow}^{SB}$ as well as the other eigenvalues, gives only an inter-component contribution to the energy, as $g_{\sigma\sigma}$ has been sent to infinity from the beginning. Of course, the symmetry breaking occurs for $N > 2$.

To clarify the precedent statement, let us take a step aside to explicit the matrices V^{SU} and V^{SB} as well as their largest eigenvalues and the corresponding eigenstate.

The matrices V^{SU} and V^{SB} for a $2 + 2$ mixture

Here, we will show examples of V^{SU} and V^{SB} matrices for the case of a balanced mixture with $N = 4$ bosons. We consider the snippet basis

$$\{|\uparrow\uparrow\downarrow\downarrow\rangle, |\uparrow\downarrow\uparrow\downarrow\rangle, |\uparrow\downarrow\downarrow\uparrow\rangle, |\downarrow\uparrow\uparrow\downarrow\rangle, |\downarrow\uparrow\downarrow\uparrow\rangle, |\downarrow\downarrow\uparrow\uparrow\rangle\} \quad (5.6)$$

For the $SU(2)$ mixture in a ring geometry, the V^{SU} matrix reads

$$V^{SU} = \frac{\hbar^4}{m^2} \alpha^{(N)} \begin{pmatrix} 6 & 1 & 0 & 0 & 1 & 0 \\ 1 & 4 & 1 & 1 & 0 & 1 \\ 0 & 1 & 6 & 0 & 1 & 0 \\ 0 & 1 & 0 & 6 & 1 & 0 \\ 1 & 0 & 1 & 1 & 4 & 1 \\ 0 & 1 & 0 & 0 & 1 & 6 \end{pmatrix}, \quad (5.7)$$

whose largest eigenvalue is $8\hbar^4\alpha^{(N)}/m^2$ with corresponding eigenvector $\vec{a}_P^{SU} = \frac{1}{\sqrt{6}}(1, 1, 1, 1, 1, 1)$.

For the SB mixture, the V^{SB} matrix reads

$$V^{SB} = \frac{\hbar^4}{m^2} \alpha^{(N)} \begin{pmatrix} 2 & 1 & 0 & 0 & 1 & 0 \\ 1 & 4 & 1 & 1 & 0 & 1 \\ 0 & 1 & 2 & 0 & 1 & 0 \\ 0 & 1 & 0 & 2 & 1 & 0 \\ 1 & 0 & 1 & 1 & 4 & 1 \\ 0 & 1 & 0 & 0 & 1 & 2 \end{pmatrix}. \quad (5.8)$$

The largest eigenvalue is $6\hbar^4\alpha^{(N)}/m^2$ and its corresponding eigenvector reads $\vec{a}_P^{SB} = \frac{1}{2\sqrt{3}}(1, 2, 1, 1, 2, 1)$.

It is worth making the case $N = 2$ explicitly. Indeed, because of the periodic boundary conditions, the $\delta(x_1 - x_2)$ contributes twice both for the diagonal terms and the off-diagonal ones. Thus, on the snippet basis $\{|\uparrow\downarrow\rangle, |\downarrow\uparrow\rangle\}$, one has the matrix

$$V^{SU} = V^{SB} = \frac{\hbar^4}{m^2} \alpha^{(N)} \begin{pmatrix} 2 & 2 \\ 2 & 2 \end{pmatrix}, \quad (5.9)$$

whose largest eigenvalue is $4\alpha^{(N)}\hbar^4/m^2$, in agreement with $K^{SU} = 2N\alpha^{(N)}\hbar^4/m^2$.

We note that V^{SB} is very similar to the matrix V^{SU} for a $SU(2)$ fermionic mixture [see Appendix A]. Indeed $[V_F^{SU}]_{i,i} = [V^{SB}]_{i,i}$, and $[V_F^{SU}]_{i,j} = -[V^{SB}]_{i,j}$ if $i \neq j$. The two matrices have the same eigenvalues, but the eigenstates do not have the same symmetry, which is well-defined for the case of $SU(2)$ fermions but is not for the case of two interacting TG gases, as we will see in the next section. Let us point out that, in contrast to V^{SU} that can be mapped on a XXX spin-chain model (for both fermionic and bosonic mixture) [Deuretzbacher et al., 2016], V^{SB} can notably be mapped on a XXZ model. We will illustrate this fascinating property in the next section.

Mapping on the XXX spin-chain model for $SU(2)$ mixtures

In the strong-interacting limit, in the case of $SU(2)$ bosons or fermions, the Hamiltonian Equation (5.1) can be mapped into a spin-chain model. To be precise, at the order $1/g$ one can write [Deuretzbacher et al., 2014]

$$\hat{H} - \mathbb{1}E_{g \rightarrow \infty} = -V_{B,F}^{SU}/g = -NJ\mathbb{1} \mp J \sum_{j=1}^N \hat{P}_{j,j+1}, \quad (5.10)$$

where $J = \alpha^{(N)}/g$, the - (+) sign applies to bosons (fermions). Since the permutation operator $\hat{P}_{j,j+1}$ can be written as a function of product of Pauli matrices $\hat{P}_{j,j'} = (\vec{\sigma}^{(j)}\vec{\sigma}^{(j')} + \mathbb{1})/2$ acting on-site j and j' , it is straightforward to show that it is possible to map Equation (5.10) on a Heisenberg XXX chain model, both for bosons and fermions: a ferromagnetic one for $SU(2)$ bosons,

$$-\frac{V_B^{SU}}{g} = -2J \sum_{j=1}^N \vec{S}^{(j)} \vec{S}^{(j+1)} - \frac{3}{2}NJ\mathbb{1}, \quad (5.11)$$

and an anti-ferromagnetic one for $SU(2)$ fermions,

$$-\frac{V_F^{SU}}{g} = 2J \sum_{j=1}^N \vec{S}^{(j)} \vec{S}^{(j+1)} - \frac{1}{2}NJ\mathbb{1}, \quad (5.12)$$

where $\vec{S} = \vec{\sigma}/2$ are the spin operators.

Mapping on the XXZ spin-chain model for $SU(2)$ breaking mixtures

For the SB case, the Hamiltonian can be written

$$\begin{aligned} \hat{H} - \mathbb{1}E_{g \rightarrow \infty} &= -V^{SB}/g \\ &= -V_B^{SU}/g - 2J \sum_{j=1}^N \left(P_{j,j+1} - |s\rangle\langle s| \hat{P}_{j,j+1} |s\rangle\langle s| \right) \\ &= -NJ\mathbb{1} - J \sum_{j=1}^N \hat{P}_{j,j+1} + 2J \sum_{j=1}^N |s\rangle\langle s| \hat{P}_{j,j+1} |s\rangle\langle s|, \end{aligned} \quad (5.13)$$

where $|s\rangle\langle s|$ is the projector on the snippet basis so that the last term applies only to diagonal elements. From this writing, the origin of the SB is clear: the term $-J \sum_{j=1}^N \hat{P}_{j,j+1}$ is the bosonic one, while the term $+2J \sum_{j=1}^N |s\rangle\langle s| \hat{P}_{j,j+1} |s\rangle\langle s|$ is at the origin of a "partial fermionization" acting only partially on the system (on the diagonal terms). One can show that

$$2J \sum_{j=1}^N |s\rangle\langle s| \hat{P}_{j,j+1} |s\rangle\langle s| = J \sum_{j=1}^N (\mathbb{1} + 4S_z^{(j)} S_z^{(j+1)}). \quad (5.14)$$

Thus we get a XXZ Heisenberg chain Hamiltonian:

$$-\frac{V^{SB}}{g} = -2J \sum_{j=1}^N (S_x^{(j)} S_x^{(j+1)} + S_y^{(j)} S_y^{(j+1)} - S_z^{(j)} S_z^{(j+1)}) - \frac{1}{2}NJ\mathbb{1}. \quad (5.15)$$

Remark that such a XXZ Hamiltonian can be mapped on a XXX one with an opposite sign of J by applying the unitary transformation $U = \prod_{\ell=\text{even}} 2S_z^{(\ell)}$ [Takahashi, 1999, Volosniev et al., 2015]. Such operator *does not preserve the symmetry* (does

not commute with the operator $\Gamma^{(2)}$, and its action is equivalent to map TG bosons on non-interacting fermions and vice-versa. On our snippet basis,

$$U = \begin{pmatrix} -1 & 0 & 0 & 0 & 0 & 0 \\ 0 & 1 & 0 & 0 & 0 & 0 \\ 0 & 0 & -1 & 0 & 0 & 0 \\ 0 & 0 & 0 & -1 & 0 & 0 \\ 0 & 0 & 0 & 0 & 1 & 0 \\ 0 & 0 & 0 & 0 & 0 & -1 \end{pmatrix}. \quad (5.16)$$

5.1.2 Analysis of the symmetry breaking

We now recall the mandatory elements to characterize the symmetry properties of the two different ground states using irreducible representations of the permutation group S_N . We will show in this section that the ground state of the $SU(2)$ Hamiltonian has a well-defined symmetry, whereas the one of the symmetry breaking case does not. In order to quantify the symmetry breaking associated with the many-body state

$$\Psi_{SB}(x_1, \dots, x_N) = \sum_{P \in S_N} a_P^{SB} \theta_P(x_1, \dots, x_N) \Psi_{TB}(x_1, \dots, x_N). \quad (5.17)$$

We calculate the expectation value of the 2-cycle class-sum operator $\Gamma^{[2]} = \frac{1}{2} \sum_{i \neq j} \hat{P}_{ij}$ (see Chapter 3) whose eigenvalues $\gamma^{[2]}$

$$\gamma_{[\Lambda]}^{[2]} = \frac{1}{2} \sum_i [\lambda_i(\lambda_i - 2i + 1)], \quad (5.18)$$

are directly related to Young's diagrams $Y_{[\Lambda]}$, with an increasing number of boxes λ_i at line i . Thus, for the fully symmetric $SU(2)$ ground state, corresponding to the Young's diagram $[N] = \square\square\square \cdots \square\square\square$, one has $\gamma_{[N]}^{[2]} = \gamma_S^{(2)} = N(N-1)/2$, namely $\gamma_S^{(2)}$ is given by the number of pairs in a system of N particles. Instead the eigenvalue $\gamma_{[N/2, N/2]}^{[2]} = \gamma_A^{(2)}$ (the most anti-symmetric scenario), corresponding to the Young's diagram $[N/2, N/2] = \square\square\square \cdots \square\square\square$, is equal to $N(N-4)/4$. This corresponds to the number of pairs in a system of $N/2$ particles (the length of a row) minus $N/2$ (the number of columns).

As a side note, one can show that in the case of $SU(\kappa)$ mixtures $\Gamma^{[2]}$ can be written in terms of the spin matrices as

$$\Gamma^{(2)} = 2 \sum_{i < j} \vec{S}^{(i)} \vec{S}^{(j)} + \frac{N(N-1)}{4} \mathbb{1}, \quad (5.19)$$

where we have used $\hat{P}_{j,j'} = (\vec{\sigma}^{(j)} \vec{\sigma}^{(j')} + \mathbb{1})/2$. In particular for $SU(2)$ balanced mixtures it reduces to

$$\Gamma^{(2)} = S^2 + \frac{N(N-4)}{4} \mathbb{1}. \quad (5.20)$$

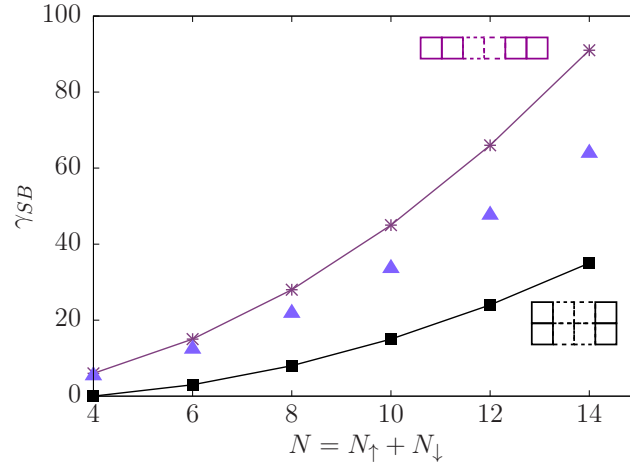


Figure 5.1: γ_{SB} as a function of N (triangles) for the symmetry breaking ground-state. The stars and the boxes represent the eigenvalues $\gamma_S^{(2)}$ and $\gamma_A^{(2)}$ respectively. The lines are a guide to the eye. Adapted from [Aupetit-Diallo et al., 2022].

In Figure 5.1, we plot $\gamma_{SB} = \langle \Psi^{SB} | \Gamma^{(2)} | \Psi^{SB} \rangle$ as a function of N and we compare it with $\gamma_S^{(2)}$ and $\gamma_A^{(2)}$. We observe that, by increasing N , γ_{SB} moves away from $\gamma_S^{(2)}$ to position itself halfway between $\gamma_S^{(2)}$ and $\gamma_A^{(2)}$. We have checked that the corresponding symmetry breaking ground state (\vec{a}_P^{SB}) does not correspond to any well-defined symmetry.

To better understand what means the $SU(2)$ breaking from the Young's diagrams point of view, we will dissect the case of $N = 4$ bosons.

The example of a 2 + 2 bosonic mixture

For the case of a balanced mixture of $N = 4$ bosons, the $\Gamma^{(2)}$ matrix can be written in the snippet basis (taking into account the initial ansatz for the many-body wave function Equation (5.2)) as

$$\Gamma^{(2)} = \begin{pmatrix} 2 & 1 & 1 & 1 & 1 & 0 \\ 1 & 2 & 1 & 1 & 0 & 1 \\ 1 & 1 & 2 & 0 & 1 & 1 \\ 1 & 1 & 0 & 2 & 1 & 1 \\ 1 & 0 & 1 & 1 & 2 & 1 \\ 0 & 1 & 1 & 1 & 1 & 2 \end{pmatrix}, \quad (5.21)$$

which can be diagonalized. This yields three representations of dimension 1, 3 and 2 with eigenvalues $\gamma_2 = 6, 2, 0$ corresponding to the diagrams $\square\square\square\square$, $\begin{array}{|c|c|} \hline \square & \square \\ \hline \square & \square \\ \hline \end{array}$ and $\begin{array}{|c|c|} \hline \square & \square \\ \hline \square & \square \\ \hline \end{array}$. The eigenstate corresponding to the irreps. of dimension one is $\vec{v}_6 = \frac{1}{\sqrt{6}}(1, 1, 1, 1, 1, 1)$ which is identical to the ground state of the $SU(2)$ model. The other eigenvectors are $\vec{v}_{2_1} = \frac{1}{\sqrt{2}}(-1, 0, 0, 0, 0, 1)$, $\vec{v}_{2_2} = \frac{1}{\sqrt{2}}(0, -1, 0, 0, 1, 0)$, $\vec{v}_{2_3} = \frac{1}{\sqrt{2}}(0, 0, -1, 1, 0, 0)$, $\vec{v}_{0_1} = \frac{1}{2}(1, 0, -1, -1, 0, 1)$ and $\vec{v}_{0_2} = \frac{1}{2\sqrt{3}}(1, -2, 1, 1, -2, 1)$. The system's ground state with broken $SU(2)$ symmetry will be a linear superposition of states with different symmetries. In this precise case we obtain that $\vec{a}_P^{SB} = \frac{2\sqrt{2}}{3}\vec{v}_6 + \frac{1}{3}\vec{v}_{0_2}$, namely the symmetries involved are mainly $\square\square\square\square$ ($\frac{8}{9}$) but also $\begin{array}{|c|c|} \hline \square & \square \\ \hline \square & \square \\ \hline \end{array}$ ($\frac{1}{9}$).

As expected, we see with this little example the direct effect of the symmetry breaking: the ground state of the resulting spin mixture will no longer have a well-defined symmetry. However, from a formal point of view, we still have to prove that it will be the case for any mixtures described by the Hamiltonian Equation (5.1). For this, we will consider the commutator between the Hamiltonian of our model and $\hat{\Gamma}^{[2]}$.

5.1.3 Proof of the $SU(2)$ symmetry breaking

Before considering the SB Hamiltonian, it is worth beginning with the $SU(2)$ scenario. First, it will help to foresee the expectations for the more involving case of SB. Moreover, as the symmetry is obviously realized in this case, we already know the result of the commutator. By then, we add a layer of control on the derivations.

5.1.4 Commutation between $\hat{\Gamma}^{[2]}$ and $\hat{H}_P^{SU} = V^{SU}/g$

For this demonstration, we can simplify the Hamiltonian as $\hat{H}_P(J_i, \Delta = \pm 1) = \hat{H}_P^{SU} \simeq \sum_i J_i \hat{P}_{i,i+1}$ and use the form $\hat{\Gamma}^{[2]} = \frac{1}{2} \sum_{i \neq j} \hat{P}_{i,j}$ for the 2-cycle class sum operator. Thus, the commutation problem boils down to considering the following commutator

$$\left[\sum_i J_i \hat{P}_{i,j}, \frac{1}{2} \sum_{i' \neq j'} \hat{P}_{i',j'} \right] = \left[\sum_i J_i \hat{P}_{i,j}, \sum_{i',j'} \hat{P}_{i',j'} \right] = \sum_{i,i',j'} [J_i \hat{P}_{i,j}, \hat{P}_{i',j'}], \quad (5.22)$$

where we will set $j = i + 1$ afterward. We have replaced $\sum_{i' \neq j'}$ by $\sum_{i',j'}$ as it simplifies the derivation and only adds identity terms $P_{i,i}$ which will not contribute to the commutation problem.

The initial step is to rewrite the permutation operators in the second quantization [Auerbach, 1994, Zhang & Wang, 2006]

$$\hat{P}_{i,j} = \sum_{\mu,\nu} \hat{F}_\mu^\nu(i) \hat{F}_\nu^\mu(j), \quad (5.23)$$

where $\hat{F}_\mu^\nu(i) = \hat{a}_{i,\mu}^\dagger \hat{a}_{i,\nu}$, \hat{a}^\dagger and \hat{a} are respectively the creation and annihilation operators, with μ and ν the spin- s projection indices going from 1 to $2s + 1$ and i and j are the sites indices. It is important to notice that the $\hat{F}_\mu^\nu(i)$'s are the generators of the $SU(n)$ group satisfying the commutation relation of the $SU(n)$ Lie algebra

$$\left[F_\mu^\nu(i), F_{\nu'}^{\mu'}(j) \right] = \delta_i^j \left(\delta_{\mu'}^\nu F_\mu^{\nu'}(i) - \delta_\mu^{\nu'} F_{\mu'}^\nu(j) \right). \quad (5.24)$$

To lighten the following derivation, we will drop the circumflex from the P 's and F 's operators for the rest of this section. We can now develop the commutator as

$$\begin{aligned}
[J_i P_{i,j}, P_{i',j'}] &= \left[\sum_{\mu,\nu} F_\mu^\nu(i) F_\nu^\mu(j), \sum_{\mu',\nu'} F_{\mu'}^{\nu'}(i') F_{\nu'}^{\mu'}(j') \right] \\
&= J_i \underbrace{\sum_{\mu,\nu,\mu',\nu'} F_\mu^\nu(i) F_\nu^\mu(j) F_{\mu'}^{\nu'}(i') F_{\nu'}^{\mu'}(j')}_{=P_{ij}P_{i'j'}} - J_{i'} \underbrace{\sum_{\mu,\nu,\mu',\nu'} F_{\mu'}^{\nu'}(i') F_{\nu'}^{\mu'}(j') F_\mu^\nu(i) F_\nu^\mu(j)}_{=P_{i'j'}P_{ij}},
\end{aligned} \tag{5.25}$$

thus by swapping the two central F operators, we have for the second sum $P_{i'j'}P_{ij}$

$$\begin{aligned}
P_{i'j'}P_{ij} &= \sum_{\mu,\nu,\mu',\nu'} F_{\mu'}^{\nu'}(i') F_\mu^\nu(i) F_{\nu'}^{\mu'}(j') F_\nu^\mu(j) - \sum_{\mu,\nu,\mu',\nu'} F_{\mu'}^{\nu'}(i') \left[F_\mu^\nu(i), F_{\nu'}^{\mu'}(j') \right] F_\nu^\mu(j) \\
&= \underbrace{\sum_{\mu,\nu,\mu',\nu'} F_{\mu'}^{\nu'}(i') F_\mu^\nu(i) F_{\nu'}^{\mu'}(j') F_\nu^\mu(j)}_{=(\star_1)} - \underbrace{\delta_i^{j'} \sum_{\mu,\nu,\mu',\nu'} F_{\mu'}^{\nu'}(i') \left(\delta_\nu^{\nu'} F_\mu^{\mu'}(i) - \delta_\mu^{\mu'} F_{\nu'}^{\nu'}(j') \right) F_\nu^\mu(j)}_{=(\blacktriangle_1)}.
\end{aligned} \tag{5.26}$$

We can actually repeat this swapping process to the terms generated to recreate a $P_{ij}P_{i'j'}$ and suppress the one in Equation (5.25). It will nonetheless introduce a $(J_i - J_{i'})P_{ij}P_{i'j'}$, but as we ultimately sum over i, j, i', j' , we can always relabel these indices in a way which cancel it. Then, as done with Equation (5.26), the ensuing steps are

$$\begin{aligned}
(\star_1) &= \sum_{\mu,\nu,\mu',\nu'} F_\mu^\nu(i) F_{\mu'}^{\nu'}(i') F_{\nu'}^{\mu'}(j') F_\nu^\mu(j) - \sum_{\mu,\nu,\mu',\nu'} \left[F_\mu^\nu(i), F_{\mu'}^{\nu'}(i') \right] F_{\nu'}^{\mu'}(j') F_\nu^\mu(j) \\
&= \underbrace{\sum_{\mu,\nu,\mu',\nu'} F_\mu^\nu(i) F_{\mu'}^{\nu'}(i') F_{\nu'}^{\mu'}(j') F_\nu^\mu(j)}_{=(\star_2)} - \underbrace{\delta_i^{i'} \sum_{\mu,\nu,\mu',\nu'} \left(\delta_\nu^{\nu'} F_\mu^{\mu'}(i) - \delta_\mu^{\mu'} F_{\nu'}^{\nu'}(i') \right) F_{\nu'}^{\mu'}(j') F_\nu^\mu(j)}_{=(\blacktriangle_2)},
\end{aligned} \tag{5.27}$$

$$\begin{aligned}
(\star_2) &= \sum_{\mu,\nu,\mu',\nu'} F_\mu^\nu(i) F_{\mu'}^{\nu'}(i') F_\nu^\mu(j) F_{\nu'}^{\mu'}(j') - \sum_{\mu,\nu,\mu',\nu'} F_\mu^\nu(i) F_{\mu'}^{\nu'}(i') \left[F_\nu^\mu(j), F_{\nu'}^{\mu'}(j') \right] \\
&= \underbrace{\sum_{\mu,\nu,\mu',\nu'} F_\mu^\nu(i) F_{\mu'}^{\nu'}(i') F_\nu^\mu(j) F_{\nu'}^{\mu'}(j')}_{=(\star_3)} - \underbrace{\delta_j^{j'} \sum_{\mu,\nu,\mu',\nu'} F_\mu^\nu(i) F_{\mu'}^{\nu'}(i') \left(\delta_\nu^{\mu'} F_\nu^{\mu'}(j) - \delta_\nu^{\mu'} F_{\nu'}^{\mu'}(j') \right)}_{=(\blacktriangle_3)},
\end{aligned} \tag{5.28}$$

and

$$\begin{aligned}
(\star_3) &= \sum_{\mu,\nu,\mu',\nu'} F_\mu^\nu(i) F_\nu^\mu(j) \overset{\leftarrow}{F_{\mu'}^{\nu'}(i')} F_{\nu'}^{\mu'}(j') - \sum_{\mu,\nu,\mu',\nu'} F_\mu^\nu(i) \left[F_\nu^\mu(j), F_{\mu'}^{\nu'}(i') \right] F_{\nu'}^{\mu'}(j') \\
&= \underbrace{\sum_{\mu,\nu,\mu',\nu'} F_\mu^\nu(i) F_{\mu'}^{\nu'}(i') F_\nu^\mu(j) F_{\nu'}^{\mu'}(j')}_{=P_{i,j} P_{i',j'}} - \delta_j^{i'} \underbrace{\sum_{\mu,\nu,\mu',\nu'} F_\mu^\nu(i) \left(\delta_\mu^{\mu'} F_\nu^{\nu'}(j) - \delta_\nu^{\nu'} F_{\mu'}^\mu(i') \right) F_{\nu'}^{\mu'}(j')}_{=(\blacktriangle_4)}.
\end{aligned} \tag{5.29}$$

Hence, the commutator $[P_{i,j}, P_{i',j'}]$ is only equal to $(\blacktriangle_1) + (\blacktriangle_2) + (\blacktriangle_3) + (\blacktriangle_4)$. By reorganizing all the terms, it follows

$$[P_{i,j}, P_{i',j'}] = \sum_{\mu,\nu,\mu',\nu'} -\delta_i^{j'} \delta_\nu^{\nu'} F_{\mu'}^{\nu'}(i') F_\mu^{\mu'}(i) F_\nu^\mu(j) + \delta_j^{i'} \delta_\nu^{\nu'} F_\mu^\nu(i) F_{\mu'}^\mu(i') F_{\nu'}^{\mu'}(j') \tag{5.30}$$

$$+ \sum_{\mu,\nu,\mu',\nu'} +\delta_i^{j'} \delta_\mu^{\mu'} F_{\mu'}^{\nu'}(i') F_{\nu'}^\nu(j') F_\nu^\mu(j) - \delta_j^{i'} \delta_\mu^{\mu'} F_\mu^\nu(i) F_\nu^{\nu'}(j) F_{\nu'}^{\mu'}(j') \tag{5.31}$$

$$+ \sum_{\mu,\nu,\mu',\nu'} -\delta_i^{j'} \delta_\mu^{\nu'} F_\mu^\nu(i) F_{\nu'}^{\mu'}(j') F_\nu^\mu(j) + \delta_j^{i'} \delta_\nu^{\nu'} F_\mu^\nu(i) F_{\mu'}^{\nu'}(i') F_{\nu'}^{\mu'}(j') \tag{5.32}$$

$$+ \sum_{\mu,\nu,\mu',\nu'} +\delta_i^{j'} \delta_\mu^{\nu'} F_{\mu'}^{\nu'}(i') F_{\nu'}^{\mu'}(j') F_\nu^\mu(j) - \delta_j^{i'} \delta_\nu^{\mu'} F_\mu^\nu(i) F_{\mu'}^{\nu'}(i') F_{\nu'}^{\mu'}(j), \tag{5.33}$$

where we have kept a numeration for the different lines to facilitate their future references. This equation is in agreement with the fact that permutation matrices do not commute two-by-two. The method now is to place back the sum over i, j, i', j' , which allows relabeling the indices to make explicit that each line cancels out. Since the idea is the same for every term of $[P_{i,j}, P_{i',j'}]$, we will just detail the procedure for the first line. If we make the transformation $\mu \leftrightarrow \mu'$ in the second part of the line (5.30), one can find

$$(5.30) = \sum_{\mu,\nu,\mu',\nu'} -F_\mu^\nu(i') F_{\mu'}^{\mu'}(i) F_\nu^{\mu'}(j) + F_\mu^\nu(i) F_{\mu'}^{\mu'}(i') F_\nu^{\mu'}(j). \tag{5.34}$$

This time doing the transformation $i \leftrightarrow i'$ in (5.34) we finally have $\sum_{i,j,i',j'} (5.34) = 0$. Similarly one can find that $\sum_{i,j,i',j'} (5.31) = \sum_{i,j,i',j'} (5.32) = \sum_{i,j,i',j'} (5.33) = 0$ which imply that $[\sum_{i,j} P_{i,j}, \sum_{i',j'} P_{i',j'}] = 0$. Moreover, we notice that each line only depends on three position indices (one remaining free). We choose this index to be j and rewrite the commutator as $[\sum_i P_{i,j}, \sum_{i',j'} P_{i',j'}]$ which imply that for a given set of i, i' , and j' every j could be considered. Said differently, $[\sum_i P_{i,j}, \sum_{i'} P_{i',j'}] = 0$ for every j . Thus we can set $[\sum_i P_{i,i+n}, \sum_{i'} P_{i',j'}] = 0$ ($j = i + n$, with $n \in \mathbb{N}^*$), the case $n = 1$ corresponding to our spin Hamiltonian Equation (5.10). Finally, we have for this case

$$[H_P^{SU}, \Gamma^{(2)}] = 0. \tag{5.35}$$

This derivation actually stands to $SU(\kappa)$ spin mixtures with any κ has the Hamiltonian Equation (5.10) is general. Moreover, one must be careful as this derivation

only stands to J_i only positive (or only negative for another mapping). In particular, certain configurations of J_i , such as $J_1 = J$, $J_2 = -mJ$, $J_3 = J$, $m \in \mathbb{N}$ for $2 + 2$ mixtures, are not included. We want to emphasize the implication of this outcome: if every spin species feels the trap in the same way (same sign of the J_i 's), any type of external trapping geometry (represented by the J_i 's set) will present in a $SU(\kappa)$ symmetry. Alongside, this derivation also spotlights that isotropic spin Hamiltonians with interactions to n -th neighbors must remarkably satisfy the $SU(\kappa)$ symmetry. This extends the application of the class-sum method study to an exceptional variety of systems.

5.1.5 Commutation between class sum operators and $H_P^{SB} = V^{SB}/g$

The derivation is similar to the $SU(\kappa)$ case and, therefore, will only be outlined. Starting with the Equation (5.13) form of V^{SB} one can find that

$$[V^{SB}/g, \Gamma^{(2)}] = [4 \sum_j J_j S_z^{(j)} S_z^{(j+1)}, 2 \sum_{n,j'} \vec{S}^{(j')} \vec{S}^{(j'+n)}]. \quad (5.36)$$

Again, using the commutation relation of spin matrices, one can obtain

$$[V^{SB}/g, \Gamma^{(2)}] = 8 \sum_{j,n} J_j \left\{ \begin{aligned} & \left(S_+^{(j)} S_-^{(j+n)} - S_-^{(j)} S_+^{(j+n)} \right) \left(S_z^{(j+n+1)} - S_z^{(j+1)} \right) \\ & + \left(S_z^{(j+n-1)} - S_z^{(j-1)} \right) \left(S_+^{(j)} S_-^{(j+n)} - S_-^{(j)} S_+^{(j+n)} \right) \end{aligned} \right\}, \quad (5.37)$$

that doesn't vanish regardless of the type of mixture ($\forall \kappa$) and the number of particles (for $N > 2$). This result proves that H^{SB} breaks the $SU(\kappa)$ symmetry.

5.1.6 Correlations analysis

The previous analysis demonstrates that the protocol used in an experiment to set particle interactions to a very large value has strong consequences on the symmetry properties of the ground state. However, the exchange symmetry, or the expectations of the two-cycle class sum operators, are not accessible experimentally. We, therefore, now look for a routinely measured physical observable that would keep a trace of the non-trivial symmetry of the ground state. We know from Chapter 1 that the simplest, yet strongly depending on the symmetry of the wave function, is the momentum distribution. This one reads in case of a system with PBC

$$n(k) = \int_{-L/2}^{L/2} e^{-ikt} \rho_1(t) dt, \quad (5.38)$$

where we have set $\rho_1(x, y) = \rho_1(x - y) = \rho_1(t)$ for the first order correlation function. As presented in Chapter 4, thanks to the separation between spin and spatial part

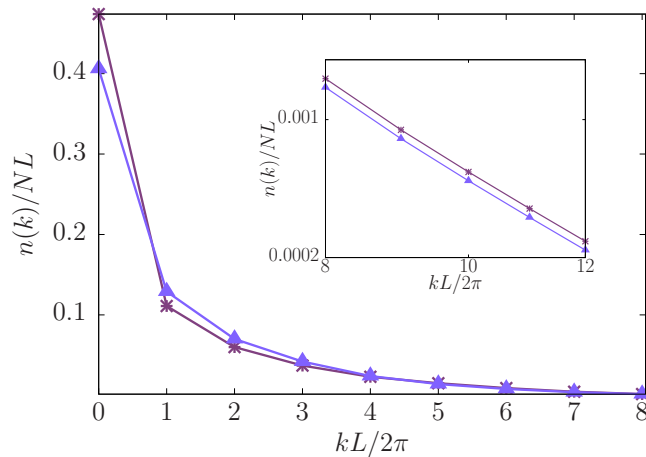


Figure 5.2: Normalized momentum distribution $n(k)/N$ in units of $1/L$ as a function of $kL/(2\pi)$ for a mixture of 4+4 bosons. The stars are the data for the $SU(2)$ mixture and the triangles for the SB system. The inset, in a log-log scale, is a zoom on the tails. The lines are a guide to the eye. Adapted from [Aupetit-Diallo et al., 2022].

in the wave function, the same decoupling can be done in $\rho_1(t)$. In our case, this reads

$$\rho_1(t) = \sum_{\sigma} N_{\sigma} \rho_{1,\sigma}(t), \quad (5.39)$$

where

$$\rho_{1,\sigma}(t) = \sum_{j=1}^N c_{\sigma}^{(1,j)} \rho^{(1,j)}(t). \quad (5.40)$$

It should be pointed out that the exchange symmetry properties affect only the spin correlation function $c_{\sigma}^{(1,j)}$. In parallel, the spatial correlation function $\rho^{(1,j)}(t)$ is only affected by the trapping geometry.

In Figure 5.2, we compare the ground state's momentum distribution of the SB case with the $SU(2)$ mixture. We recall that the latter coincides with the momentum distribution of a single-component TG gas. We notice remarkable differences between the two at small and large momenta. In particular, both the peak centered around $k = 0$ and the tails at large k (inset of Figure 5.2) of the momentum distribution are larger for the $SU(2)$ mixture. In contrast, the one of the SB mixture is higher at intermediate wavevectors.

To explore these features, in the following sections, we will focus our study on n_0 and $\lim_{k \rightarrow \infty} n(k)k^4$ that provide information about large-distance and short-distance correlations, respectively. As a reminder, in the ring geometry, n_0 coincides with the quasi-condensate fraction of the system.

5.1.7 Long-distance coherence

We now discuss in detail the large-distance coherence, which corresponds to small momenta in the momentum distribution. Specifically, we restrict this analysis to the zero-momentum occupation number for its importance as a measure of long-distance coherence in quantum systems. For the balanced mixture discussed in this manuscript $\rho_{1,\sigma}(t)$ is independent of σ , so n_0 is given by

$$n_0 = \int_{-L/2}^{L/2} dt \rho_1(t) = 2 \sum_{j=1}^{N/2} c_{\sigma}^{(1,j)} R^j, \quad (5.41)$$

where we have defined $R^j = \int_{-L/2}^{L/2} dt \rho^{(1,j)}(t)$ and we have used that $c^{(1,j)} = c^{(1,N-j+1)}$. We are mostly interested in the asymptotic behavior at a large number of particles that we approach by increasing the number of particles up to $N = 14$. The results of our exact calculations are actually well approximated by a simple fitting function R^j at a large number of particles,

$$R^j \underset{N \rightarrow \infty}{\simeq} \frac{3}{4} \frac{1}{\sqrt{2j-1}}. \quad (5.42)$$

For the $SU(2)$ case, $c^{(1,j)} = 1, \forall j$. This implies that the ground state of the $SU(2)$ system coincides with that of a TG gas with a single spin component. Indeed, in the presence of a single component mixture, the spin correlation function would have been maximum $\forall j$. The resulting approximated expression for the zero-momentum occupation, in the limit $N \gg 1$, reads

$$n_0^{SU}(N \gg 1) \simeq \frac{3}{2} \sum_{j=1}^{N/2} \frac{1}{\sqrt{2j-1}}. \quad (5.43)$$

This approximation in Equation (5.43) provides the correct leading term of the function $n_0^{SU}(N)$ given in [Forrester et al., 2003b] for a single component TG gas,

$$n_0^{SU}(N) = 1.54\sqrt{N} - 0.58 + \frac{0.03}{\sqrt{N}}. \quad (5.44)$$

For the SB case, the $c^{(1,j)}$'s depend on N for small values of N but they seem to converge rapidly to a well-defined value $c^{(1,j)}$ for any j (see Table 5.1).

Breaking the $SU(2)$ symmetry makes the two spin states distinguishable. Thus, we expect that, at large j , there is no more coherence between the first spin and the j -th one, so that the probability $c^{(1,j)}$ to have the same spin state has to tend to $1/2$. Indeed the $c^{(1,j)}$'s can be fitted with the function

$$f_{1j} = \left(\frac{1}{2} + \frac{1}{2} e^{-b(j-1)^a} \right), \quad (5.45)$$

a and b being positive and slightly depending on N . The exponential decay part of Equation (5.45) does not contribute to the thermodynamic limit, so that

$$\lim_{N \rightarrow \infty} \frac{n_0^{SB}}{n_0^{SU}} = \frac{1}{2}. \quad (5.46)$$

Table 5.1: Behaviour of the absolute value of the coefficients $c^{(1,j)}$ as functions of N for the case of breaking symmetry.

$N/2$	$c^{(1,2)}$	$c^{(1,3)}$	$c^{(1,4)}$	$c^{(1,5)}$	$c^{(1,6)}$	$c^{(1,7)}$	$c^{(1,8)}$
2	0.833						
3	0.811	0.769					
4	0.804	0.750	0.721				
5	0.801	0.742	0.702	0.687			
6	0.799	0.737	0.692	0.671	0.660		
7	0.798	0.735	0.687	0.662	0.645	0.638	
8	0.797	0.733	0.683	0.656	0.636	0.625	0.619

In Figure 5.3, we plot the exact results for n_0^{SU} and n_0^{SB} , together with the analytical approximated expression for $n_0^{SU}(N)$ given in Equation (5.44) and that for the symmetry breaking case,

$$n_0^{SB}(N) = 0.77\sqrt{N} + 1.64 - \frac{1.61}{\sqrt{N}}. \quad (5.47)$$

Equation (5.47) has been obtained by fitting the data obtained by the exact calculation and by fixing the first coefficient to 0.77 (half the first coefficient of Equation (5.44)).

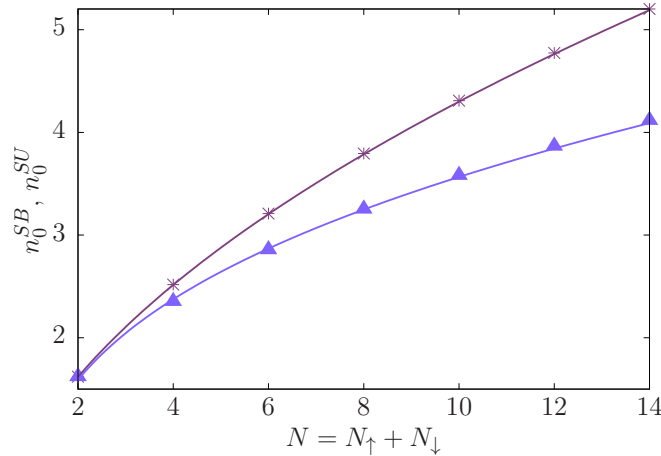


Figure 5.3: The zero-momentum occupation numbers n_0^{SU} (stars) and n_0^{SB} (triangles), for a balanced mixture, as a function of the total number of particles N . The exact results (points) are compared with the approximated function (lines) given respectively in Equations (5.44) and (5.47). Adapted from [Aupetit-Diallo et al., 2022].

Breaking the $SU(2)$ symmetry has the effect of destroying long-distance coherence. For our particular model, the zero-momentum occupation number is reduced by a factor of two. This macroscopic consequence of a microscopic symmetry property is a central result as it constitutes an experimental smoking gun of $SU(2)$ symmetry breaking.

5.1.8 Short-distance correlations: the Tan's contact

We now proceed with the discussion of short-distance correlations. This time, they are observable in the tails of the momentum distribution. For a system with zero-range interactions, the momentum distribution decays as k^{-4} . The prefactor $\mathcal{K} = \lim_{k \rightarrow \infty} n(k)k^4$ is the so-called Tan's contact \mathcal{C} [Tan, 2008c]. This observable is proportional to the cusps in the systems, namely to the symmetric exchanges between particles [Decamp et al., 2016b, Decamp et al., 2017]. In this section, we will focus on the modification of the Tan's contact due to symmetry breaking.

For the $SU(2)$ -symmetric system, the Tan's contact is proportional to the energy slope K^{SU} ,

$$\mathcal{C}^{SU} = \frac{2m^2}{\hbar^4} K^{SU}. \quad (5.48)$$

We see from the cusp conditions Equation (2.5) that in the ring geometry for the $SU(2)$ case, there are N cusps, and each cusp brings a contribution that is proportional to twice α_N , so that $K^{SU} = 2N\alpha_N\hbar^4/m^2$ and thus $\mathcal{C}^{SU} = 4N\alpha_N$.

For the SB case, $K_{\uparrow\downarrow}^{SB}$ takes into account only the inter-component contribution, as our starting point in the energy calculation is a two-component TG gas whose intra-species interaction strength is set to infinity from the beginning. However, the Tan's contact is related to both the intra- and inter-component contributions $[\partial_{1/g_{\sigma,\sigma}} E]_{g_{\sigma,\sigma} \rightarrow \infty}$ and $[\partial_{1/g_{\sigma,\sigma'}} E]_{g_{\sigma,\sigma'} \rightarrow \infty}$, the first term counting the cusps for exchanges of identical bosons, and the second giving the cusps for exchanges of bosons with different spins. Similarly to the $SU(2)$, in the SB case the contact is given by

$$\mathcal{C}^{SB} = \frac{2m^2}{\hbar^4} [(\vec{a}_P^{SB})^t V^{SU} \vec{a}_P^{SB}], \quad (5.49)$$

with \vec{a}_P^{SB} is the eigenvector of V^{SB} corresponding to its largest eigenvalue.

In Figure 5.4 we plot the ratio $\mathcal{C}^{SB}/\mathcal{C}^{SU}$ as a function of N . We observe that $\mathcal{C}^{SB}/\mathcal{C}^{SU}$ converges very rapidly to ~ 0.9 . Thus, for $N > 2$, the contact is lower for the SB case than for the $SU(2)$ mixture. As reported for other multicomponent mixtures [Decamp et al., 2016b], moving from the ideal case of fully symmetric exchanges also manifests itself in the lowering of the contact in this case. The modification is relatively small, which is caused by the fact that each component of the mixture is bosonic and, then, several cusps are still present in the SB case.

5.1.9 Concluding remarks

In this section, we have presented a model of a Bose-Bose mixture where exchange symmetry is broken and its solutions at large inter-particle interaction. Before summing up our conclusions, we would like to mention that the solution of such a model can also be obtained for any strength of the inter-particle interaction employing the Bethe ansatz solution for the Yang-Gaudin Hamiltonian [Sutherland, 1968, Gaudin, 1976]. Indeed, one can write in each coordinate sector Q such that

$$x_{Q(1,\uparrow)} < \dots < x_{Q(N,\downarrow)},$$

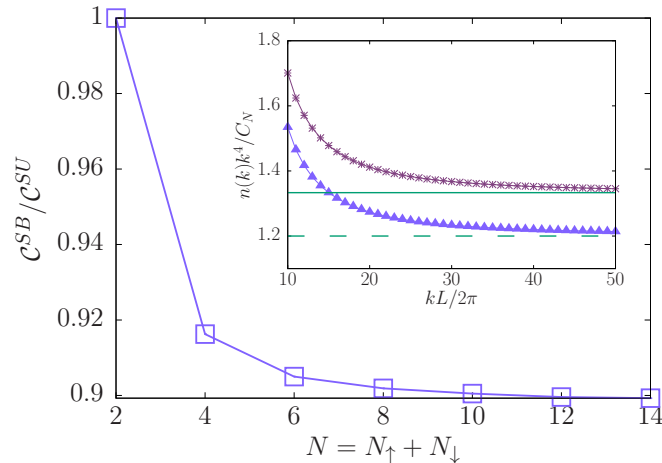


Figure 5.4: The ratio $\mathcal{C}^{SB}/\mathcal{C}^{SU}$ as a function of $N = N_{\uparrow} + N_{\downarrow}$ for balanced mixtures (the line is a guide to the eye). In the inset, we show $n(k)k^4$, in units of $C_N = N^2(N^2 - 1)/L^3$, as a function of $kL/(2\pi)$ for the case of a $SU(2)$ mixture (stars) and a SB one (triangles) of $N = 4+4$ bosons. The horizontal lines indicates the values of \mathcal{C}^{SU}/C_N (continuous line) and \mathcal{C}^{SB}/C_N (dashed line). Adapted from [Aupetit-Diallo et al., 2022].

$$\Psi_Q^{SB}(x_1, \dots, x_N) = \prod_{i,j} \prod_{\sigma=\uparrow,\downarrow} \text{sign}(x_{Q(i,\sigma)} - x_{Q(j,\sigma)}) \Psi_Q^{YG}(x_1, \dots, x_N), \quad (5.50)$$

where the function Ψ_Q^{YG} is the Bethe wave function for the $SU(2)$ Fermi gas in the coordinate sector Q . We recall the two main advantages of our method compared to the Bethe ansatz. First, the easy access to the first order correlation function provides a deep understanding of spatial and spin correlations up to the order $1/g_{\uparrow\downarrow}$. Second, it can be applied to any trapping potential. As soon as one knows the single-particle orbitals, such as for the case of a harmonic potential or a box trap, it is possible to write the exact solution for the many-body wave function and also for the symmetry breaking case.

In this study, we have shown that different spin states with different symmetries can be obtained by varying the protocol used in order to achieve the strong-repulsive limit. The symmetry breaking induced by the difference between the intra- and inter-specie interaction strengths affects both short- and large-distance correlations. However, the effect on long-distance coherence is particularly significant. We have observed a reduction by a factor of two in the zero-momentum occupation number for high numbers of particles, indicating the destruction of spin coherence at a large distance. This suggests that the zero-momentum occupation number is a highly sensitive observable for detecting symmetry breaking.

To conclude, our work provides a guide for the studies of the correlation properties of $SU(\kappa)$ mixtures in the strongly interacting regime, highlighting the importance of the protocol chosen to reach such a regime.

5.2 Spin mixtures with artificial gauge field on a ring

In this section, we will present the results obtained in collaboration with Giovanni Pecci and Anna Minguzzi from LPMMC [Pecci et al., 2023]. The idea is to consider a system with PBC with an artificial gauge field generated by an external global flux. This system is slightly more complicated than the previously discussed. However, the spin structure of the Hamiltonian remains unchanged. This motivated a $SU(\kappa)$ symmetry analysis aiming to provide new data about the system. In particular, we will show that such investigation adds another layer of information onto the system's spectrum but also unlocks a way to place the system in a controlled symmetry state.

5.2.1 Model and definitions

We consider a two-component Bose-Bose mixture of N atoms, made of N_\uparrow particles in one component (denoted as spin up) and N_\downarrow particles in the other component (denoted as spin down). We focus on the balanced case $N_\uparrow = N_\downarrow = N/2$. We place ourselves in the $SU(2)$ scenario, where every interaction strength is positive, equal, and denoted g . The gas is confined in a one-dimensional ring of radius $R = \frac{L}{2\pi}$, with L being the ring's circumference. We consider an artificial gauge field, e.g. induced by setting the system in rotation with frequency Ω inducing an effective flux $\Phi = 2\Omega\pi R^2$ flowing through the ring.

The Hamiltonian of the system is

$$\mathcal{H} = \sum_{j=1}^N \frac{1}{2m} (p_j - m\Omega R)^2 + g \sum_{j<\ell} \delta(x_j - x_\ell), \quad (5.51)$$

where m is the mass of the particles, $c = \frac{2m}{\hbar^2}g$ the diffusion strength, and $\tilde{\Phi} = \frac{\Phi}{\Phi_0}$, with $\Phi_0 = \frac{h}{m}$ the reduced flux. The kinetic part of the Hamiltonian can be rewritten as $\mathcal{H}_{kin} = \sum_{j=1}^N \frac{1}{2m} \left(p_j - \frac{2\pi\hbar}{L}\tilde{\Phi} \right)^2$. Hence, this model is integrable, and to solve it, we can rely on the Bethe ansatz method for spin mixtures [Sutherland, 1968, Li et al., 2003, Oelkers et al., 2006, Imambekov & Demler, 2006b] introduced in Chapter 3 at the difference that 2π times the rescaled flux now tilts the total momentum. Thus, the energy of the system is given by $E(\tilde{\Phi}) = \frac{\hbar^2}{2m} \sum_j (k_j - \frac{2\pi}{L}\tilde{\Phi})^2$ and the total momentum is $P = \hbar \sum_j (k_j - \frac{2\pi}{L}\tilde{\Phi})$. In addition, we set $\epsilon = \frac{\hbar^2\pi^2}{mL^2}$ as the energy scale.

In the following, we recall the crucial elements of the Bethe ansatz method for spin mixture obtained in Chapter 3. First, the Bethe ansatz, properly speaking for two-component spin mixtures with PBC in the configuration sector $x_1 < \dots < x_N$ reads [Li et al., 2003, Oelkers et al., 2006, Imambekov & Demler, 2006b]

$$\Psi(x_1, \dots, x_N) = \sum_{P \in S_N} A_P(\{k_i\}, \{\Lambda_m\}, c) e^{i \sum_j k_{P(j)} x_j}, \quad (5.52)$$

where $N = N_\downarrow + N_\uparrow$ is the total number of particles of spin denoted \downarrow and \uparrow , $A_P(\{k_i\}, \{\Lambda_m\}, c)$ the amplitudes depending on the N charge rapidities $\{k_i\}$ but also on the N_\downarrow spin rapidities $\{\Lambda_m\}$, and where the sum is performed over all the

possible permutations P in the symmetric group S_N . The two sets of rapidities fully specify the wave function of the system: they can be obtained for each value of $\tilde{\Phi}$ by solving the coupled Bethe equations [Li et al., 2003],

$$\begin{cases} Lk_j = 2\pi I_j + 2\eta_B \sum_{l=1}^N \arctan\left(\frac{k_l - k_j}{c}\right) - \sum_{m=1}^{N_\downarrow} \arctan\left(\frac{2(k_j - \Lambda_m)}{c}\right) \\ \sum_{j=1}^N \arctan\left(\frac{2(\Lambda_m - k_j)}{c}\right) = \pi J_m + \sum_{n=1}^{N_\downarrow} \arctan\left(\frac{2(\Lambda_m - \Lambda_n)}{c}\right) \end{cases}, \quad (5.53)$$

where we introduced the charge and spin Bethe quantum numbers I_j and J_m , which are integers or half integers depending on the partition of the mixture. The selection rules of the Bethe quantum numbers are summarized in Table 5.2. The choice of the quantum numbers defines the state of the system. In particular, in the ground state, adjacent quantum numbers are spaced by one unit. Moreover, similarly to identical particles, they are chosen such that the corresponding rapidities k_j minimize the energy E [Li et al., 2003, Imambekov & Demler, 2006a, Imambekov & Demler, 2006b].

Table 5.2: Selection rule for the Bethe quantum numbers of a $SU(2)$ fermionic and bosonic mixture with PBC [Yu & Fowler, 1992, Li et al., 2003]. For fermions N_\downarrow (resp. N_\uparrow) dictates the distribution of the I_j (resp. J_m) while for bosons, only N_\downarrow has to be considered.

	Fermions		Bosons	
Conditions	N_\downarrow even	N_\downarrow odd	N_\uparrow even	N_\uparrow odd
Selection rules	$I_j \in \mathbb{Z}$	$I_j \in \mathbb{Z} + 1/2$	$I_j \in \mathbb{Z} + 1/2$	$I_j \in \mathbb{Z}$
Conditions	N_\uparrow even	N_\uparrow odd	N_\uparrow even	N_\uparrow odd
Selection rules	$J_m \in \mathbb{Z} + 1/2$	$J_m \in \mathbb{Z}$	$J_m \in \mathbb{Z} + 1/2$	$J_m \in \mathbb{Z}$

Later on, we will consider the highly repulsive regime in which a spin-charge decoupling occurs in the wave function Equation (5.52). Precisely, in this case the amplitudes satisfy $\lim_{c \rightarrow \infty} A_P(\{k_i\}, \{\Lambda_m\}, c) = \tilde{A}_P(\{\lambda_m\}) = \epsilon(P)A_P(\{\lambda_m\})$ for fermions and $\lim_{c \rightarrow \infty} A_P(\{k_i\}, \{\Lambda_m\}, c) = A_P(\{\lambda_m\})$ for bosons. The presence or absence of the signature $\epsilon(P)$ only betrays the type of symmetry under the involved particle exchange. Moreover, the set of amplitudes $\{A_P(\{\lambda_m\})\}$ doesn't belong anymore to a particular configuration sector but effectively describes the whole space. Precisely, the wave function in a particular sector $x_{P(1)} < \dots < x_{P(N)}$ become in this limit

$$\Psi(x_1, \dots, x_N) = \tilde{A}_P(\{\lambda_m\}) e^{i \sum_j k_{P(j)} x_j}, \quad (5.54)$$

where now every $A_P(\{\lambda_m\})$ is attached to a given sector, and explicitly reads [Essler et al., 2005, Oelkers et al., 2006]

$$A_P(\{\lambda_m\}) \propto \sum_{Q \in S_{N_\downarrow}} \prod_{1 \leq m < n \leq N_\downarrow} \frac{\lambda_{Q(m)} - \lambda_{Q(n)} - 2i}{\lambda_{Q(m)} - \lambda_{Q(n)}} \prod_{l=1}^{N_\downarrow} \left(\frac{\lambda_{Q(l)} - i}{\lambda_{Q(l)} + i} \right)^{y_{P(l)}}, \quad (5.55)$$

where the integer $y_{P(l)}$ labels the position of the l -th spin down in the coordinate sector P .

Our ultimate goal is the symmetry analysis of the system. As presented in Chapter 3, this analysis can be performed using the class sum operators $\hat{\Gamma}^{[2]}$ and its eigenvalues $\gamma_{[\nu]}^{[2]}$, with $[\nu] = [\nu_1, \nu_2, \dots]$ corresponding to Young's diagrams, with ν_j boxes in the j -th line. We recall that these diagrams represent the overall symmetry of the state. Through their use, one can assign a well-defined symmetry to every state Ψ of the Hamiltonian Equation (5.51) by deriving the expectation values of $\hat{\Gamma}^{[2]}$ in these states. Therefore, to perform this symmetry analysis, we must obtain each eigenstate of our model - thus the rapidities and amplitudes. A thorough explanation of the method to acquire the explicit expression of the Bethe wave function has been provided in Chapter 3 and will therefore be skipped here. Instead, the complete derivation in the case of $1 + 1$, and $2 + 2$ mixture at large interaction has been provided.

5.2.2 Case of two particles

Before tackling the case of larger numbers of particles, it is instructive to understand the solution for $N = 2$ particles, i.e., one boson for each component of the mixture. When $N = 2$ and $N_{\downarrow} = 1$ there are only two coordinate sectors, namely $P_1 = \mathbb{1} : x_1 \leq x_2$ and $P_2 : x_2 \leq x_1$. Without loss of generality, we assume the positions of the spin-down particle in the two sectors to be $y_{\mathbb{1}} = 2$ and $y_{P_2} = 1$. We use Equation (5.55) to compute the amplitudes of the Bethe wave function

$$\begin{aligned} \tilde{A}_{\mathbb{1}}(\lambda) &\propto \left(\frac{\lambda - i}{\lambda + i} \right)^2, \\ \tilde{A}_{P_2}(\lambda) &\propto (-1) \left(\frac{\lambda - i}{\lambda + i} \right), \end{aligned} \tag{5.56}$$

where we used the property $\epsilon(\mathbb{1}) = 1$ and $\epsilon(P_2) = -1$. The Bethe equation for the spin rapidity λ reads

$$\arctan(\lambda) = \frac{\pi}{2}J, \quad J \in \mathbb{Z}. \tag{5.57}$$

In the ground state at zero flux, we have, to minimize the energy, $J = 0$ and $\tilde{A}_{\mathbb{1}}(0) = \tilde{A}_{P_2}(0) = 1$, while in the first excited state $J = 1$ and consequently $\tilde{A}_{\mathbb{1}}(\infty) = 1, \tilde{A}_{P_2}(\infty) = -1$. Next, to connect with the standard solutions in the fermionized limit, we decompose the wave function in each coordinate sector on a basis of anti-symmetric combinations of plane waves, as opposed to Equation (5.54). Consequently, we introduce the amplitudes $\mathcal{A} = \epsilon(Q)A_Q$. Explicitly, the wave function in this form reads

$$\Psi(x_1, x_2) = \mathcal{A}(x_1 - x_2) \det(e^{ik_j x_\ell}). \tag{5.58}$$

A simple reorganization of the terms entering in the above equation yields

$$\Psi(x_1, x_2) = \mathcal{A}(x_1 - x_2) \sin(k(x_1 - x_2)) e^{iK(x_1+x_2)/2}, \quad (5.59)$$

where $K = k_1 + k_2$ is the center of mass momentum and $k = (k_1 - k_2)/2$ is the relative momentum of the two-particle system. In the homogeneous ring, there is complete factorization between the internal structure of the state, encoded in the term $\mathcal{A}(x_1 - x_2) \sin k((x_1 - x_2))$, where $\mathcal{A}(x_1 - x_2)$ controls the overall symmetry under exchange of particles, and the center-of-mass part $\exp(iK(x_1 + x_2)/2)$. The latter is the one that couples to the artificial gauge flux [Manninen et al., 2012, Naldesi et al., 2022]. The corresponding value of the energy is $E = \sum_{j=1,2} (\hbar^2/2m)[k_j - (2\pi/L)\tilde{\Phi}]^2$.

The values of the wave vectors k_1, k_2 are obtained by imposing the periodic boundary conditions $\Psi(x_1 + L, x_2) = \Psi(x_1, x_2) = \Psi(x_1, x_2 + L)$. The function $\mathcal{A}(x_1 - x_2)$ for the ground state depends on the value of the artificial gauge field.

For $-0.25 < \tilde{\Phi} < 0.25$, the ground state of distinguishable bosons coincides with the one of identical TG bosons, i.e., $\mathcal{A}(x_1 - x_2) = \text{sign}(x_1 - x_2)$. In this case, the periodic boundary conditions imposed on Equation (5.58) yield $k_1 + k_2 = (2\pi/L)2p$ and $k_1 - k_2 = (2\pi/L)q$ with p, q integers. The solution for the ground state gives $k_1 = -\pi/L$ and $k_2 = \pi/L$.

Notice that thanks to the analogy of the Hamiltonian with one of the particles in a crystal with quasi-momentum $\tilde{\Phi}$, the same choice for $\mathcal{A}(x_1 - x_2)$ holds for all intervals of flux obtained by a translation of the interval $-0.25 < \tilde{\Phi} < 0.25$ by integer numbers, i.e., shifting $\tilde{\Phi}$ by integer multiples of Φ_0 .

For $0.25 < \tilde{\Phi} < 0.75$, the ground state is instead obtained by choosing $\mathcal{A}(x_1 - x_2) = 1$, as for spinless fermions. This corresponds to the Bethe ansatz solution for the wave function of the first excited state at zero flux. In this case, the periodic boundary conditions yield $k_1 = 0$ and $k_2 = 2\pi/L$. As above, the same choice for $\mathcal{A}(x_1, x_2)$ holds for all intervals of flux values obtained by translations of the considered interval by integer numbers.

By collecting all the above considerations, we obtain the ground-state energy as a flux function (see Figure 5.5): it consists of piece-wise parabolas, with half periodicity with respect to the flux quantum Φ_0 . We notice that each parabola is associated with a different total momentum value $P = \hbar(k_1 + k_2)$. Hence, of the total angular momentum L_z along the direction perpendicular to the ring plane. We label them by $\ell = \langle L_z \rangle / \hbar$, as also indicated in the figure, where $\langle L_z \rangle = PR$. We notice that the halved periodicity implies *fractional angular momentum per particle* as already reported for the case of attracting bosons [Naldesi et al., 2022], paired fermions [Bloch, 1973, Yu & Fowler, 1992, Pecci et al., 2021], and SU(N) fermionic mixtures [Chetcuti et al., 2022].

Our explicit solution also allows us to obtain the ground state's symmetry readily. The wave function is fully symmetric for the parabola centered at zero flux (and all its translations by Φ_0). In contrast, for the one centered at $\Phi_0/2$ (and all its translations by Φ_0) the wave function is fully anti-symmetric. The corresponding Young's diagrams are also depicted in Figure 5.5.

Let us summarize the four main aspects emerging from the analysis of the two-particle case: 1) the ground state of the mixture on a ring is not degenerate, as opposed to the case of a mixture under harmonic confinement [Volosniev et al., 2014], 2) piece-wise parabolas give the ground-state energy as a function of the flux,

each of them characterized by a given value of total angular momentum specified by ℓ , 3) each parabola has a well-defined symmetry (either fully symmetric or fully anti-symmetric), and 4) the case of a two-component mixture displays a halving of the periodicity with respect to the case of a spin-polarized Fermi gas (parabolas centered at semi-integer values of Φ_0) as well as the one of a single-component TG gas (parabolas centered at integer multiples of Φ_0).

In the following, we will treat the more challenging case of a 2 + 2 spin mixture.

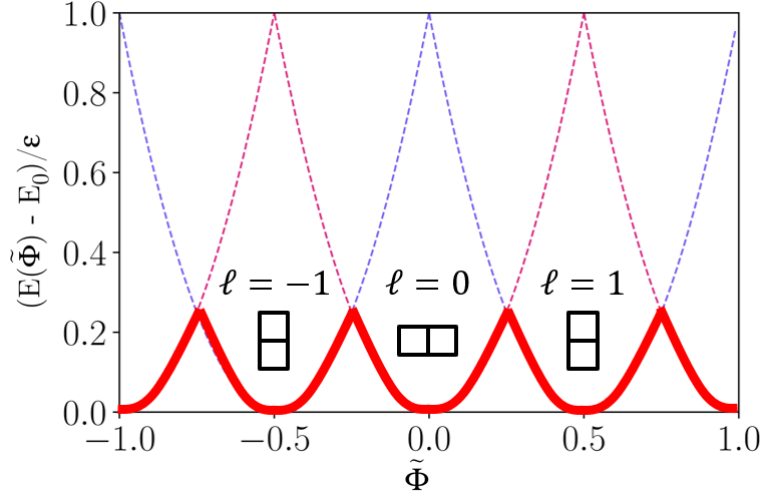


Figure 5.5: On the left, ground state energy (relative to the energy E_0 at zero flux, in units of ϵ) as a function of the reduced flux (dimensionless) for the case $N = 2$, $N_{\downarrow} = 1$ (red solid line). The violet and magenta dashed lines correspond to the energy landscape for $N = 2$ single-component TB and SF, respectively. The total angular momentum quantum number and the Young's diagram indicating the symmetry of the ground state under particle exchange are also indicated on each ground-state branch. Adapted from [Pecci et al., 2023].

5.2.3 Results for $N = 4$, $N_{\downarrow} = 2$

This section provides the results for a balanced multicomponent Bose gas of $N = 4$ particles and $N_{\downarrow} = 2$ spins down. The quantum numbers I_j and J_m are both semi-integers [Li et al., 2003]. We can write Equation (5.53) as follows

$$A_P(\lambda_1, \lambda_2) \propto \left(\frac{\lambda_1 - \lambda_2 - 2i}{\lambda_1 - \lambda_2} \left(\frac{\lambda_1 - i}{\lambda_1 + i} \right)^{y_{P(1)}} \left(\frac{\lambda_2 - i}{\lambda_2 + i} \right)^{y_{P(2)}} + \frac{\lambda_2 - \lambda_1 - 2i}{\lambda_2 - \lambda_1} \left(\frac{\lambda_2 - i}{\lambda_2 + i} \right)^{y_{P(1)}} \left(\frac{\lambda_1 - i}{\lambda_1 + i} \right)^{y_{P(2)}} \right). \quad (5.60)$$

The set of Bethe equations is

Table 5.3: Solutions of the Bethe equations for a strongly repulsive Bose-Bose mixture of $N = 4$ particles and $N_{\downarrow} = 2$ spin-down particles. We consider various values of total angular momentum P and quantum numbers configuration J_1, J_2 . Such solutions are the ground state and the first excited states for zero reduced flux $\tilde{\Phi}$ (see column $E(0)/\epsilon$) but become the ground state in a given interval of flux as indicated in the last column of the table.

P	$J_1 + J_2$	$\tilde{\lambda}_1$	$\tilde{\lambda}_2$	$E(0)/\epsilon$	Reduced flux interval
0	0	$1/\sqrt{3}$	$-1/\sqrt{3}$	10	$-1/8 \leq \tilde{\Phi} \leq 1/8$
0	0	$i\infty$	$-i\infty$	10	$-1/8 \leq \tilde{\Phi} \leq 1/8$
$2\pi/L$	1	-1	∞	21/2	$1/8 \leq \tilde{\Phi} \leq 3/8$
$4\pi/L$	2	0	∞	12	$3/8 \leq \tilde{\Phi} \leq 5/8$
$4\pi/L$	2	i	$-i$	12	$3/8 \leq \tilde{\Phi} \leq 5/8$
$6\pi/L$	3	1	∞	29/2	$5/8 \leq \tilde{\Phi} \leq 7/8$

$$\begin{cases} Lk_j = 2\pi I_j - \frac{2\pi}{4}(J_1 + J_2) \\ 8 \arctan(\lambda_1) = 2\pi J_1 - \arctan \frac{\lambda_2 - \lambda_1}{2} \\ 8 \arctan(\lambda_2) = 2\pi J_2 + \arctan \frac{\lambda_2 - \lambda_1}{2} \end{cases}, \quad (5.61)$$

which can be simplified using the trigonometric relation $\arctan(a) + \arctan(b) = \arctan\left(\frac{a+b}{1-ab}\right)$

$$\begin{cases} Lk_j = 2\pi I_j - \frac{2\pi}{4}(J_1 + J_2) \\ \frac{\lambda_1 + \lambda_2}{1 - \lambda_1 \lambda_2} = \tan\left(\frac{\pi}{4}(J_1 + J_2)\right) \\ 8 \arctan(\lambda_2) = 2\pi J_2 + \arctan \frac{\lambda_2 - \lambda_1}{2} \end{cases}, \quad (5.62)$$

In order to minimize the energy associated to the charge sector we have to minimize $\sum_j I_j$. As a consequence, the set of quantum numbers I_j for the ground state of the charge sector is $I_j = \{-\frac{3}{2}, -\frac{1}{2}, \frac{1}{2}, \frac{3}{2}\}$. Moreover, due to the periodicity of the tangent function, the second equation only gives independent solutions for $(J_1 + J_2) \pmod{4}$. Therefore, we can focus on the four cases $J_1 + J_2 = 0, 1, 2, 3$, which, for each value of $\tilde{\Phi}$, correspond to respectively the ground state and the first three excited states. Explicitly, these configurations yield the following values for the total momentum $P = 0, \frac{2\pi}{L}, \frac{4\pi}{L}, \frac{6\pi}{L}$. The solutions of Equation (5.62) are listed in Table 5.3. Remarkably, if we allow for complex λ_n , multiple solutions can be associated with the same momentum value. We define $a_Q^{\ell,i} = A_Q(\tilde{\lambda}_1^i(P), \tilde{\lambda}_2^i(P))$ as the amplitudes of the Bethe wave function for each configuration of quantum numbers and where $\tilde{\lambda}_{1,2}^i(P)$ are the i -th solutions of the last two Bethe equations (5.62) for a fixed value of the total momentum P , labeled by the quantum number ℓ . In particular, we get two solutions for $P = 0$ and $P = 4\pi/L$, while for $P = 2\pi/L$ and $P = 6\pi/L$, the solution is unique. We also stress that in order to get all the possible low-energy excitations, we had to include singular solutions of the Bethe equations [Nepomechie & Wang, 2013, Kirillov & Sakamoto, 2014].

In Table 5.4, we show all the possible $a_Q^{\ell,i}$ for this case in the different coordinate sectors, defined by the possible spin orderings. We get six possible solutions, which

Table 5.4: Amplitudes $a_Q^{\ell,i}$ corresponding to the different spin sectors for $N = 4$ and $N_\downarrow = 2$.

Sector	$a_Q^{(0,1)}$	$a_Q^{(0,2)}$	$a_Q^{(1,1)}$	$a_Q^{(2,1)}$	$a_Q^{(2,2)}$	$a_Q^{(3,1)}$
$ \uparrow\uparrow\downarrow\downarrow\rangle$	2	2	$1 - i$	0	2	$1 + i$
$ \uparrow\downarrow\uparrow\downarrow\rangle$	-4	2	0	2	0	0
$ \downarrow\uparrow\uparrow\downarrow\rangle$	2	2	$1 + i$	0	-2	$1 - i$
$ \uparrow\downarrow\downarrow\uparrow\rangle$	2	2	$-1 - i$	0	-2	$-1 + i$
$ \downarrow\uparrow\downarrow\uparrow\rangle$	-4	2	0	-2	0	0
$ \downarrow\downarrow\uparrow\uparrow\rangle$	2	2	$-1 + i$	0	2	$-1 - i$

correspond to six different states. This value coincides with the possible and distinguishable spin configurations allowed in this case, given in general by $\frac{N!}{N_\downarrow!(N-N_\downarrow)!}$.

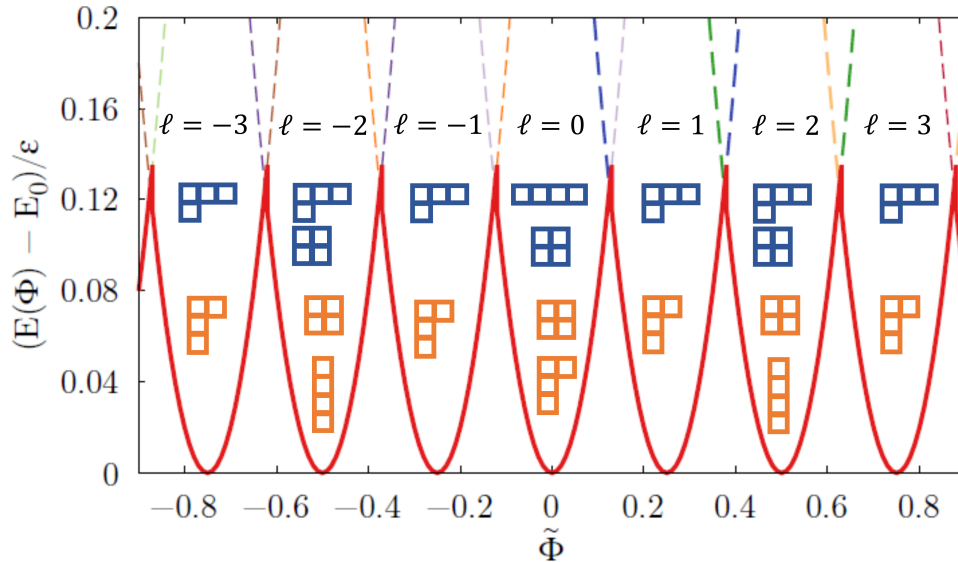


Figure 5.6: Top panel: energy levels (relative to the energy E_0 at zero flux, in units of ϵ) as a function of the reduced flux (dimensionless) for both a bosonic and a fermionic mixture with $N = 4$ and $N_\downarrow = 2$. The red continuous line highlights the ground state of the system. For each flux value, we indicate the angular momentum quantum number of the ground state. The two upper lines of Young's diagrams (blue diagrams) indicate the symmetry of the bosonic ground state as a flux function. The two bottom lines (orange diagrams) are the ones of the fermionic ground state. Adapted from [Pecci et al., 2023].

Looking at Figure 5.6, we see that each time the flux increases by $\tilde{\Phi}/N$, the ground state carries a different value of total momentum P .

We evaluated the symmetry of the states listed in Table 5.4 by computing the expectation value $\langle a^{\ell,i} | \Gamma_2 | a^{\ell,i} \rangle$, $|a^{\ell,i}\rangle$ being the vector collecting the coefficients $a_Q^{\ell,i}$ in the different coordinate sectors for the i -th state of total momentum P (i.e the columns of Table 5.4), suitably normalized. For each of the above states, this expectation value coincides with an eigenvalue of the class-sum operator Γ_2 , i.e., each

state has well-defined symmetry. This allows us to link them to a Young's diagram and, therefore, for any value of the reduced flux, to determine the symmetry of the ground state. In the top panel of Figure 5.6, the upper line (blue) of diagrams provides the symmetry of the ground state for each branch of the ground-state energy as a function of the flux.

It is instructive to compare our results for the Bose-Bose mixture with the ones for a Fermi-Fermi mixture with repulsive contact inter-component interactions. In this case, the wave function still has the form Equation (5.54). However, the Bethe equations are different since there is no contact interaction among fermions belonging to the same component, and the symmetry under exchanges of particles belonging to the same component is different. At strong repulsive interactions, the first Bethe equations (5.53) reads $Lk_j = 2\pi\left(I_j + \frac{1}{N}\sum_{m=1}^M J_m\right)$ while the equation for the spin rapidities coincides with the one for the bosonic case [Yu & Fowler, 1992, Chetcuti et al., 2022]. The results for the solutions of the Bethe equations for the fermionic case are summarized in Table 5.5. In this case the quantum numbers I_j for $N = 4$ and $N_\downarrow = 2$ are integers [Oelkers et al., 2006]. In the ground state, we have $I_j = \{-2, -1, 0, 1\}$ which implies $\sum_j I_j = -2$. The total momentum for the Fermi-Fermi mixture is $P_F = \frac{2\pi\hbar}{L}\left(\sum_j I_j + \sum_a J_a\right) \doteq \frac{\hbar}{R}\ell_F$ [Ogata & Shiba, 1990, Essler et al., 2005, Chetcuti et al., 2022]. The energy levels as a function of the flux are the same as for the Bose-Bose mixture. Similarly, for a given value of $\tilde{\Phi}$, the angular momentum of the ground state is the same for bosons and fermions.

On the other hand, the symmetry of the ground state is markedly different in the two cases. We evaluate the symmetry of the fermionic ground-state wave function by following the same procedure used for the bosonic system. Since the Bethe equation for the spin rapidities is the same as in the bosonic case, the fermionic amplitudes satisfy $a_Q^{\ell_F, j} = a_Q^{(\ell-2)(\text{mod}4), j}$, where ℓ_F labels fermionic states with different angular momentum. Consequently, the same value of the total momentum P_F is associated with distinct spin rapidities in the two cases and, therefore, to different amplitudes A_P . As the amplitudes affect the symmetry of the wave function, the corresponding Young's diagrams are different in the fermionic and the bosonic case. The Young's diagrams indicating the fermionic ground state's symmetries as a flux function are displayed in orange in the top panel of Figure 5.6.

We also remark that - both in the case of bosonic and fermionic mixtures - different parabolas display different symmetries, reflecting that they correspond to separate excited states at zero flux.

Let us emphasize the fact that we are considering a two-component system, and thus, different symmetries are possible. We remind that for the case of a single-component gas, also for the case of $N = 4$ particles, the energy landscapes are those shown in the right panels of Figure 5.5 (top panel for the TG gas and bottom panel for spinless fermions).

5.2.4 Concluding remarks

In this study, we have investigated the properties of 1D spin mixtures at large interaction with PBC and, in the presence of an external flux, up to 4 particles. We first obtained the general wave function via Bethe ansatz by carefully selecting the

Table 5.5: Solutions of the Bethe equations for a strongly repulsive Fermi-Fermi mixture for $N = 4$, $N_{\downarrow} = 2$, and various values of total momentum P_F . We also provide the energy associated with each state at zero flux and the reduced flux interval where each state becomes the ground state.

P_F	$J_1 + J_2$	$\tilde{\lambda}_1$	$\tilde{\lambda}_2$	$E(0)/\epsilon$	Reduced flux interval
0	2	0	∞	10	$-1/8 \leq \tilde{\Phi} \leq 1/8$
0	2	i	$-i$	10	$-1/8 \leq \tilde{\Phi} \leq 1/8$
$2\pi/L$	3	1	∞	21/2	$1/8 \leq \tilde{\Phi} \leq 3/8$
$4\pi/L$	4	$\frac{1}{\sqrt{3}}$	$-\frac{1}{\sqrt{3}}$	12	$3/8 \leq \tilde{\Phi} \leq 5/8$
$4\pi/L$	4	∞	∞	12	$3/8 \leq \tilde{\Phi} \leq 5/8$
$6\pi/L$	5	-1	∞	29/2	$5/8 \leq \tilde{\Phi} \leq 7/8$

physical solutions of the Bethe equations. This task successfully fulfilled allowed for a $SU(2)$ symmetry analysis via the class-sum method. In parallel, we have computed the spectrum of various mixtures to aid in interpreting the impact of the flux on different states and their symmetry.

This joint analysis has provided various outcomes. First, we have shown that the spectrum of a spin mixture with an artificial gauge is composed of parabolas, each corresponding to a particular spin excited state. We have found the ground state energy to be periodic with the flux Φ and the excited states with fractions of Φ . This $1/N$ fractionalization of the periodicity, as compared to the non-interacting case, is understood as an interplay between Φ and the excited states. Precisely, by applying an overall Φ , the states originally above the ground state see their energy decreasing at its level but in a different range of reduced flux $\tilde{\Phi}$. The second crucial result comes from the symmetry analysis. In particular, we have been able to assign well-defined symmetries to each parabola.

Furthermore, our study delved into the symmetry of particle exchange in ground-state branches, specifically about flux. Our findings indicate that a non-degenerate branch corresponds to a singular Young's diagram. Conversely, if the ground state is degenerate, multiple diagrams may be observed. This analysis confirms that spin excitations are responsible for the reduction in periodicity and the appearance of novel parabolic branches, which are absent in the non-interacting regime.

The fact that a particular symmetry state could be linked with a given flux is remarkable. This is an engaging feature in order to build an experimental setup to select the symmetry state of spin mixtures.

Conclusion

Along with this thesis, we have investigated the correlations and symmetry properties of 1D ultracold atomic gases with contact interactions between them. We have carried a particular interest in spin mixtures throughout their long- and short-distance correlation behavior and the notion of $SU(\kappa)$ symmetry.

In Chapter 3 we have conducted a thorough study of the short-distance properties of gases in a 1D box-shaped trap. We have begun with the simple yet insightful example of spinless fermions and Tonks-Girardeau bosons, which have unveiled the presence of unexpected terms in the $1/k^4$ coefficient of the momentum distribution tail. In particular, we have demonstrated the presence of an additional constant and oscillating contribution generated by the hard walls of the potential. This curious phenomenon has motivated us to push our analysis toward the more involving case spin mixtures, allowing a deeper understanding of these new contributions. We learned that the constant term resulted from the wave function's accommodation to the boundary conditions. At the same time, we understood that the one-spin coherence was mediating the oscillatory term between the same particle at the edges of the trap. The latter has the important effect that spin coherences are carried by these oscillations, opening new protocols to probe spin states of 1D systems. Relying on this discovery, we have proposed a method to probe the ground state of a bosonic spin mixture.

In the first section of Chapter 5, we have incorporated the $SU(\kappa)$ analysis into our investigation of spin mixtures via the class-sum method. Our team considered a model to investigate the $SU(2)$ symmetry of a bosonic spin mixture in a controlled setup and an experimental protocol for its implementation. Since the Hamiltonian governing the system is integrable, we obtained the corresponding exact wave function to conduct both a symmetry analysis and an exploration of the correlations. This ansatz has enabled both the symmetry analysis and the investigation of the correlations of this new system. Our findings revealed that the ground state of a spin mixture no longer has a single well-defined symmetry but rather becomes a mixture of different symmetries. This state can be assimilated as the ground state of a fermionic mixture, which has been ultimately symmetrized. We have also explored the effect of the SB on the long- and short-distance correlations. Even if the symmetry is weakly broken, we have demonstrated that it tremendously impacts the system's long-distance coherence, halving the related observable: the zeroth- k mode occupation. The effect is so important enough to be observed experimentally, furnishing a convenient way to confirm if the system has realized a $SU(2)$ symmetry breaking.

In parallel with this work, I developed an exact expression for the n -th order

correlation function and the equivalent of the Lenard form of the first-order correlation (both for $SU(\kappa)$ spin mixture at large interaction). I already have preliminary results, which have not been included in the present document. This analysis of higher-order correlations is of particular importance and could allow, for instance, for full counting statistics obtaining. In contrast, the Lenard-like form of the first-order correlation function, which is extremely efficient for short-distance analysis, could provide an exact expression for Tan's contact in complex configurations, such as the $SU(\kappa)$ symmetry breaking case.

In Chapter 5, we have also moved to a slightly more challenging model where spin mixtures are trapped in a ring-shaped trap. Through the Bethe ansatz method, we have carefully acquired the exact wave function and examined its $SU(\kappa)$ symmetries. In parallel, we have derived the system's spectrum as a function of the overall flux within the ring. This joint analysis has allowed us to characterize the symmetry of each spectrum's regions and, by then, helped to explain its structure.

The versatility of 1D cold atomic spin mixtures offers many possibilities to improve our results. Among all the perspectives, some were revealed to be of particular interest. In Chapter 4 we have already evoked the dynamics of our systems. This type of generalization must be seen as one of the principal outlooks of the works done in this thesis. One can think, for instance, to obtaining the spectral function of spin mixtures. Besides, the thermodynamic properties are also particularly thrilling. Indeed, our systems are integrable and realizable in many configurations, so they could serve as an experimental platform to study the eigenvalue thermalization hypothesis. One can also think of the disorder properties of such a system, for instance, through localization. Naturally, we can consider more exotic systems both in terms of mixtures and trapping geometry. For the former, the question of Bose-Fermi or anyonic mixtures is relevant. For the latter, we know that the method we call Volosniev works for any type of trapping geometry as long as we know the natural orbital so correlation functions are accessible in a huge variety of configurations.

In parallel, we have demonstrated in Chapter 5 (through a commutator problem) that any arbitrary trapping geometry can realize an $SU(\kappa)$ symmetry, so $SU(\kappa)$ symmetry analysis can be realized even for random or time-dependent trapping. On the symmetry side, many other aspects must be investigated more deeply. For example, the other kind of complete set of commuting observable of S_n and what information they could convey. To conclude, one important question related to the spectrum remains unanswered: why do some states with the same overall symmetry (i.e., Young's diagrams) have different energies? This feature clearly points toward a hidden property of the system, and understanding what drives this ordering could naturally add another layer of insight into these mixtures.

Appendix A

Derivation of the Volosniev matrix

A.1 The nearest-neighbor exchange constant

To simplify the expression of the slope, we will demonstrate what became the α_k 's in a homogeneous configuration. With this updated form, we will derive the thermodynamic limit of Equation (3.21) in the case of PBC and, as the two are similar, only present the result for DBC.

In a sense, the α_k 's quantify the preferred particle positions within the trap. However, when the potential is uniform throughout the trap, there is no preference for a specific position. Consequently, all α_k 's values should be equal, so we can set $\alpha_k = \alpha_N$ and adjust Equation (3.21) accordingly

$$\alpha_N = N! \int_{x_1 < \dots < x_N} dx_1 \dots dx_N \delta(x_1 - x_2) \left| \frac{\partial \Psi_{SF}}{\partial x_1} \right|^2. \quad (\text{A.1})$$

Let us investigate what became this expression for PBC and DBC.

A.1.1 α_N in the ring

While dealing with PBC, the Equation (A.1) formulation of the nearest-neighbor exchange constant becomes ill-defined. The boundary condition imposes for every ordering to loop, which results in Γ_{Id} to have the form $x_1 < \dots < x_N < x_1$. Writing the sector this way may suggest that the integration domain has no dimension. However, we can overcome this issue by treating one of the variables (in this case, x_1) as a moving boundary for the other $(N-1)$ variables. The corresponding domain is actually N times larger than Γ_{Id} and leads to the ensuing expression [Aupetit-Diallo et al., 2022]

$$\alpha_N^R = (N-1)! \int_0^L dx_1 \prod_{i=2}^N \int_{x_{i-1}}^{x_1+L} dx_i \delta(x_1 - x_2) \left| \frac{\partial \Psi_{SF}}{\partial x_1} \right|^2. \quad (\text{A.2})$$

We acknowledge Martial Morisse and Manon Ballu for the idea of redefining α_N in these terms.

To solve this new formulation, let us express the spinless fermions wave function under a Leibnitz determinant form

$$\Psi_{SF}(x_1, \dots, x_N) = \frac{1}{\sqrt{N!}} \sum_{P \in S_N} \epsilon(P) \prod_{n=1}^N \phi_{P(n)}(x_n), \quad (\text{A.3})$$

and rewrite the natural orbitals for PBC in a suitable way

$$\phi_m(x_n) = e^{ik_n^\infty x_n} / \sqrt{L}, \quad (\text{A.4})$$

with the $k_n^\infty = \pi I_n / L = \pi(2n - N - 1) / L$, for $n = 1, \dots, N$. Thus, for Equation (A.2) it follows

$$\begin{aligned} \alpha_N^R &= \frac{1}{N! L^N} \sum_{P, Q \in S_N} \epsilon(P) \epsilon(Q) \int_0^L dx_1 \left[\frac{\partial \phi_{P(1)}(x_1)}{\partial x_1} \cdot \frac{\partial \phi_{Q(1)}^*(x_1)}{\partial x_1} \cdot \phi_{P(2)}(x_1) \phi_{Q(2)}^*(x_1) \right] \\ &\times \int_{x_1}^{x_1+L} dx_3 \phi_{P(3)}(x_3) \phi_{Q(3)}^*(x_3) \prod_{n=3}^{N-1} \int_{x_n}^{x_n+L} dx_{n+1} \phi_{P(n+1)}(x_{n+1}) \phi_{Q(n+1)}^*(x_{n+1}) \end{aligned} \quad (\text{A.5})$$

$$\begin{aligned} &= \frac{1}{N! L^N} \sum_{P, Q \in S_N} \epsilon(P) \epsilon(Q) k_{P(1)}^\infty k_{Q(1)}^\infty \int_0^L dx_1 e^{i\pi(\Delta I_1 + \Delta I_2)x_1/L} \int_{x_1}^{x_1+L} dx_3 e^{i\pi \Delta I_3 x_3/L} \\ &\times \prod_{n=3}^{N-1} \int_{x_n}^{x_n+L} dx_{n+1} e^{i\pi \Delta I_{n+1} x_{n+1}/L}, \end{aligned} \quad (\text{A.6})$$

with $\Delta I_n = I_{P(n)} - I_{Q(n)} = 2(P(n) - Q(n))$. Here, we will present a conjecture regarding the result of the previous integral. Through formal computation, we have verified the following expression up to $N = 6$, this one reads

$$\begin{aligned} \alpha_N^R &= \frac{1}{N(N-2)!L} \sum_{P, Q \in S_N} \epsilon(P) \epsilon(Q) k_{P(1)}^\infty k_{Q(1)}^\infty \delta_{P(1)+P(2)}^{Q(1)+Q(2)} \prod_{n=3}^N \delta_{P(n)}^{Q(n)} \\ &= \frac{1}{N(N-2)!L} \sum_{P, Q \in S_N} [(k_{P(1)}^\infty)^2 - k_{P(1)}^\infty k_{Q(2)}^\infty] \prod_{n=3}^N \delta_{P(n)}^{Q(n)} \\ &= \frac{1}{N(N-2)!L} \sum_{P \in S_N} [(k_{P(1)}^\infty)^2 - k_{P(1)}^\infty k_{P(2)}^\infty]. \end{aligned} \quad (\text{A.7})$$

This result is believed to be robust as no new types of nested integrals arise in Equation (A.6) for $N \geq 4$. With the precedent formulation, the solution is quite direct. Only two elements remain free in this sum, $P(1)$ and $P(2)$, so the sum over P boils down to $(N-2)!$ identical sums over two sets of N ordered elements

$$\alpha_N^R = \frac{1}{N!} \sum_{n, m=1}^N [(k_n^\infty)^2 - k_n^\infty k_m^\infty]. \quad (\text{A.8})$$

Finally, using the symmetry of the k_i^∞ one can find a condensed form for the nearest-neighbor exchange constant

$$\alpha_N^R = \frac{1}{L} \sum_{n=1}^N (k_n^\infty)^2. \quad (\text{A.9})$$

This result was already found in [Barfknecht et al., 2021], but no explanation was provided. Moreover, such simplification appears to be a general property of 1D UCAG at large repulsion and can also be observed in DBC, for instance. Finding the thermodynamic limit is then straightforward

$$\begin{aligned} \sum_{n=1}^N (k_n^\infty)^2 &= \frac{2\pi^2}{L^2} \left(\sum_{n=0}^{N/2-1} 4n^2 + \sum_{n=0}^{N/2-1} 4n + \frac{N}{2} \right) \\ &= \frac{N(N^2 - 1)}{3L^2} \pi^2, \end{aligned} \quad (\text{A.10})$$

which leads to the nearest-neighbor exchange constant thermodynamic limit in the presence of PBC to reads as follows [Aupetit-Diallo et al., 2022]

$$\alpha_N^R = \frac{N(N^2 - 1)}{3L^3} \pi^2. \quad (\text{A.11})$$

We will now present the same outcome obtained in DBC.

A.1.2 α_N in the box

Integrating on a moving boundary will be inefficient for a system not invariant by translation. Thus, we need a slightly different treatment for the box. Here the idea is to extend the domain Γ_{1d} from $x_1 < x_2 < \dots < x_N$ to $0 < x_1 < L \cup_{k=1, k \neq 2}^{N-1} x_k < x_{k+1} < L$. Noticing that this new domain is $(N - 2)!$ time larger we find [Aupetit-Diallo et al., 2023]

$$\alpha_N^B = \frac{N!}{(N - 2)!} \int_0^L dx_1 \left(\prod_{i=1, i \neq 2}^{N-1} \int_{x_i}^L dx_{i+1} \right) \left| \frac{\partial \Psi}{\partial x_1} \right|^2. \quad (\text{A.12})$$

This approach is a variation of the method described in [Decamp et al., 2016a], designed explicitly for homogeneous systems. It allows for the determination of the nearest-neighbor exchange constant in the thermodynamic limit, taking into account the presence of DBC. The resulting expression is as follows [Aupetit-Diallo et al., 2023]

$$\alpha_N^B = \frac{N(N + 1)(2N + 1)}{6L^3} \pi^2. \quad (\text{A.13})$$

We have gathered all the elements for building the Volosniev matrix and can proceed.

A.2 Construction of the Volosniev matrix

Before presenting the recipe for building the V matrix, let us take a closer look at the basis where it lives. Based on the Equation (3.28) that defines our eigenproblem, the a_P vectors, where P indexes the snippets as defined by K in Equation (3.22), constitute the basis we're looking for. Thereby, these $D = N! / \prod_{\sigma} N_{\sigma}!$ snippets - or independent spin sectors - must form the basis for the Volosniev matrix. Let's explicitly write it out for a $2 + 2$ mixture with $\sigma = (\uparrow, \downarrow)$ to clarify this basis. In this scenario, the snippet basis is as follows

$$\{|\uparrow\uparrow\downarrow\downarrow\rangle_1, |\uparrow\downarrow\uparrow\downarrow\rangle_2, |\uparrow\downarrow\downarrow\uparrow\rangle_3, |\downarrow\uparrow\uparrow\downarrow\rangle_4, |\downarrow\uparrow\downarrow\uparrow\rangle_5, |\downarrow\downarrow\uparrow\uparrow\rangle_6\}, \quad (\text{A.14})$$

where we have labeled the vectors to facilitate the incoming calculation of the element $[V]_{i,j}$. Moreover, let us recall the expression of the Volosniev matrix

$$[V^{SU}]_{i,j} = \begin{cases} \sum_{d,k \neq i} \alpha_{i,k} + 2 \sum_{b,k \neq i} \alpha_{i,k} & k = i \\ -\alpha_{i,j} & k \neq i \end{cases}, \quad (\text{A.15})$$

where the d -sum has to be taken over snippets k that transpose distinguishable particles, while the b -sum involves snippets that transpose identical bosons. Now that these definitions have been set, let us dissect the example of $2 + 2$ mixtures of fermions and bosons in the box and give their equivalent in the ring to witness their discrepancies.

$2 + 2$ mixture in the box

To proceed, we will apply the permutation operator $P_{i,i+1}$ (with $i = 1, \dots, N - 1$) to each snippet and rely on the state labeling chosen in (B.4). As a remark, the Volosniev matrix is symmetric, so in principle, we just have to compute the upper triangle to construct V entirely. Nonetheless, for the sake of this discussion, we will provide the full derivation for the upper half of the matrix. To begin, let us take the first vector $|\uparrow\uparrow\downarrow\downarrow\rangle$. For fermions, only exchanges of distinguishable particles count, as no contact potential is present for identical fermions. Then, we just have to consider P_{23} , as P_{12} and P_{34} act as identity. It follows $P_{23} |\uparrow\uparrow\downarrow\downarrow\rangle = |\uparrow\downarrow\uparrow\downarrow\rangle$ which is the second vector of the basis. Thus, the element $[V]_{1,2} = -\alpha_4$ and $[V]_{1,3} = [V]_{1,4} = [V]_{1,5} = [V]_{1,6} = 0$. Moreover, because there is one snippet accessible via $P_{i,i+1}$, the first diagonal element reads $[V]_{1,1} = 1 \times \alpha_4$. We can repeat the same procedure for the rest of the basis. Hence with the second vector

$$P_{i,i+1} |\uparrow\downarrow\uparrow\downarrow\rangle = \begin{cases} \xrightarrow{P_{12}} |\uparrow\downarrow\uparrow\downarrow\rangle \implies [V]_{2,4} = -\alpha_4 \\ \xrightarrow{P_{23}} |\uparrow\uparrow\downarrow\downarrow\rangle \implies [V]_{2,1} = -\alpha_4 \\ \xrightarrow{P_{34}} |\uparrow\downarrow\downarrow\uparrow\rangle \implies [V]_{2,3} = -\alpha_4 \end{cases}, \quad (\text{A.16})$$

which imply for the second diagonal element to be $[V]_{2,2} = 3 \times \alpha_4$. Similarly, for the third vector

$$P_{i,i+1} |\uparrow\downarrow\downarrow\uparrow\rangle = \begin{cases} \xrightarrow{P_{12}} |\downarrow\uparrow\downarrow\uparrow\rangle \implies [V]_{3,5} = -\alpha_4 \\ \xrightarrow{P_{34}} |\uparrow\downarrow\uparrow\downarrow\rangle \implies [V]_{3,2} = -\alpha_4 \end{cases}, \quad (\text{A.17})$$

which implies that the third diagonal element should be $[V]_{3,3} = 2 \times \alpha_4$. We will conclude the derivation at this point and provide the complete matrix, as the remaining steps are identical and could be obtained by symmetry. Thereby, the Volosniev matrix for $2 + 2$ fermions and DBC reads

$$V_{2F+2F}^{Box} = \alpha_4 \begin{pmatrix} 1 & -1 & 0 & 0 & 0 & 0 \\ -1 & 3 & -1 & -1 & 0 & 0 \\ 0 & -1 & 2 & 0 & -1 & 0 \\ 0 & -1 & 0 & 2 & -1 & 0 \\ 0 & 0 & -1 & -1 & 3 & -1 \\ 0 & 0 & 0 & 0 & -1 & 1 \end{pmatrix}, \quad (\text{A.18})$$

where the eigenvalues and eigenvectors are presented in Table A.1.

Table A.1: Rescaled eigenvalues K_i/α_4 and eigenvectors $|a_P\rangle_i$ of V_{2F+2F}^{Box} , with i the excitation level.

K_i/α_4	$ a_P\rangle_i$
4.73	$(1, -2 - \sqrt{3}, 1 + \sqrt{3}, 1 + \sqrt{3}, -2 - \sqrt{3}, 1)$
3.41	$(-1, 1 + \sqrt{2}, 0, 0, -1 - \sqrt{2}, 1)$
2	$(0, 0, -1, 1, 0, 0)$
1.27	$(1, -2 + \sqrt{3}, 1 - \sqrt{3}, 1 - \sqrt{3}, -2 + \sqrt{3}, 1)$
0.58	$(-1, 1 - \sqrt{2}, 0, 0, -1 + \sqrt{2}, 1)$
0	$(1, 1, 1, 1, 1, 1)$

Fortunately, we do not have to restart the derivation from scratch for a bosonic mixture with the same composition, as the only difference lies in the diagonal elements. For instance, the first vector $|\uparrow\uparrow\downarrow\downarrow\rangle$ has two types neighboring identical bosons, and $[V]_{1,1}$ must be heightened by an additional $+4\alpha_4$ term. On its side, the second vector, $|\uparrow\downarrow\uparrow\downarrow\rangle$, does not present neighboring identical bosons, so $[V]_{2,2}$ is identical to fermions. By continuing this process, we obtain the matrix for a $2 + 2$ bosonic mixture in the presence of DBC

$$V_{2B+2B}^{Box} = \alpha_4 \begin{pmatrix} 5 & -1 & 0 & 0 & 0 & 0 \\ -1 & 3 & -1 & -1 & 0 & 0 \\ 0 & -1 & 4 & 0 & -1 & 0 \\ 0 & -1 & 0 & 4 & -1 & 0 \\ 0 & 0 & -1 & -1 & 3 & -1 \\ 0 & 0 & 0 & 0 & -1 & 5 \end{pmatrix}, \quad (\text{A.19})$$

like fermions, the eigenvalues, and eigenvectors can be found in Table A.2.

Table A.2: Rescaled eigenvalues K_i/α_4 and eigenvectors $|a_P\rangle_i$ of V_{2B+2B}^{Box} , with i the excitation level.

K_i/α_4	$ a_P\rangle_i$
6	(1, -1, 1, 1, -1, 1)
5.41	(-1, -1 + $\sqrt{2}$, 0, 0, 1 - $\sqrt{2}$, 1)
4.73	(1, 2 - $\sqrt{3}$, 1 - $\sqrt{3}$, 1 - $\sqrt{3}$, 2 - $\sqrt{3}$, 1)
4	(0, 0, -1, 1, 0, 0)
2.58	(-1, -1 - $\sqrt{2}$, 0, 0, 1 + $\sqrt{2}$, 1)
1.26	(1, 2 + $\sqrt{3}$, 1 + $\sqrt{3}$, 1 + $\sqrt{3}$, 2 + $\sqrt{3}$, 1)

We can now discuss the outcomes of the Volosniev matrix in the ring.

2 + 2 mixture in the ring

The treatment of PBC in the Volosniev formalism is highly close to DBC. For instance, the expression of the recipe presented Equation (A.15) remains unchanged. The only difference is that now particles 1 and N are in contact, leading to additional sectors' connexion. These new connexions introduce supplementary non-zero elements to the Volosniev matrix, which now reads for 2 + 2 fermionic mixtures with PBC

$$V_{2F+2F}^{Ring} = \alpha_4 \begin{pmatrix} 2 & -1 & 0 & 0 & -1 & 0 \\ -1 & 4 & -1 & -1 & 0 & -1 \\ 0 & -1 & 2 & 0 & -1 & 0 \\ 0 & -1 & 0 & 2 & -1 & 0 \\ -1 & 0 & -1 & -1 & 4 & -1 \\ 0 & -1 & 0 & 0 & -1 & 2 \end{pmatrix}, \quad (\text{A.20})$$

and for 2 + 2 bosonic mixture with PBC

$$V_{2B+2B}^{Ring} = \alpha_4 \begin{pmatrix} 6 & -1 & 0 & 0 & -1 & 0 \\ -1 & 4 & -1 & -1 & 0 & -1 \\ 0 & -1 & 6 & 0 & -1 & 0 \\ 0 & -1 & 0 & 6 & -1 & 0 \\ -1 & 0 & -1 & -1 & 4 & -1 \\ 0 & -1 & 0 & 0 & -1 & 6 \end{pmatrix}. \quad (\text{A.21})$$

The eigenvalues and eigenvectors for these two matrices are presented in Table A.3.

Table A.3: Rescaled eigenvalues K_i/α_4 and eigenvectors $|a_P\rangle_i$ of V_{2+2}^{Ring} , with i the excitation level of the state for (left) $2 + 2$ fermions (right) $2 + 2$ bosons.

$2F + 2F$		$2B + 2B$	
K_i/α_4	$ a_P\rangle_i$	K_i/α_4	$ a_P\rangle_i$
6	(1,-2,1,1,-2,1)	8	(1,-1,1,1,-1,1)
4	(0,-1,0,0,1,0)	6	(-1,0,0,0,0,1)
2	(-1,0,0,0,0,1)	6	(-1,0,0,1,0,0)
2	(-1,0,0,1,0,0)	6	(-1,0,1,0,0,0)
2	(-1,0,1,0,0,0)	4	(0,-1,0,0,1,0)
0	(1,1,1,1,1,1)	2	(1,2,1,1,2,1)

To conclude this brief showcase of ring geometry, we want to emphasize that only the ground and most excited states correspond to exact physical states, as every other state could include phases.

Appendix B

$SU(2)$ symmetry analysis of a $2 + 2$ mixture in the box

In this appendix, we will detail the procedure that allows us to assign a well-defined symmetry to the physical state of a $SU(\kappa)$ Hamiltonian \hat{H}_{SU} . First of all, let us recall the Hamiltonian governing our system at large interaction in the presence of DBC [Deuretzbacher et al., 2014]

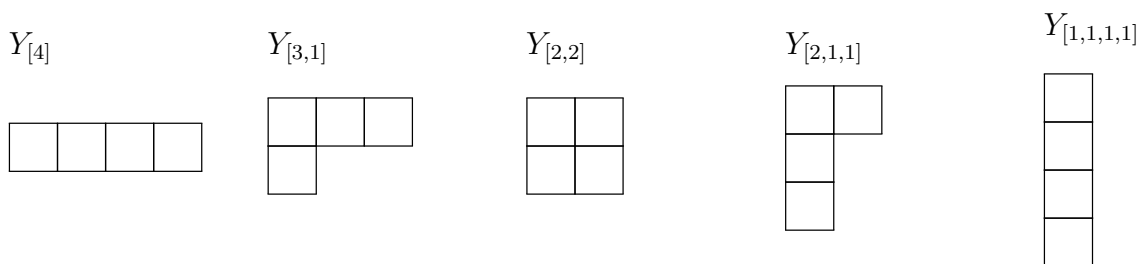
$$\hat{H}_P = (E_F - (N - 1))J_N \mathbb{1} \pm J_N \sum_{j=1}^{N-1} \hat{P}_{j,j+1}, \quad (\text{B.1})$$

where the + (resp. -) sign stands for fermions (resp. bosons). The eigenstates of \hat{H}_P will be referred to as $|a_P\rangle$. In the case of $2 + 2$ mixtures of bosons and fermions, we have already obtained these states and gathered them in Table A.1 and A.2 of Appendix A.2.

To determine the symmetries of these states, we will follow the steps described in the Section 3.3 of the main document.

B.1 Derivation of the $\gamma_{[\nu]}^{[r]}$ and dimension of the CSCO

For this initial step, the aim is to obtain the central characters $\gamma_{[\nu]}^{[r]}$ for every irrep. of S_N up to an order r' that lifts any degeneracies. For S_4 , we already know the number of irreps. and the corresponding Young's diagrams, which are



but what are the associated central characters? For the 2-cycles, in this case Equation (3.52) gives

$$\gamma_{[4]}^{[2]} = 6, \quad \gamma_{[3,1]}^{[2]} = 2, \quad \gamma_{[2,2]}^{[2]} = 0, \quad \gamma_{[2,1,1]}^{[2]} = -2, \quad \gamma_{[1,1,1,1]}^{[2]} = -6. \quad (\text{B.2})$$

We can see that even at this order, no degeneracies occur. Consequently, our CSCO has only two elements \hat{H}_P and $\hat{\Gamma}^{[2]}$. To give an example of further derivation, we will also compute $\gamma_{[\nu]}^{[3]}$ and $\hat{\Gamma}^{[3]}$ even if it is not strictly necessary for S_4 . Using Equation (3.53) the 3-cycle central characters reads

$$\gamma_{[4]}^{[3]} = 8, \quad \gamma_{[3,1]}^{[3]} = 0, \quad \gamma_{[2,2]}^{[3]} = -4, \quad \gamma_{[2,1,1]}^{[3]} = 0, \quad \gamma_{[1,1,1,1]}^{[3]} = 8. \quad (\text{B.3})$$

We can now proceed to the second step and gather the elements of the relevant conjugacy classes.

B.2 Element and representations of the conjugacy classes cc_r

We know which orders of class operators are required, let us move to their obtaining. According to their general expressions, class sum operators are the sum of all the elements of a given class cc_Λ . To visualize which elements will be needed, we have summarized all the elements that compose each of the five conjugacy classes of S_4 in Table B.1. At this stage, one can quickly verify each class's dimension using the formula of $|cc_\Lambda|$ in Equation (3.48). The question is now, how can we construct the representation of these elements?

On the one hand, we must select a representation. For this derivation, we will write the matrices on a snippet basis, which is more concise and convenient than the sectors. In a $2 + 2$ mixture scenario, this one reads

$$\{ \underset{1}{|\uparrow\uparrow\downarrow\downarrow\rangle}, \underset{2}{|\uparrow\downarrow\uparrow\downarrow\rangle}, \underset{3}{|\uparrow\downarrow\downarrow\uparrow\rangle}, \underset{4}{|\downarrow\uparrow\uparrow\downarrow\rangle}, \underset{5}{|\downarrow\uparrow\downarrow\uparrow\rangle}, \underset{6}{|\downarrow\downarrow\uparrow\uparrow\rangle} \}, \quad (\text{B.4})$$

On the other hand, we use a fundamental property of S_n 's elements: *each cycle can be decomposed into a product of 2-cycles*, and the elements of cc_Λ make no exception. Therefore, we will first represent every 2-cycles, and obtain $\Gamma^{[2]}$ by the same mean, then use them to build all the others r -cycles, and $\Gamma^{[r]}$ in a second time.

Table B.1: Elements of the five possible conjugacy classes cc_Λ of S_4 with the description of the cycle as well as all the elements that compose each class.

Partition	Cycle description	Cycle type elements of S_4
1+1+1+1	Four fixed points	() Id
2+1+1	One 2-cycle & Two fixed points	(1,2), (1,3), (1,4), (2,3), (2,4), (3,4)
2+2	Two 2-cycle	(1,2)(3,4), (1,3)(2,4), (1,4)(2,3)
3+1	One 3-cycle & one fixed point	(1,2,3), (1,3,2), (2,3,4), (2,4,3), (3,4,1), (3,1,4), (4,1,2), (4,2,1)
4	One 4-cycle	(1,2,3,4), (1,2,4,3), (1,3,2,4), (1,3,4,2), (1,4,3,2), (1,4,3,2)

B.2. Element and representations of the conjugacy classes 115

As we can see in Table B.1, the 2-cycles of S_4 are $P_{12}, P_{23}, P_{34}, P_{13}, P_{24}, P_{14}$. Let us start with P_{12} and compute the matrix elements of its representation $\hat{D}_{snip}(P_{12})$ in the snippet basis. If one swaps the two first components of each vector of the snippet basis, we obtain

$$\begin{aligned} P_{12} |\uparrow\uparrow\downarrow\downarrow\rangle &= |\uparrow\uparrow\downarrow\downarrow\rangle, & P_{12} |\uparrow\downarrow\uparrow\downarrow\rangle &= |\downarrow\uparrow\uparrow\downarrow\rangle, & P_{12} |\uparrow\downarrow\downarrow\uparrow\rangle &= |\downarrow\uparrow\downarrow\uparrow\rangle, \\ P_{12} |\downarrow\uparrow\uparrow\downarrow\rangle &= |\uparrow\downarrow\uparrow\downarrow\rangle, & P_{12} |\downarrow\uparrow\downarrow\uparrow\rangle &= |\uparrow\downarrow\downarrow\uparrow\rangle, & P_{12} |\downarrow\downarrow\uparrow\uparrow\rangle &= |\downarrow\downarrow\uparrow\uparrow\rangle. \end{aligned}$$

These manipulations show which vectors can be connected by the action of P_{12} , namely the non-zero matrix elements of $\hat{D}_{snip}(P_{12})$. Hence the representation of P_{12} reads

$$\hat{D}_{snip}(P_{12}) = \begin{pmatrix} 1 & 0 & 0 & 0 & 0 & 0 \\ 0 & 0 & 0 & 1 & 0 & 0 \\ 0 & 0 & 0 & 0 & 1 & 0 \\ 0 & 1 & 0 & 0 & 0 & 0 \\ 0 & 0 & 1 & 0 & 0 & 0 \\ 0 & 0 & 0 & 0 & 0 & 1 \end{pmatrix}. \quad (\text{B.5})$$

By application of the same process to the remaining 2-cycles, we finally get all the representations

$$\begin{aligned} \hat{D}_{snip}(P_{12}) &= \begin{pmatrix} 1 & 0 & 0 & 0 & 0 & 0 \\ 0 & 0 & 0 & 1 & 0 & 0 \\ 0 & 0 & 0 & 0 & 1 & 0 \\ 0 & 1 & 0 & 0 & 0 & 0 \\ 0 & 0 & 1 & 0 & 0 & 0 \\ 0 & 0 & 0 & 0 & 0 & 1 \end{pmatrix}, & \hat{D}_{snip}(P_{23}) &= \begin{pmatrix} 0 & 1 & 0 & 0 & 0 & 0 \\ 1 & 0 & 0 & 0 & 0 & 0 \\ 0 & 0 & 1 & 0 & 0 & 0 \\ 0 & 0 & 0 & 1 & 0 & 0 \\ 0 & 0 & 0 & 0 & 0 & 1 \\ 0 & 0 & 0 & 0 & 1 & 0 \end{pmatrix}, \\ \hat{D}_{snip}(P_{34}) &= \begin{pmatrix} 1 & 0 & 0 & 0 & 0 & 0 \\ 0 & 0 & 1 & 0 & 0 & 0 \\ 0 & 1 & 0 & 0 & 0 & 0 \\ 0 & 0 & 0 & 0 & 1 & 0 \\ 0 & 0 & 0 & 1 & 0 & 0 \\ 0 & 0 & 0 & 0 & 0 & 1 \end{pmatrix}, & \hat{D}_{snip}(P_{13}) &= \begin{pmatrix} 0 & 0 & 0 & 1 & 0 & 0 \\ 0 & 1 & 0 & 0 & 0 & 0 \\ 0 & 0 & 0 & 0 & 0 & 1 \\ 1 & 0 & 0 & 0 & 0 & 0 \\ 0 & 0 & 0 & 0 & 1 & 0 \\ 0 & 0 & 1 & 0 & 0 & 0 \end{pmatrix}, \\ \hat{D}_{snip}(P_{24}) &= \begin{pmatrix} 0 & 0 & 1 & 0 & 0 & 0 \\ 0 & 1 & 0 & 0 & 0 & 0 \\ 1 & 0 & 0 & 0 & 0 & 0 \\ 0 & 0 & 0 & 0 & 0 & 1 \\ 0 & 0 & 0 & 0 & 1 & 0 \\ 0 & 0 & 0 & 1 & 0 & 0 \end{pmatrix}, & \hat{D}_{snip}(P_{14}) &= \begin{pmatrix} 0 & 0 & 0 & 0 & 1 & 0 \\ 0 & 0 & 0 & 0 & 0 & 1 \\ 0 & 0 & 1 & 0 & 0 & 0 \\ 0 & 0 & 0 & 1 & 0 & 0 \\ 1 & 0 & 0 & 0 & 0 & 0 \\ 0 & 1 & 0 & 0 & 0 & 0 \end{pmatrix}. \end{aligned}$$

If one wants to get the same result in the sectors basis, the exact procedure must now be applied to the $4!$ permutation of the vector $|1, \sigma_1; 2, \sigma_2; 3, \sigma_3; 4, \sigma_4\rangle$, leading to $4! \times 4!$ matrices. For the r -cycles in the snippet basis, we can mindlessly use Table B.1 to construct the elements with products of 2-cycles. Thus, if we translate the cyclic notation in Table B.1 into permutation we have

$$\begin{aligned}
 (1, 2, 3) &= P_{12}P_{23}, & (1, 3, 2) &= P_{13}P_{23}, \\
 (2, 3, 4) &= P_{23}P_{34}, & (2, 4, 3) &= P_{24}P_{34}, \\
 (3, 4, 1) &= P_{34}P_{41}, & (3, 1, 4) &= P_{34}P_{41}, \\
 (4, 1, 2) &= P_{41}P_{12}, & (4, 1, 2) &= P_{41}P_{12}.
 \end{aligned}$$

With the representation in hand, we have all the ingredients to build the class sum operators.

B.3 r -cycle class-sum operators and symmetry analysis

The last step is simply to use the expression of the different class sum operators. For instance, with the 2-cycle and the 3-cycle class sum operator, we have

$$\hat{\Gamma}^{[2]} = \begin{pmatrix} 2 & 1 & 1 & 1 & 1 & 0 \\ 1 & 2 & 1 & 1 & 0 & 1 \\ 1 & 1 & 2 & 0 & 1 & 1 \\ 1 & 1 & 0 & 2 & 1 & 1 \\ 1 & 0 & 1 & 1 & 2 & 1 \\ 0 & 1 & 1 & 1 & 1 & 2 \end{pmatrix}, \quad \hat{\Gamma}^{[3]} = \begin{pmatrix} 0 & 2 & 2 & 2 & 2 & 0 \\ 2 & 0 & 2 & 2 & 0 & 2 \\ 2 & 2 & 0 & 0 & 2 & 2 \\ 2 & 2 & 0 & 0 & 2 & 2 \\ 2 & 0 & 2 & 2 & 0 & 2 \\ 0 & 2 & 2 & 2 & 2 & 0 \end{pmatrix}. \quad (\text{B.6})$$

The eigenvalues of the $\hat{\Gamma}^{[2]}$ and $\hat{\Gamma}^{[3]}$ are respectively $\{6, 2, 2, 2, 0, 0\}$ and $\{8, 0, 0, 0, -4, -4\}$ which correspond to the diagram $Y_{[1,1,1,1]}$, $Y_{[2,1,1]}$ and $Y_{[2,2]}$. As an example, one can obtain the analog representation of $\hat{\Gamma}^{[2]}$ in the following sector basis

$$\begin{aligned}
 &\{ |1234\rangle, |1243\rangle, |2134\rangle, |2143\rangle, |1324\rangle, |1423\rangle, \\
 &|2314\rangle, |2413\rangle, |1342\rangle, |1432\rangle, |2341\rangle, |2431\rangle, \\
 &|3124\rangle, |4123\rangle, |3214\rangle, |4213\rangle, |3142\rangle, |4132\rangle, \\
 &|3241\rangle, |4231\rangle, |3412\rangle, |4312\rangle, |3421\rangle, |4321\rangle \}, \quad (\text{B.7})
 \end{aligned}$$

where the vectors $|i, j, k, l\rangle$ are an abbreviation of the vectors $|i, \sigma_i; j, \sigma_j; k, \sigma_k; l, \sigma_l\rangle$. We then can express $\hat{\Gamma}^{[2]}$ as follow

118 Appendix B. $SU(2)$ symmetry analysis of a $2 + 2$ mixture

Table B.2: Expectation values of the operator $\hat{\Gamma}^{[2]}$ and $\hat{\Gamma}^{[3]}$ (resp. $\hat{\Gamma}^{[2]}$ and $\hat{\Gamma}^{[3]}$) in the eigenstates $|a_P\rangle_i$ of the ground state manifold of \hat{H}_{SU} for $2 + 2$ fermionic (resp. bosonic) mixtures in presence of DBC. The states have been order by decreasing energy slope K .

$2F + 2F$		
$ a_P\rangle_i$	$\langle a_P \hat{\Gamma}^{[2]} a_P \rangle_i$	$\langle a_P \hat{\Gamma}^{[3]} a_P \rangle_i$
$(1, -2 - \sqrt{3}, 1 + \sqrt{3}, 1 + \sqrt{3}, -2 - \sqrt{3}, 1)$	0	-4
$(-1, 1 + \sqrt{2}, 0, 0, -1 - \sqrt{2}, 1)$	-2	0
$(0, 0, -1, 1, 0, 0)$	-2	0
$(1, -2 + \sqrt{3}, 1 - \sqrt{3}, 1 - \sqrt{3}, -2 + \sqrt{3}, 1)$	0	-4
$(-1, 1 - \sqrt{2}, 0, 0, -1 + \sqrt{2}, 1)$	-2	0
$(1, 1, 1, 1, 1, 1)$	-6	8
$2B + 2B$		
$ a_P\rangle_i$	$\langle a_P \hat{\Gamma}^{[2]} a_P \rangle_i$	$\langle a_P \hat{\Gamma}^{[3]} a_P \rangle_i$
$(1, -1, 1, 1, -1, 1)$	6	8
$(-1, -1 + \sqrt{2}, 0, 0, 1 - \sqrt{2}, 1)$	2	0
$(1, 2 - \sqrt{3}, 1 - \sqrt{3}, 1 - \sqrt{3}, 2 - \sqrt{3}, 1)$	0	-4
$(0, 0, -1, 1, 0, 0)$	2	0
$(-1, -1 - \sqrt{2}, 0, 0, 1 + \sqrt{2}, 1)$	2	0
$(1, 2 + \sqrt{3}, 1 + \sqrt{3}, 1 + \sqrt{3}, 2 + \sqrt{3}, 1)$	0	-4

Appendix C

Large- k tail of the momentum distribution of TB in the box

As a reminder, the large- k tail of $n(k)$ for the Tonks-Girardeau gas (Equation (4.21) of the main text) is given by

$$\lim_{k \rightarrow \infty} k^4 n^{\text{TG}}(k) = \mathcal{C}_N^{\text{TG}} + \mathcal{B}_N + \mathcal{A}_N \cos(kL) = \frac{N}{N-1} \mathcal{C}_N^{\text{TG}} + \mathcal{A}_N \cos(kL), \quad (\text{C.1})$$

where $\mathcal{C}_N^{\text{TG}}$ is the Tan contact related to this system, and \mathcal{B}_N and \mathcal{A}_N are the same for the case of spinless fermions (see Section 4.1 of the main document). The similarities between Equation (4.4) and (4.21) could be understood from the fact that $\rho_1^{\text{TG}}(x, y)$ can always be written in terms of the fermionic reduced density matrices $\rho_j^{\text{SF}}(x, \dots)$ as [Lenard, 1964]

$$\rho_1^{\text{TG}}(x, y) = \rho_1^{\text{SF}}(x, y) + \sum_{j=1}^{N-1} \frac{(-2)^j}{j!} \int_x^y dx_2 \dots dx_{1+j} \rho_{1+j}^{\text{SF}}(x, x_2, \dots; y, x_2, \dots), \quad (\text{C.2})$$

which is Equation (4.18) of the main text.

The first term of Equation (C.2) gives rise to the same terms of Equation (4.4). We now show why there is not a $(-1)^{N-1}$ factor for TG gas with respect to the spinless fermion case. To do that, we write the integral of the second term in Equation (C.2) as follows

$$\begin{aligned} \int_{-L/2}^{L/2} dx_2 \dots dx_{1+j} \rho_{1+j}^{\text{F}}(x, x_2, \dots; y, x_2, \dots) &= (N-1)(N-2) \dots (N-j) \rho_1^{\text{F}}(x, y) \\ &= \frac{(N-1)!}{(N-j-1)!} \rho_1^{\text{F}}(x, y), \end{aligned} \quad (\text{C.3})$$

and we notice that

$$\begin{aligned} \sum_{j=1}^{N-1} \frac{(-2)^j}{j!} \frac{(N-1)!}{(N-j-1)!} &= \sum_{j=1}^{N-1} (-2)^j \binom{N-1}{j} \\ &= \sum_{j=0}^{N-1} (-2)^j \binom{N-1}{j} - 1 = (-1)^{N-1} - 1. \end{aligned} \quad (\text{C.4})$$

Using Equation (C.3) and (C.4), we then evaluate

$$\lim_{\substack{x \rightarrow -\frac{L}{2} \\ y \rightarrow \frac{L}{2}}} \sum_{j=1}^{N-1} \frac{(-2)^j}{j!} \int_x^y dx_2 \dots dx_{1+j} \rho_{1+j}^F(x, x_2, \dots; y, x_2, \dots) \quad (\text{C.5})$$

$$= \sum_{j=1}^{N-1} \frac{(-2)^j}{j!} \frac{(N-1)!}{(N-j-1)!} \rho_1^F(x, y)|_{x \sim -\frac{L}{2}, y \sim \frac{L}{2}}, \quad (\text{C.6})$$

$$= \rho_1^F(x, y)|_{x \sim -\frac{L}{2}, y \sim \frac{L}{2}} [(-1)^{N-1} - 1], \quad (\text{C.7})$$

which gives a factor -2 for N even and 0 for N odd (Equation (4.20) of the main text). The sum of Equation (C.7) and the first term in the expansion in Equation (C.2) appears then in Equation (C.1) with a positive sign in front of \mathcal{A}_N regardless of the parity of N .

We now evaluate the additional term, which corresponds to the Tan contact. This term differs from the others because it is connected to two-body correlations. Indeed, it can be written as [Sant'Ana et al., 2019]

$$\mathcal{C}_N^{\text{TG}} = \frac{2}{\pi} \int_{-L/2}^{L/2} dx_2 \lim_{x, y \rightarrow x_2} \frac{\rho_2^F(x, x_2; y, x_2)}{|x - x_2||y - x_2|} = \frac{(N-1)N(N+1)(2N+1)}{3L^3} \pi. \quad (\text{C.8})$$

Finally, we see that, for the case of a TG gas, $\mathcal{C}_N^{\text{TG}} = (N-1)\mathcal{B}_N$, and, therefore, we end up with Equation (C.1).

Bibliography

- [Abramowitz et al., 1971] Abramowitz, M., Stegun, I. A., & Greenhill, A. G. (1971). *Handbook of Mathematical Functions with Formulas, Graphs*. Dover Publications.
- [Allen & Misener, 1938] Allen, J. F. & Misener, A. D. (1938). Flow of Liquid Helium II. *Nature*, vol. 141(3558), page 75.
- [Anderson et al., 1995] Anderson, M. H., Ensher, J. R., Matthews, M. R., Wieman, C. E., & Cornell, E. A. (1995). Observation of Bose-Einstein Condensation in a Dilute Atomic Vapor. *Science*, vol. 269(5221), pages 198–201.
- [Auerbach, 1994] Auerbach, A. (1994). *Interacting Electrons and Quantum Magnetism*. Springer.
- [Aupetit-Diallo et al., 2023] Aupetit-Diallo, G., Musolino, S., Albert, M., & Vignolo, P. (2023). High-momentum oscillating tails of strongly interacting one-dimensional gases in a box. *Phys. Rev. A*, vol. 107, page L061301.
- [Aupetit-Diallo et al., 2022] Aupetit-Diallo, G., Pecci, G., Pignol, C., Hébert, F., Minguzzi, A., Albert, M., & Vignolo, P. (2022). Exact solution for SU(2)-symmetry-breaking bosonic mixtures at strong interactions. *Phys. Rev. A*, vol. 106(3), page 033312.
- [Barceló et al., 2001] Barceló, C., Liberati, S., & Visser, M. (2001). Analogue gravity from Bose-Einstein condensates. *Classical and Quantum Gravity*, vol. 18(6), page 1137.
- [Barfknecht et al., 2021] Barfknecht, R. E., Foerster, A., Zinner, N. T., & Volosniev, A. G. (2021). Generation of spin currents by a temperature gradient in a two-terminal device. *Communications Physics*, vol. 4, page 252.
- [Barth & Zwerger, 2011] Barth, M. & Zwerger, W. (2011). Tan relations in one dimension. *Annals of Physics*, vol. 326, pages 2544–2565.
- [Batchelor et al., 2005] Batchelor, M. T., Guan, X. W., Oelkers, N., & Lee, C. (2005). The 1D interacting Bose gas in a hard wall box. *Journal of Physics A: Mathematical and General*, vol. 38(36), page 7787.
- [Bethe, 1931] Bethe, H. (1931). Zur Theorie der Metalle. *Zeitschrift für Physik*, vol. 71(3), pages 205–226.

- [Billam et al., 2013] Billam, T. P., Marchant, A. L., Cornish, S. L., Gardiner, S. A., & Parker, N. G. (2013). *Bright Solitary Matter Waves: Formation, Stability and Interactions*. Berlin: Springer Berlin Heidelberg.
- [Bleistein & Handelsman, 1986] Bleistein, N. & Handelsman, R. A. (1986). *Asymptotic Expansions of Integrals*. Dover Publications.
- [Bloch, 1973] Bloch, F. (1973). Superfluidity in a Ring. *Physical Review A*, vol. 7(6), pages 2187–2191.
- [Bloch et al., 2008] Bloch, I., Dalibard, J., & Zwerger, W. (2008). Many-body physics with ultracold gases. *Reviews of Modern Physics*, vol. 80(3), pages 885–964.
- [Bloch et al., 2000] Bloch, I., Hänsch, T. W., & Esslinger, T. (2000). Measurement of the spatial coherence of a trapped Bose gas at the phase transition. *Nature*, vol. 403(6766), pages 166–170.
- [Bouchoule & Dubail, 2021] Bouchoule, I. & Dubail, J. (2021). Breakdown of Tan’s Relation in Lossy One-Dimensional Bose Gases. *Physical Review Letters*, vol. 126(16), page 160603.
- [Calabrese et al., 2016] Calabrese, P., Essler, F. H. L., & Mussardo, G. (2016). Introduction to ‘Quantum Integrability in Out of Equilibrium Systems’. *Journal of Statistical Mechanics: Theory and Experiment*, vol. 2016(6), page 064001.
- [Castelvecchi, 2023] Castelvecchi, D. (2023). *Nature*. <https://www.nature.com/articles/d41586-023-00536-w>.
- [Cayla et al., 2023] Cayla, H., Massignan, P., Giamarchi, T., Aspect, A., Westbrook, C. I., & Clément, D. (2023). Observation of $1/k^4$ after Expansion of Bose-Einstein Condensates with Impurities. *Physical Review Letters*, vol. 130(15), page 153401.
- [Cazalilla et al., 2011] Cazalilla, M. A., Citro, R., Giamarchi, T., Orignac, E., & Rigol, M. (2011). One dimensional bosons: From condensed matter systems to ultracold gases. *Rev. Mod. Phys.*, vol. 83, pages 1405–1466.
- [Chetcuti et al., 2022] Chetcuti, W. J., Haug, T., Kwek, L.-C., & Amico, L. (2022). Persistent current of SU(N) fermions. *SciPost Phys.*, vol. 12, page 033.
- [Cohen-Tannoudji et al., 1986] Cohen-Tannoudji, C., Diu, B., & Laloe, F. (1986). *Quantum Mechanics, Volume 1*. Wiley-VCH.
- [Curie, 1894] Curie, P. (1894). Sur la symétrie dans les phénomènes physiques, symétrie d’un champ électrique et d’un champ magnétique. *J. Phys. Theor. Appl.*, vol. 3(1), pages 393–415.
- [de Boer & Verwey, 1937] de Boer, J. H. & Verwey, E. J. W. (1937). Semiconductors with partially and with completely filled 3d-lattice bands. *Proceedings of the Physical Society*, vol. 49(4S), page 59.

- [De Bruyne et al., 2021] De Bruyne, B., Dean, D. S., Le Doussal, P., Majumdar, S. N., & Schehr, G. (2021). Wigner function for noninteracting fermions in hard-wall potentials. *Physical Review A*, vol. 104(1), page 013314.
- [Dean et al., 2019] Dean, D. S., Doussal, P. L., Majumdar, S. N., & Schehr, G. (2019). Noninteracting fermions in a trap and random matrix theory. *Journal of Physics A: Mathematical and Theoretical*, vol. 52(14), page 144006.
- [Decamp et al., 2016a] Decamp, J., Armagnat, P., Fang, B., Albert, M., Minguzzi, A., & Vignolo, P. (2016a). Exact density profiles and symmetry classification for strongly interacting multi-component Fermi gases in tight waveguides. *New Journal of Physics*, vol. 18(5), page 055011.
- [Decamp et al., 2016b] Decamp, J., Jünemann, J., Albert, M., Rizzi, M., Minguzzi, A., & Vignolo, P. (2016b). High-momentum tails as magnetic-structure probes for strongly correlated $SU(\kappa)$ fermionic mixtures in one-dimensional traps. *Phys. Rev. A*, vol. 94(5), page 053614.
- [Decamp et al., 2017] Decamp, J., Jünemann, J., Albert, M., Rizzi, M., Minguzzi, A., & Vignolo, P. (2017). Strongly correlated one-dimensional Bose–Fermi quantum mixtures: symmetry and correlations. *New Journal of Physics*, vol. 19(12), page 125001.
- [Deuretzbacher et al., 2014] Deuretzbacher, F., Becker, D., Bjerlin, J., Reimann, S. M., & Santos, L. (2014). Quantum magnetism without lattices in strongly interacting one-dimensional spinor gases. *Phys. Rev. A*, vol. 90(1), page 013611.
- [Deuretzbacher et al., 2016] Deuretzbacher, F., Becker, D., & Santos, L. (2016). Momentum distributions and numerical methods for strongly interacting one-dimensional spinor gases. *Phys. Rev. A*, vol. 94(2), page 023606.
- [Deuretzbacher et al., 2008] Deuretzbacher, F., Fredenhagen, K., Becker, D., Bongs, K., Sengstock, K., & Pfannkuche, D. (2008). Exact Solution of Strongly Interacting Quasi-One-Dimensional Spinor Bose Gases. *Phys. Rev. Lett.*, vol. 100(16), page 160405.
- [Devillard et al., 2020] Devillard, P., Chevallier, D., Vignolo, P., & Albert, M. (2020). Full counting statistics of the momentum occupation numbers of the Tonks-Girardeau gas. *Physical Review A*, vol. 101(6), page 063604.
- [Dirac, 1929] Dirac, P. A. M. (1929). Quantum mechanics of many-electron systems. *Proceedings of The Royal Society A: Mathematical, Physical and Engineering Sciences*, vol. 123, pages 714–733.
- [Doughty & Lawler, 1984] Doughty, D. K. & Lawler, J. E. (1984). Spatially resolved electric field measurements in the cathode fall using optogalvanic detection of Rydberg atoms. *Applied Physics Letters*, vol. 45(6), pages 611–613.
- [Dyson, 2004a] Dyson, F. J. (2004a). Statistical Theory of the Energy Levels of Complex Systems. I. *Journal of Mathematical Physics*, vol. 3(1), pages 140–156.

- [Dyson, 2004b] Dyson, F. J. (2004b). Statistical Theory of the Energy Levels of Complex Systems. II. *Journal of Mathematical Physics*, vol. 3(1), pages 157–165.
- [Dyson, 2004c] Dyson, F. J. (2004c). Statistical Theory of the Energy Levels of Complex Systems. III. *Journal of Mathematical Physics*, vol. 3(1), pages 166–175.
- [Dyson & Mehta, 2004] Dyson, F. J. & Mehta, M. L. (2004). Statistical Theory of the Energy Levels of Complex Systems. IV. *Journal of Mathematical Physics*, vol. 4(5), pages 701–712.
- [Einstein, 1905a] Einstein, A. (1905a). Zur Elektrodynamik bewegter Körper. *Annalen der Physik*, vol. 322(10), pages 891–921.
- [Einstein, 1905b] Einstein, A. (1905b). Über die von der molekularkinetischen Theorie der Wärme geforderte Bewegung von in ruhenden Flüssigkeiten suspendierten Teilchen. *Annalen der Physik*, vol. 322(8), pages 549–560.
- [Englert & Brout, 1964] Englert, F. & Brout, R. (1964). Broken Symmetry and the Mass of Gauge Vector Mesons. *Physical Review Letters*, vol. 13(9), pages 321–323.
- [Essler et al., 2005] Essler, F. H. L., Frahm, H., Göhmann, F., Klümper, A., & Korepin, V. E. (2005). *The One-Dimensional Hubbard Model*. Cambridge: Cambridge University Press.
- [Faley et al., 2004] Faley, M. I., Pratt, K., Reineman, R., Schurig, D., Gott, S., Atwood, C. G., Sarwinski, R. E., Paulson, D. N., Starr, T. N., & Fagaly, R. L. (2004). High temperature superconductor dc SQUID micro-susceptometer for room temperature objects. *Superconductor Science and Technology*, vol. 17(5), page S324.
- [Fang et al., 2011] Fang, B., Vignolo, P., Gattobigio, M., Miniatura, C., & Minguzzi, A. (2011). Exact solution for the degenerate ground-state manifold of a strongly interacting one-dimensional bose-fermi mixture. *Phys. Rev. A*, vol. 84, page 023626.
- [Fang et al., 2009] Fang, B., Vignolo, P., Miniatura, C., & Minguzzi, A. (2009). Fermionization of a strongly interacting bose-fermi mixture in a one-dimensional harmonic trap. *Phys. Rev. A*, vol. 79, page 023623.
- [Fetter & Svidzinsky, 2001] Fetter, A. L. & Svidzinsky, A. A. (2001). Vortices in a trapped dilute Bose-Einstein condensate. *Journal of Physics: Condensed Matter*, vol. 13(12), page R135.
- [Feynman, 1982] Feynman, R. P. (1982). Simulating physics with computers. *International Journal of Theoretical Physics*, vol. 21(6), pages 467–488.
- [Fisher, 1915] Fisher, R. A. (1915). Frequency Distribution of the Values of the Correlation Coefficient in Samples from an Indefinitely Large Population. *Biometrika*, vol. 10(4), pages 507–521.

- [Forrester et al., 2003a] Forrester, P., Frankel, N., Garoni, T., & Witte, N. (2003a). Painlevé Transcendent Evaluations of Finite System Density Matrices for 1d Impenetrable Bosons. *Communications in Mathematical Physics*, vol. 238(1), pages 257–285.
- [Forrester et al., 2003b] Forrester, P. J., Frankel, N. E., Garoni, T. M., & Witte, N. S. (2003b). Finite one-dimensional impenetrable Bose systems: Occupation numbers. *Phys. Rev. A*, vol. 67(4), page 043607.
- [Franchini et al., 2017] Franchini, F. et al. (2017). *An introduction to integrable techniques for one-dimensional quantum systems*. Springer.
- [Fredholm, 1903] Fredholm, I. (1903). Sur une classe d'équations fonctionnelles. *Acta Mathematica*, vol. 27, pages 365–390.
- [Frobenius, 1896] Frobenius, G. (1896). Über vertauschbare matrizen. *Sitz.-Ber, Akad. Wiss. Berlin*.
- [Galton, 1877] Galton, F. (1877). Typical laws of heredity. *Nature*, vol. 15, pages 492–5, 512–4, 532–3.
- [Galton, 1889] Galton, F. (1889). Kinship and Correlation. *Statistical Science*, vol. 4(2), pages 81 – 86.
- [Gaudin, 1971] Gaudin, M. (1971). Boundary energy of a bose gas in one dimension. *Phys. Rev. A*, 4, 386–394.
- [Gaudin, 1976] Gaudin, M. (1976). Diagonalisation d'une classe d'hamiltoniens de spin. *J. Phys. France*, vol. 37(10), pages 1087–1098.
- [Gerritsma et al., 2010] Gerritsma, R., Kirchmair, G., Zähringer, F., Solano, E., Blatt, R., & Roos, C. F. (2010). Quantum simulation of the Dirac equation. *Nature*, vol. 463(7277), pages 68–71.
- [Giamarchi, 2021] Giamarchi, T. (2021). <https://boulderschool.yale.edu/2021/boulder-school-2021-lecture-notes>.
- [Girardeau, 1960] Girardeau, M. (1960). Relationship between Systems of Impenetrable Bosons and Fermions in One Dimension. *Journal of Mathematical Physics*, vol. 1(6), pages 516–523.
- [Glauber, 1963] Glauber, R. J. (1963). The Quantum Theory of Optical Coherence. *Phys. Rev.*, vol. 130(6), pages 2529–2539.
- [Greiner et al., 2002] Greiner, M., Mandel, O., Esslinger, T., Hänsch, T. W., & Bloch, I. (2002). Quantum phase transition from a superfluid to a Mott insulator in a gas of ultracold atoms. *Nature*, vol. 415(6867), pages 39–44.
- [Greiner & Müller, 1989] Greiner, W. & Müller, B. (1989). *Symmetries in Quantum Mechanics*. Springer.

- [Guan & He, 2022] Guan, X.-W. & He, P. (2022). New trends in quantum integrability: recent experiments with ultracold atoms. *Reports on Progress in Physics*, vol. 85(11), page 114001.
- [Hamermesh, 1962] Hamermesh, M. (1962). *Group theory and its application to physical problems*. Dover Publications Inc.
- [Henkel et al., 2017] Henkel, C., Sauer, T.-O., & Proukakis, N. P. (2017). Cross-over to quasi-condensation: mean-field theories and beyond. *Journal of Physics B: Atomic, Molecular and Optical Physics*, vol. 50(11), page 114002.
- [Hess, 1986] Hess, H. F. (1986). Evaporative cooling of magnetically trapped and compressed spin-polarized hydrogen. *Physical Review B*, vol. 34(5), pages 3476–3479.
- [Higgs, 1964] Higgs, P. W. (1964). Broken Symmetries and the Masses of Gauge Bosons. *Physical Review Letters*, vol. 13(16), page 508–509.
- [Holland et al., 2001] Holland, M., Kokkelmans, S. J. J. M. F., Chiofalo, M. L., & Walser, R. (2001). Resonance Superfluidity in a Quantum Degenerate Fermi Gas. *Physical Review Letters*, vol. 87(12), page 120406.
- [Hotelling, 1936] Hotelling, H. (1936). Relations Between Two Sets of Variates. *Biometrika*, vol. 28(3/4), pages 321–377.
- [Huang & Yang, 1957] Huang, K. & Yang, C. N. (1957). Quantum-Mechanical Many-Body Problem with Hard-Sphere Interaction. *Phys. Rev.*, vol. 105(3), pages 767–775.
- [Hänsch & Schawlow, 1975] Hänsch, T. & Schawlow, A. (1975). Cooling of gases by laser radiation. *Optics Communications*, vol. 13(1), pages 68–69.
- [Imambekov & Demler, 2006a] Imambekov, A. & Demler, E. (2006a). Applications of exact solution for strongly interacting one-dimensional Bose–Fermi mixture: Low-temperature correlation functions, density profiles, and collective modes. *Annals of Physics*, vol. 321(10), pages 2390–2437.
- [Imambekov & Demler, 2006b] Imambekov, A. & Demler, E. (2006b). Exactly solvable case of a one-dimensional Bose–Fermi mixture. *Physical Review A*, vol. 73(2), page 021602.
- [Jones & Chapman, 1924a] Jones, J. E. & Chapman, S. (1924a). On the determination of molecular fields. —II. From the equation of state of a gas. *Proceedings of the Royal Society of London. Series A, Containing Papers of a Mathematical and Physical Character*, vol. 106(738), pages 463–477.
- [Jones & Chapman, 1924b] Jones, J. E. & Chapman, S. (1924b). On the determination of molecular fields.—I. From the variation of the viscosity of a gas with temperature. *Proceedings of the Royal Society of London. Series A, Containing Papers of a Mathematical and Physical Character*, vol. 106(738), pages 441–462.

- [Kapitza, 1938] Kapitza, P. (1938). Viscosity of Liquid Helium below the λ -Point. *Nature*, vol. 141(3558), page 74.
- [Kasevich & Chu, 1991] Kasevich, M. & Chu, S. (1991). Atomic interferometry using stimulated Raman transitions. *Physical Review Letters*, vol. 67(2), page 181–184.
- [Katriel, 1993] Katriel, J. (1993). Representation-free evaluation of the eigenvalues of the class-sums of the symmetric group. *Journal of Physics A: Mathematical and General*, vol. 26(4), page L135.
- [Kibble, 1976] Kibble, T. W. B. (1976). Topology of cosmic domains and strings. *Journal of Physics A: Mathematical and General*, vol. 9(8), page 1387.
- [Kinoshita et al., 2004] Kinoshita, T., Wenger, T., & Weiss, D. S. (2004). Observation of a One-Dimensional Tonks-Girardeau Gas. *Science*, vol. 305(5687), pages 1125–1128.
- [Kinoshita et al., 2005] Kinoshita, T., Wenger, T., & Weiss, D. S. (2005). Local Pair Correlations in One-Dimensional Bose Gases. *Physical Review Letters*, vol. 95(19), page 190406.
- [Kirillov & Sakamoto, 2014] Kirillov, A. N. & Sakamoto, R. (2014). Singular solutions to the bethe ansatz equations and rigged configurations. *Journal of Physics A: Mathematical and Theoretical*, vol. 47(20), page 205207.
- [Kittel, 1976] Kittel, C. (1976). *Introduction to solid state physics*. John & Wiley.
- [Kominis et al., 2003] Kominis, I. K., Kornack, T. W., Allred, J. C., & Romalis, M. V. (2003). A subfemtotesla multichannel atomic magnetometer. *Nature*, vol. 422(6932), pages 596–599.
- [Korepin et al., 1993] Korepin, V. E., Bogoliubov, N. M., & Izergin, A. G. (1993). *Quantum Inverse Scattering Method and Correlation Functions*. Cambridge Monographs on Mathematical Physics. Cambridge University Press.
- [Kota, 2020] Kota, V. K. B. (2020). *SU(3) Symmetry in Atomic Nuclei*. Springer Nature Singapore.
- [Lacroix-A-Chez-Toine et al., 2018] Lacroix-A-Chez-Toine, B., Le Doussal, P., Majumdar, S. N., & Schehr, G. (2018). Non-interacting fermions in hard-edge potentials. *Journal of Statistical Mechanics: Theory and Experiment*, vol. 2018(12), page 123103. IOP Publishing and SISSA.
- [Landau & Lifshitz, 2013] Landau, L. D. & Lifshitz, E. M. (2013). *Quantum mechanics: non-relativistic theory*, volume 3. Elsevier.
- [Langen et al., 2015] Langen, T., Geiger, R., & Schmiedmayer, J. (2015). Ultracold Atoms Out of Equilibrium. *Annual Review of Condensed Matter Physics*, vol. 6(1), pages 201–217.

- [Lenard, 1964] Lenard, A. (1964). Momentum Distribution in the Ground State of the One-Dimensional System of Impenetrable Bosons. *Journal of Mathematical Physics*, vol. 5(7), pages 930–943.
- [Lenard, 1966] Lenard, A. (1966). One-Dimensional Impenetrable Bosons in Thermal Equilibrium. *Journal of Mathematical Physics*, vol. 7, pages 1268–1272.
- [Lennard-Jones, 1931] Lennard-Jones, J. E. (1931). Cohesion. *Proceedings of the Physical Society*, vol. 43(5), page 461.
- [Lewenstein et al., 2007] Lewenstein, M., Sanpera, A., Ahufinger, V., Damski, B., Sen(De), A., & Sen, U. (2007). Ultracold atomic gases in optical lattices: mimicking condensed matter physics and beyond. *Advances in Physics*, vol. 56(2), pages 243–379.
- [Li et al., 2003] Li, Y.-Q., Gu, S.-J., Ying, Z.-J., & Eckern, U. (2003). Exact results of the ground state and excitation properties of a two-component interacting Bose system. *Europhysics Letters*, vol. 61(3), page 368.
- [Lieb & Liniger, 1963] Lieb, E. H. & Liniger, W. (1963). Exact Analysis of an Interacting Bose Gas. I. The General Solution and the Ground State. *Phys. Rev.*, vol. 130(4), pages 1605–1616.
- [Ma, 2007] Ma, Z.-Q. (2007). *Group Theory for Physicists*. World Scientific Publishing.
- [MacDonald, 1979] MacDonald, I. G. (1979). *Symmetric functions and Hall polynomials*. Oxford Mathematical Monographs.
- [Manin, 1980] Manin, Y. (1980). *Computable and non-computable*. Moscow, Soviet Radio.
- [Manninen et al., 2012] Manninen, M., Viefers, S., & Reimann, S. (2012). Quantum rings for beginners II: Bosons versus fermions. *Physica E: Low-dimensional Systems and Nanostructures*, vol. 46, pages 119–132.
- [Maschke, 1898] Maschke, H. (1898). Ueber den arithmetischen Charakter der Coefficienten der Substitutionen endlicher linearer Substitutionsgruppen. *Mathematische Annalen*, vol. 50(4), pages 492–498.
- [Maschke, 1899] Maschke, H. (1899). Beweis des Satzes, dass diejenigen endlichen linearen Substitutionsgruppen, in welchen einige durchgehends verschwindende Coefficienten auftreten, intransitiv sind. *Mathematische Annalen*, vol. 52(2), pages 363–368.
- [McClelland et al., 2016] McClelland, J. J., Steele, A. V., Knuffman, B., Twedt, K. A., Schwarzkopf, A., & Wilson, T. M. (2016). Bright focused ion beam sources based on laser-cooled atoms. *Applied Physics Reviews*, vol. 3(1), page 011302.

- [Meckes, 2019] Meckes, E. S. (2019). *The Random Matrix Theory of the Classical Compact Groups*. Cambridge Tracts in Mathematics. Cambridge: Cambridge University Press.
- [Mehta & Dyson, 2004] Mehta, M. L. & Dyson, F. J. (2004). Statistical Theory of the Energy Levels of Complex Systems. V. *Journal of Mathematical Physics*, vol. 4(5), pages 713–719.
- [Minguzzi & Vignolo, 2022] Minguzzi, A. & Vignolo, P. (2022). Strongly interacting trapped one-dimensional quantum gases: Exact solution. *AVS Quantum Science*, 4(2).
- [Minguzzi et al., 2002] Minguzzi, A., Vignolo, P., & Tosi, M. P. (2002). High-momentum tail in the Tonks gas under harmonic confinement. *Physics Letters A*, vol. 294(3), pages 222–226.
- [Mott & Peierls, 1937] Mott, N. F. & Peierls, R. (1937). Discussion of the paper by de Boer and Verwey. *Proceedings of the Physical Society*, vol. 49(4S), page 72.
- [Naldesi et al., 2022] Naldesi, P., Polo, J., Dunjko, V., Perrin, H., Olshanii, M., Amico, L., & Minguzzi, A. (2022). Enhancing sensitivity to rotations with quantum solitonic currents. *SciPost Phys.*, vol. 12, page 138.
- [Nataf & Mila, 2014] Nataf, P. & Mila, F. (2014). Exact Diagonalization of Heisenberg SU(N) Models. *Physical Review Letters*, vol. 113(12), page 127204.
- [Navon et al., 2021] Navon, N., Smith, R. P., & Hadzibabic, Z. (2021). Quantum gases in optical boxes. *Nature Physics*, vol. 17(12), pages 1334–1341.
- [Nepomechie & Wang, 2013] Nepomechie, R. I. & Wang, C. (2013). Algebraic bethe ansatz for singular solutions. *Journal of Physics A: Mathematical and Theoretical*, vol. 46(32), page 325002.
- [Noether, 1918] Noether, E. (1918). Nachrichten von der gesellschaft der wissenschaften zu göttingen. *Mathematisch-Physikalische Klasse*, vol. 1918, pages 235–257.
- [Oelkers et al., 2006] Oelkers, N., Batchelor, M. T., Bortz, M., & Guan, X.-W. (2006). Bethe ansatz study of one-dimensional Bose and Fermi gases with periodic and hard wall boundary conditions. *Journal of Physics A: Mathematical and General*, vol. 39(5), page 1073.
- [Ogata & Shiba, 1990] Ogata, M. & Shiba, H. (1990). Bethe-ansatz wave function, momentum distribution, and spin correlation in the one-dimensional strongly correlated Hubbard model. *Physical Review B*, vol. 41(4), pages 2326–2338.
- [Olshanii, 1998] Olshanii, M. (1998). Atomic Scattering in the Presence of an External Confinement and a Gas of Impenetrable Bosons. *Physical Review Letters*, vol. 81(5), pages 938–941.

- [Olshanii & Dunjko, 2003] Olshanii, M. & Dunjko, V. (2003). Short-Distance Correlation Properties of the Lieb-Liniger System and Momentum Distributions of Trapped One-Dimensional Atomic Gases. *Phys. Rev. Lett.*, vol. 91(9), page 090401.
- [Pagano et al., 2014] Pagano, G., Mancini, M., Cappellini, G., Lombardi, P., Schäfer, F., Hu, H., Liu, X.-J., Catani, J., Sias, C., Inguscio, M., & Fallani, L. (2014). A one-dimensional liquid of fermions with tunable spin. *Nature Physics*, vol. 10(3), pages 198–201.
- [Papenbrock, 2003] Papenbrock, T. (2003). Ground-state properties of hard-core bosons in one-dimensional harmonic traps. *Physical Review A*, vol. 67(4), page 041601.
- [Paredes et al., 2004] Paredes, B., Widera, A., Murg, V., Mandel, O., Fölling, S., Cirac, I., Shlyapnikov, G. V., Hänsch, T. W., & Bloch, I. (2004). Tonks–Girardeau gas of ultracold atoms in an optical lattice. *Nature*, vol. 429(6989), pages 277–281.
- [Pâțu & Klümper, 2017] Pâțu, O. I. & Klümper, A. (2017). Universal Tan relations for quantum gases in one dimension. *Phys. Rev. A*, vol. 96(6), page 063612.
- [Pecci et al., 2023] Pecci, G., Aupetit-Diallo, G., Albert, M., Vignolo, P., & Minguzzi, A. (2023). Persistent currents in a strongly interacting multicomponent Bose gas on a ring. *Comptes Rendus. Physique*, Online first, pages 1–13.
- [Pecci et al., 2021] Pecci, G., Naldesi, P., Amico, L., & Minguzzi, A. (2021). Probing the BCS-BEC crossover with persistent currents. *Physical Review Research*, vol. 3(3), page L032064.
- [Peters et al., 1999] Peters, A., Chung, K. Y., & Chu, S. (1999). Measurement of gravitational acceleration by dropping atoms. *Nature*, vol. 400(6747), pages 849–852.
- [Phillips, 1998] Phillips, W. D. (1998). Nobel Lecture: Laser cooling and trapping of neutral atoms. *Reviews of Modern Physics*, vol. 70(3), pages 721–741.
- [Phillips & Metcalf, 1982] Phillips, W. D. & Metcalf, H. (1982). Laser Deceleration of an Atomic Beam. *Physical Review Letters*, vol. 48(9), pages 596–599.
- [Ping et al., 2002] Ping, J., Wang, F., & Chen, J.-Q. (2002). *Group representation theory for physicists*. World Scientific Publishing Company.
- [Raab et al., 1987] Raab, E. L., Prentiss, M., Cable, A., Chu, S., & Pritchard, D. E. (1987). Trapping of Neutral Sodium Atoms with Radiation Pressure. *Physical Review Letters*, vol. 59(23), pages 2631–2634.
- [Ribeiro et al., 2013] Ribeiro, P., Haque, M., & Lazarides, A. (2013). Strongly interacting bosons in multichromatic potentials supporting mobility edges: Localization, quasi-condensation, and expansion dynamics. *Physical Review A*, vol. 87(4), page 043635.

- [Rizzi et al., 2018] Rizzi, M., Miniatura, C., Minguzzi, A., & Vignolo, P. (2018). Scaling behavior of Tan's contact for trapped Lieb-Liniger bosons: From two to many. *Physical Review A*, vol. 98(4), page 043607.
- [Sant'Ana et al., 2019] Sant'Ana, F. T., Hébert, F., Rousseau, V. G., Albert, M., & Vignolo, P. (2019). Scaling properties of Tan's contact: Embedding pairs and correlation effect in the Tonks-Girardeau limit. *Phys. Rev. A*, vol. 100(6), page 063608.
- [Satija & Zhao, 2013] Satija, I. I. & Zhao, E. (2013). *Topological Insulators with Ultracold Atoms*. Berlin, Heidelberg: Springer Berlin Heidelberg.
- [Seaward, 2020] Seaward, J. (2020). *Gaz unidimensionnels avec interactions accordables*. Theses, Université Paris-Nord - Paris XIII.
- [Shannon, 1948] Shannon, C. E. (1948). A mathematical theory of communication. *The Bell System Technical Journal*, vol. 27(3), pages 379–423.
- [Sokolov & Shirokovskii, 1961] Sokolov, A. V. & Shirokovskii, V. P. (1961). Group theoretical methods in the quantum physics of solids (spatial symmetry). *Soviet Physics Uspekhi*, vol. 3(4), page 551.
- [Stray et al., 2022] Stray, B., Lamb, A., Kaushik, A., Vovrosh, J., Rodgers, A., Winch, J., Hayati, F., Boddice, D., Stabrawa, A., Niggebaum, A., Langlois, M., Lien, Y.-H., Lellouch, S., Roshanmanesh, S., Ridley, K., de Villiers, G., Brown, G., Cross, T., Tuckwell, G., Faramarzi, A., Metje, N., Bongs, K., & Holynski, M. (2022). Quantum sensing for gravity cartography. *Nature*, vol. 602(7898), pages 590–594.
- [Sutherland, 1968] Sutherland, B. (1968). Further Results for the Many-Body Problem in One Dimension. *Physical Review Letters*, vol. 20(3), pages 98–100.
- [Takahashi, 1999] Takahashi, M. (1999). *Thermodynamics of one-dimensional solvable models*. Cambridge University Press.
- [Tan, 2008a] Tan, S. (2008a). Energetics of a strongly correlated Fermi gas. *Annals of Physics*, vol. 323(12), pages 2952–2970.
- [Tan, 2008b] Tan, S. (2008b). Generalized virial theorem and pressure relation for a strongly correlated Fermi gas. *Annals of Physics*, vol. 323(12), pages 2987–2990.
- [Tan, 2008c] Tan, S. (2008c). Large momentum part of a strongly correlated Fermi gas. *Annals of Physics*, vol. 323(12), pages 2971–2986.
- [Vaidya & Tracy, 1979] Vaidya, H. G. & Tracy, C. A. (1979). One-Particle Reduced Density Matrix of Impenetrable Bosons in One Dimension at Zero Temperature. *Phys. Rev. Lett.*, vol. 43(20), pages 1540–1540.
- [Vignolo & Minguzzi, 2013] Vignolo, P. & Minguzzi, A. (2013). Universal Contact for a Tonks-Girardeau Gas at Finite Temperature. *Phys. Rev. Lett.*, vol. 110(2), page 020403.

- [Voit, 1995] Voit, J. (1995). One-dimensional Fermi liquids. *Reports on Progress in Physics*, vol. 58(9), page 977.
- [Volosniev et al., 2014] Volosniev, A. G., Fedorov, D. V., Jensen, A. S., Valiente, M., & Zinner, N. T. (2014). Strongly interacting confined quantum systems in one dimension. *Nature Communications*, vol. 5(1), page 5300.
- [Volosniev et al., 2015] Volosniev, A. G., Petrosyan, D., Valiente, M., Fedorov, D. V., Jensen, A. S., & Zinner, N. T. (2015). Engineering the dynamics of effective spin-chain models for strongly interacting atomic gases. *Physical Review A*, vol. 91(2), page 023620.
- [Widom, 1973] Widom, H. (1973). Toeplitz Determinants with Singular Generating Functions. *American Journal of Mathematics*, vol. 95(2), pages 333–383.
- [Wiener, 1933] Wiener, N. (1933). The fourier integral: and certain of its applications. *Nature*, vol. 132(3341), pages 731–732.
- [Wiener, 1938] Wiener, N. (1938). The Homogeneous Chaos. *American Journal of Mathematics*, vol. 60(4), pages 897–936.
- [Wigner, 1951] Wigner, E. P. (1951). On the statistical distribution of the widths and spacings of nuclear resonance levels. *Mathematical Proceedings of the Cambridge Philosophical Society*, vol. 47(4), pages 790–798.
- [Wildermuth et al., 2005] Wildermuth, S., Hofferberth, S., Lesanovsky, I., Haller, E., Andersson, L. M., Groth, S., Bar-Joseph, I., Krüger, P., & Schmiedmayer, J. (2005). Microscopic magnetic-field imaging. *Nature*, vol. 435(7041), pages 440.
- [Wineland & Demhelt, 1975] Wineland, D. J. & Demhelt, H. G. (1975). Proposed 10-14 $\Delta\nu < \nu$ laser fluorescence spectroscopy on Tl⁺ mono-ion oscillator III. *Am. Phys. Soc.*, vol. 20.
- [Wishart, 1928] Wishart, J. (1928). The Generalised Product Moment Distribution in Samples from a Normal Multivariate Population. *Biometrika*, vol. 20A(1/2), pages 32–52.
- [Yamanouchi, 1937] Yamanouchi, T. (1937). On the Construction of Unitary Irreducible Representations of the Symmetric Group. *Proceedings of the Physico-Mathematical Society of Japan. 3rd Series*, vol. 19, pages 436–450.
- [Yang, 1967] Yang, C. N. (1967). Some Exact Results for the Many-Body Problem in one Dimension with Repulsive Delta-Function Interaction. *Phys. Rev. Lett.*, vol. 19(23), pages 1312–1315.
- [Yu & Fowler, 1992] Yu, N. & Fowler, M. (1992). Persistent current of a Hubbard ring threaded with a magnetic flux. *Phys. Rev. B*, vol. 45(20), pages 11795–11804.
- [Zhang & Wang, 2006] Zhang, G.-M. & Wang, X. (2006). Spin swapping operator as an entanglement witness for quantum Heisenberg spin-s systems. *Journal of Physics A: Mathematical and General*, vol. 39(26), page 8515.